Novel Turbine Fence Optimisation Using Lateral Flow Constraint

Steven Ettema
Magdalen College
University of Oxford

A thesis submitted for the degree of
Doctor of Philosophy
Hilary 2022

Acknowledgements

I would like to thank my supervisors, Prof. Richard Willden and Dr. Chris Vogel for their guidance and support over the last 3 years. Their enthusiasm for marine renewable energy has been infectious, pushing me to ask more questions and pursue a deeper understanding of the underlying physical processes at play. I feel very privileged to have received my supervision from these talented academics.

Next I would like to thank the post docs, Dr. James McNaughton, Dr. Xiaosheng Chen and Dr. Sam Harvey, I owe them a lot for all of the time and assistance they have given me. Special thanks to Dr. James McNaughton who provided assistance with the end-wall experiments and insights to the intricacies of the Engineering Department's procurement system. Thanks also to Dr. Xiaosheng Chen for his help with turbine design and in refining the RANS-BE subroutine.

I would also like to thank all my friends, both those who I have left behind in Australia while on this amazing academic adventure and those who I have made over here. A special mention to Magdalen College Boat Club for being a great distraction and great fun.

I would like to acknowledge the General Sir John Monash Foundation without their assistance I would not have had the pleasure of extending myself in the investigation of tidal turbines and renewable energy.

Finally, I would like to thank family; especially my parents, Roxanne and Ben. Oxford is a long way from home and I am very thankful for all their support; be it in the form of care packages filled with Australian treats or your time early in the morning when I call. It has helped a lot and I feel very lucky to have such a great family.

Abstract

Tidal stream turbines lend themselves to being placed closely together as shared infrastructure costs can be distributed amongst the devices. This has led to the development of various systems with turbines arranged in a fence formation (for example, Schottel-SME's Plat-i and Orbital Marine Power's O2).

Close spacing between turbines can be used to realise a performance improvement through increased local blockage at reduced spacing (Nishino and Willden, 2012). However, flow diversion around the fence reduces the realistically achievable power compared to theoretical limits and affects, in particular, the outboard turbines within a fence. This fence-end effect results in a variation in power production and loading over the fence. The work presented in this thesis examines ways to reduce these losses and achieve more uniform power output and time-varying loading for all turbines along the fence. Two approaches are investigated in this work; a physical barrier in the form of a contoured turbine fence end-wall, and a yaw control strategy. In order to computationally examine the fluid mechanics of a turbine fence with yaw applied to end-turbines, a new rotor geometry and mesh structure is presented in this thesis. This turbine was designed at a scale to ensure fully turbulent flow over the entire blade permitting the $k-\omega$ SST RANS turbulence model to be used which facilitated computationally efficient multi-rotor blade resolved simulations.

The first approach presented in this thesis to reduce end effects used a contoured turbine fence end-wall to realign the flow normal to the turbine plane. A Reynolds-Averaged Navier-Stokes (RANS) model with an embedded blade element (BE) solver was used to investigate the variation of end losses with inter-turbine spacing. Numerical simulations demonstrated that use of an end-wall (at tip-to-wall spacing half the turbine tip-to-tip spacing of s=$0.25D$) could increase overall fence performance by up to 3.95% relative to the without-end-wall case. This performance improvement coincided with a marginal reduction in mean thrust on the

turbines, optimal tip-speed-ratio (λ^*), and basin efficiency (noting that the slight decrease in turbine thrust was more than offset by the additional thrust from the end-wall). The numerical results were compared to experiments performed in the towing tank at the SSPA facility in Sweden. This comparison showed that the RANS-BE model slightly over-estimated performance improvement due to the end-wall and highlighted some of the shortcomings of the numerical model.

The second approach used yaw control to improve the alignment of the outboard turbine to the skewed approach flow towards the ends of the fence. Blade resolved sliding-mesh simulations of a four-turbine long fence with counter-rotation about the fence centre-line, were used to adjust the yaw of the outboard turbine to align normal with the immediate inflow. The principal benefit of this was a significant reduction in unsteady, azimuthally varying blade root bending moment loads. A modest improvement in outboard turbine performance was also observed, however this was accompanied by a reduction in the performance of the inboard turbines (due to reduced lateral flow confinement) and thus had a minimal effect on total fence power.

The impact of differential turbine speed control was also investigated within the four-turbine fence with the outboard turbine aligned and yawed. Little improvement in overall fence power was found when optimising for this parameter with differential controls; however, when using the controls to balance thrust over each turbine, a reduction in thrust of 1.5% was observed while maintaining the same power output from the synchronised operation case. When a 5° yaw of the outboard turbines towards the centre-line of the fence was introduced to this control strategy a similar operational condition was found with the added benefit of reducing the amplitude of the outboard turbine blade root bending moment by 49%, bringing this loading cycle closer to that experienced by the inboard turbine.

The use of these methods to compensate for end-losses have been shown to be effective in balancing the steady load and reducing the unsteady blade loading, with a comparatively small impact on power. Given the reduction in loading and balancing of fatigue along the fence this yaw control strategy may have the potential to contribute to reductions in the cost of energy from tidal stream systems.

Contents

Nomenclature

Abbreviations

2D	Two dimensional
3D	Three dimensional
BE	Blade element
BEM	Blade element momentum
CNC	Computer numerical controlled
DNS	Direct numerical simulation
FFT	Fast Fourier Transform
GR	Growth rate
LMADT	Linear momentum actuator disc theory
MRF	Multiple reference frames
RANS	Reynolds-Averaged Navier-Stokes
SST	Shear stress transport
UDF	User defined function

Physical properties

γ	Fraction of time where flow is fully turbulent
ϵ	Dissipation rate of turbulent kinetic energy

μ	Dynamic viscosity
ν	Kinematic viscosity defined as $\frac{\mu}{\rho}$
ν_t	Eddy viscosity
ρ	Fluid density
σ_{xx}	Normal stresses
τ_{xy}	Shear stresses
τ_w	Wall shear stress
ω	Specific dissipation rate of turbulent kinetic energy
Ω	Rotational speed in rad/s
A	Area
F	Force
k	Turbulent kinetic energy
m	Mass
p	Pressure
p_v	Vapour pressure
p_z	Pressure at depth z
p_{atm}	Atmospheric pressure
$p_{section}$	Static pressure over an aerofoil section
Q_t	Torque
Re	Reynolds number defined as $\frac{\rho u L}{\mu}$
T_s	Cauchy stress tensor

TI Turbulence intensity

u' Fluctuating velocity component

u Velocity vector

u_θ Swirl velocity

u_r Radial velocity

u_x Stream-wise velocity

u_y Cross-stream velocity

u_z Vertical velocity

u_* Friction velocity defined as $\sqrt{\frac{\tau_w}{\rho}}$

u_∞ Free-stream velocity

u_{norm} Velocity normal to the turbine

V Volume

W Relative speed of the flow to turbine blade

y Wall distance

y^+ Non-dimensional wall distance defined as $\frac{u_* y}{\nu}$

Turbine and blade properties

α Angle of attack

α^* Angle of attack where section lift to drag ratio is a maximum

β Blade twist angle

δ Trailing edge thickness

η Basin efficiency defined as the ratio between power extracted from the flow to total power removed from the flow

λ Tip speed ratio defined as $\frac{\Omega R}{u_\infty}$

λ^* Tip speed ratio which achieves the highest power coefficient

λ_{max} Maximum tip speed ratio prior to the onset of cavitation

Φ Symmetry factor used to quantify bias between inboard and outboard turbines

ϕ Flow angle between the approach flow and rotor plane (sum of α and β)

Ψ Turbine yaw angle

σ Blade solidity defined as $\frac{N_b c}{2\pi r}$

θ Turbine rotational position

A_c Cross-sectional area of channel

A_l Turbine local passage cross-sectional area, bounded by a line defined at the midpoint between adjacent turbines

A_t Swept area of turbine

B_g Global blockage defined as $\frac{\sum A_t}{A_c}$

B_l Local blockage defined as $\frac{A_t}{A_l}$

C Ratio between the moments measured from the thrust and torque transducer to the blade mounted strain gauges

c Chord length

C_a Cavitation number defined as $\frac{p - p_v}{\frac{1}{2}\rho W^2}$

c_d 2D drag coefficient defined as $\frac{F_d}{\frac{1}{2}\rho W^2 c}$

c_l 2D lift coefficient defined as $\dfrac{F_l}{\frac{1}{2}\rho W^2 c}$

C_p Turbine power coefficient defined as $\dfrac{P}{\frac{1}{2}\rho A_t u_\infty^3}$

C_p^* Maximum turbine power coefficient

c_q Torque coefficient defined as $c_\theta r$

C_t Turbine thrust coefficient defined as $\dfrac{T}{\frac{1}{2}\rho A_t u_\infty^2}$

C_t^* Turbine thrust coefficient at λ^*

c_x Stream-wise local thrust coefficient defined as $c_l \cos(\phi) + c_d \sin(\phi)$

c_θ Rotational thrust coefficient defined as $c_l \sin(\phi) - c_d \cos(\phi)$

$C_{pressure}$ Pressure coefficient defined as $\dfrac{p - p_\infty}{\frac{1}{2}\rho W^2}$

D Turbine diameter

f_0 Once per-rotation frequency

F_θ Blade force in the torque direction

F_d Drag force

F_l Lift force

F_x Blade force in the stream-wise direction

F_{tip} Tip correction factor

K Resistance coefficient in the porous disc model

M_{EW} Edge-wise blade root bending moment

M'_{EW} Edge-wise blade root bending moment corrected for blade self weight

M^*_{EW} Averaged edge-wise blade root bending moment from thrust and torque transducer

M_{FW} Flap-wise blade root bending moment

M^*_{FW} Average flap-wise blade root bending moment from thrust and torque transducer

N_b Number of blades per turbine

P Turbine power

Q Volumetric flow rate through turbine swept area

Q_∞ Free-stream volumetric flow rate through a turbine swept area

R Turbine radius

r Turbine radial position

r_b Radial location of the blade centre of mass

r_T Radial location of the line of action for thrust on a turbine blade

s Tip-to-tip turbine spacing

SG Data read from the strain gauge

T Turbine thrust

V_b Turbine blade volume

Z_{hub} Depth of the turbine hub

Units and constants

$^\circ$ Degrees

g Acceleration due to gravity taken as 9.81 m/s

kg Kilograms

m	Meters
mm	Millimetres
N	Newtons

Chapter 1

Introduction

1.1 The tidal energy resource

Tidal energy is the energy associated with tidal motion. Typically this is extracted using mechanical devices, such as turbines or barrages, with greater energy extracted in regions with larger tidal ranges or high velocity tidal currents. For the United Kingdom there are several potential regions for tidal energy extraction with tidal ranges in some parts exceeding 14 m (Baker, 1991).

1.2 Methods of energy extraction

There are two classes of devices used to extract tidal energy, tidal range devices and tidal stream devices, the latter being split into horizontal axis turbines (HATs) and vertical axis turbines (VATs). The work in this thesis focuses on HATs; however, for completeness, both tidal range and VATs devices are briefly discussed in this section.

1.2.1 Tidal range devices

Tidal range devices extract energy by exploiting a head difference induced by a barrier (such as a dam or a barrage) which artificially shifts the tidal phase on either side (Neill et al., 2018). The barrier is operated to discharge water during either the ebbing, flooding or a combination of both phases of the tide (Burrows et al., 2009) and energy is extracted as the flow passes through turbines in the barrier. The energy produced using this method is proportional to the square of the water level difference on either side of the barrage (Baker, 1991; Neill et al., 2018). As a result, regions with large tidal ranges are well suited to this type of device, such as the Severn Estuary, which has a 14 m tidal range (Xia et al., 2010).

The Severn Estuary has been the subject of multiple studies (Sathiamoorthy and Probert, 1994; Ahmadian et al., 2010; Xia et al., 2010) investigating tidal range devices owing to the significant potential for energy production (an estimated 17 TWh per year (Xia et al., 2010)); and has been subject to several unsuccessful proposals to install tidal range devices dating back to 1920 (Waters and Aggidis, 2016). Despite the interest in the development of Severn Estuary, there are currently no tidal range devices installed due to two main challenges faced by this device type; environmental impacts and high development costs (Rourke et al., 2010b; Frid et al., 2012; Waters and Aggidis, 2016). This is a consequence of the significant change in the coastal hydrodynamics which can result from barrages.

1.2.2 Tidal stream devices

Tidal stream devices extract kinetic energy from the flow in a similar manner to wind turbines (Rourke et al., 2010b). Like wind energy the power output is

proportional to the cube of the inflow velocity focusing site selection on regions of fast currents. There are several challenges unique to tidal which are not present in wind owing to a disparity in fluid density and inflow speeds; these influence the loading and turbine geometry (King and Tryfonas, 2009). The density of water is approximately 832 times greater than air improving energy density (Rourke et al., 2010a); however, smaller turbine diameter (80 - 90 m for wind compared to 8 - 20 m for tidal) (Rourke et al., 2010b; Veers et al., 2003) and lower inflow speeds (7.5 - 10 m/s for wind and 2 - 3.5 m/s for tidal) (Lu and McElroy, 2017) means that the thrust of tidal and wind rotors are similar in magnitude. There are, however, some larger modern wind turbines that experience significantly higher thrusts (NES Fircroft, 2021). Tidal stream devices are also capable of significantly impacting the flow speed, and therefore performance, through effects associated with flow resistance and confinement; this is discussed in Chapter 2.

There are two classes of tidal stream devices, HATs; where the rotor spins about the axis parallel to the flow direction, and VATs; where the rotor spins about an axis perpendicular to the flow direction (Rourke et al., 2010b; Khan et al., 2009). While some VAT concepts have been developed and prototyped (Atlantis Strom, 2004; Blue Energy, 2010; ORPC, 2019), the dominant form of tidal stream devices appears to be HATs (Siemens, 2015; Andritz Hydro, 2016; SIMEC Atlantis Energy, 2019; Orbital Marine Power, 2019). This can, in part, credited to the extensive knowledge base of HATs from conventional wind turbines.

1.3 Support structure

There is a significant variation in the support structures designed for tidal stream energy devices due to the complexities of installation, maintenance, geographic and hydrodynamic conditions (King and Tryfonas, 2009). Broadly speaking there are two classes of support systems for tidal turbines; floating and fixed. Fixed systems are rigidly attached to the bed through support structures; such as monopiles, which are commonly used in the wind industry (Arshad and O'Kelly, 2013). This type of support structure has been used in the design and installation of the SeaGen tidal rotor (Siemens, 2015). Despite its success and well established position in offshore wind there are limits to the depths that this support system can be used owing to increased cost with depth of installation. This is due to the bed conditions, which are more commonly scoured rock at tidal stream locations, and limited duration for access due to strong currents making it difficult for installation.

In contrast floating tidal devices may be more suitable for deep water applications where attaching a structure rigidly to the bed is cost prohibitive. This support structure type has been implemented by Orbital Marine in their O2 and SR2000 turbines (Orbital Marine Power, 2019) as well as by Sustainable Marine Energy in the PLAT-I and PLAT-O array types (SME, 2019). Floating tidal devices also provide the additional benefit of operating in the upper region of the water column where the currents are typically higher; this positioning also allows easier access for maintenance. Operating the turbine near the surface of the water column does risk cavitation due to the lower pressure and care must be taken when defining the operation conditions to limit this risk by restricting the operating point to a certain range (Wimshurst et al., 2018). Furthermore, floating structures and

the turbines they support also experience higher wave loading, with the action of the waves causing fluctuations in velocity through the turbine. Additional challenges for floating tidal devices include platform loading and the connection to the electricity grid as the floating mooring lines require flexible electric connections (Brown et al., 2001).

1.4 Tidal turbine fences

One appealing feature of HATs over tidal range devices is the device modularity allowing additional power generation by placing more turbines in the flow. The flexibility of device placement calls to question how best to arrange tidal turbines. Work by Draper and Nishino (2014) suggested turbines placed in a fence formation (a single row of turbines) produced greater power than a staggered array of turbines (two rows of turbines staggered such that down-stream turbines are not in the shadow of up-stream turbines). Work performed numerically (Schluntz and Willden, 2015; Vogel and Willden, 2017) and experimentally (Cooke, 2016; McNaughton et al., 2019) has confirmed that turbines in fence formation achieve enhanced power due to the channel blockage effect (discussed in Section 2.2). However, as Cooke (2016) showed, this performance improvement is not evenly distributed along the fence due to the diversion of inflow around the ends of the turbine fence (end losses).

Tidal fence devices are growing in popularity with manufactures producing several prototypes including the SR2000 (Orbital Marine Power, 2019) and PLAT-I (SME, 2019). These devices indicate a push toward using shared infrastructure between turbines with the turbine mounted to floating support structure. This

allows the turbines to achieve a performance improvement from the close proximity in the fence formation and reduces the cost as infrastructure is shared.

1.5 Thesis outline

This research aims to further the understanding of turbine fence end losses through CFD simulation and physical testing. In particular, this work focuses on:

1. Establishing performance variation along short turbine fences
2. Determining the azimuthal variation in blade loads between the inboard and outboard turbines
3. Evaluating potential methods to mitigate loading and power imbalances along short turbine fences though:
   (a) The addition of an end-wall
   (b) Yaw adjustment of outboard turbines

An overview of turbine performance and relevant literature is presented in Chapter 2, and methods for numerical modelling of turbines are presented in Chapter 3. The design of a turbine fence end-wall (Chapter 4) and testing (Chapter 5) is examined. Chapter 6 presents a design of a turbine of sufficient geometric scale to ensure fully turbulent flow over the entire blade tidal turbine which facilitates the detailed modelling of a yaw control strategy in Chapter 7. Finally, a summary of the finding from this thesis is made in the conclusions chapter (Chapter 8).

Chapter 2

Rotor fence performance

This chapter explores the hydrodynamic performance of horizontal axis tidal turbines in a fence arrangement. Firstly, the performance metrics of a single turbine and the concept of channel blockage is introduced. These ideas are then extended to a turbine fence, presenting turbine fence performance metrics and introducing local blockage. Finally, fence performance losses are discussed and potential mitigation methods are presented.

2.1 Performance metrics

2.1.1 Single turbine

The performance of a single horizontal axis turbine is typically characterised by its thrust and power coefficient, defined as

$$C_t = \frac{T}{\frac{1}{2}\rho A_t u_\infty^2}, \quad C_p = \frac{P}{\frac{1}{2}\rho A_t u_\infty^3} \tag{2.1}$$

where C_t is the thrust coefficient, C_p is the power coefficient, T is the thrust on the turbine, P is the power produced by the turbine, ρ is the density of the fluid, A_t is the swept area of the turbine and u_∞ is the free-stream flow velocity normal to the turbine. Turbine performance varies with the tip-speed-ratio (λ), which is defined as

$$\lambda = \frac{\Omega R}{u_\infty} \tag{2.2}$$

where Ω is the rotational speed of the turbine in radians per second and R is the turbine radius. Typically, C_t monotonically increases with λ and C_p initially increases with λ to a maximum value (C_p^*) at λ^* after which performance reduces. A maximum C_p exists due to a reduction in blade torque (Q_t) at high speed through increasing drag losses. Power from a turbine is extracted following

$$P = Q_t \Omega. \tag{2.3}$$

This implies that power increases as the turbine rotates faster; however, Q_t is a function of Ω that decreases at high Ω due to a sub-optimal angle of attack (α) on the blade. Figure 2.1 plots the velocity triangle at a radial station (r) on a turbine blade and demonstrates how the angle of attack decreases with Ω.

Figure 2.1 shows that the flow velocity over a turbine blade (W) is a function of the velocity in the stream-wise direction (u_x) and the velocity in the rotational direction; composed of the flow in the rotational plane (u_θ) and the angular velocity of the section (Ωr).

$$W = \left[(\Omega r + u_\theta)^2 + u_x^2 \right]^{1/2} \tag{2.4}$$

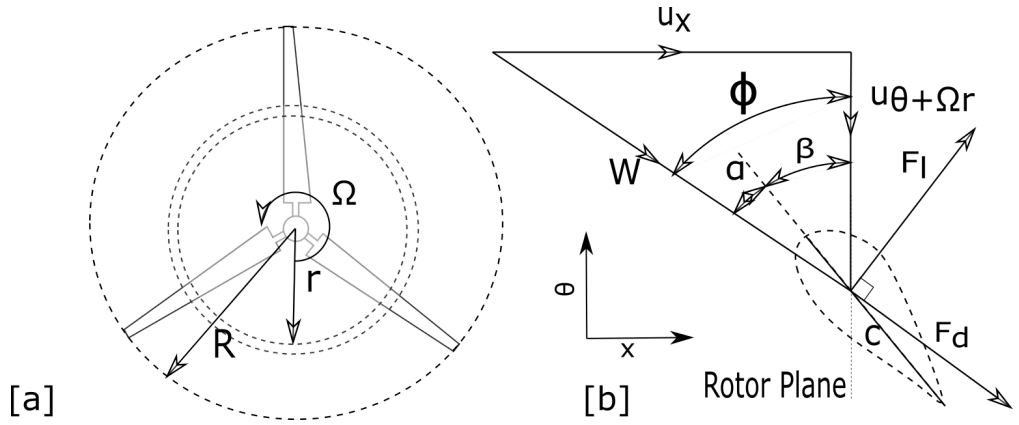

Figure 2.1: (a): Rotor discretisation; (b): resolution of lift and drag forces at radius r.

The flow approaches the turbine blade at an angle ϕ, which is the sum of α and the blade twist (β). As a result, a unit span of the section produces a lift force (F_l) and a drag force (F_d) defined as

$$F_l = \frac{1}{2}\rho W^2 c_l c, \quad F_d = \frac{1}{2}\rho W^2 c_d c \tag{2.5}$$

where c is the chord length, c_l is a lift coefficient, and c_d is a drag coefficient. c_l and c_d are often taken from two-dimensional (2D) aerofoil sections; this simplification requires no flow along the turbine radius and is explored in Section 3.1.2. Force in the stream-wise (F_x) and rotational (F_θ) directions at r can be determined by applying a rotation to F_l and F_d. This yields

$$F_x = F_l \cos\phi + F_d \sin\phi$$

$$F_\theta = F_l \sin\phi - F_d \cos\phi.$$

The forces can be integrated over the length of the blade (from the radius of the nacelle, r_{hub}, to the end of the blade R) to determine T and Q_t,

$$T = \int_{r_{hub}}^{R} F_x(r)dr$$
$$Q_t = \int_{r_{hub}}^{R} F_\theta(r)rdr$$

While the relations are simple to express, T and Q_t are complex functions dependant on the inflow properties, the turbine design, and the turbine operation. Consequently, various models exist to predict turbine performance and the impact on the surrounding flow, a selection of models are discussed in Chapter 3

2.1.2 Turbine fence

A turbine fence is an array of turbines which operates in the same plane. This arrangement has been shown to generate greater power than staggered alignments (Draper and Nishino, 2014) and the close proximity of turbines in this configuration allows for the use of shared infrastructure within the fence; such as in the Orbital Marine O2 and SR2000 turbine (Orbital Marine Power, 2019) and the Sustainable Marine Energy PLAT-I device (SME, 2019).

Alongside the performance metrics presented for individual turbines in Section 2.1.1 the basin efficiency (η) is an important characteristic of a turbine fence. Basin efficiency is defined as the ratio between useful power extracted from the flow and total power removed from the flow,

$$\eta = \frac{\sum P}{\sum P_{removed}} \tag{2.6}$$

where $\sum P$ is the sum of power produced by all the turbines and $\sum P_{removed}$ is sum of all power removed from the flow, including from parasitic drag and dissipated in

wake mixing downstream of the turbines. Parasitic drag includes forces which do not contribute to the power production, such as the force applied from the support structure to the flow. The definition of Belloni (2013) was used to determine η throughout this thesis following,

$$\eta = \frac{\sum P}{(\sum T + \sum T_{structure})_x u_\infty}. \tag{2.7}$$

where $\sum T_x$ is the sum of the turbine thrusts in the stream-wise direction and $\sum T_{structure-x}$ is the sum of the thrust from the support structure in the stream-wise direction. This value only considers the floating structures in this thesis and does not include additional sources of parasitic drag such as from the support towers and other structural support.

2.2 Blockage

Pertinent to improving the performance of a turbine is an understanding of the blockage effect. Garrett and Cummins (2007) first investigated blockage in a channel demonstrating that an improvement in tidal turbine performance was possible due the volume-flux constraint presented by the channel to the flow through the turbine. A key finding from this study was that the maximum C_p surpassed the well-established Lanchester-Betz limit[1] for unblocked flows of 16/27 in blocked channels. It was shown that a new limit of $(16/27)(1 - B_g)^{-2}$ applies to turbines in blocked flow conditions, where B_g is the blockage ratio defined as $\frac{\sum A_t}{A_c}$ (A_c is the channel cross-sectional area). This effect has been observed experimentally in the work of Bahaj et al. (2007) who saw a performance improvement when testing

[1] Also referred to as the Betz limit.

a turbine in a cavitation tunnel and more recently by Ross and Polagye (2020) in their testing of a HAT and VAT in varied blockage conditions.

The result from Garrett and Cummins' studies have been expanded on by various authors, leading to additional definitions of blockage for different area ratios, namely global blockage (B_g), array blockage (ratio of frontal area of turbine array, A_a, to channel cross section area, $B_a = \frac{A_a}{A_c}$) and local blockage (ratio of device area, A_t, to the local passage cross-sectional area, A_l, $B_l = \frac{A_t}{A_l}$). These three definitions are illustrated in Figure 2.2. Using these definitions for blockage, Nishino and Willden (2012) introduced an approach to analyse an ideal system at both the turbine and the array scale using continuity and momentum relations to maintain compatibility between the two models. Through this theoretical frame work they identified a new limit for power extraction from a long fence of turbines partially blocking an infinitely wide channel ($B_g = 0$) of $C_p = 0.798$ when $B_l \approx 0.4$, a 34.5% improvement on the Betz limit of 0.593. A small further uplift in performance, dependent on the Froude number, can be achieved when the effects of free-surface deformation are also considered (Vogel et al., 2016).

A limitation to the models discussed above is the reliance on linear actuator disc theory which is an idealised parameterisation of turbine behaviour that does not account for real rotor properties such as the shape of the blade profile. This detail can be represented by using more refined methods discussed in Chapter 3.

Performance improvements from increased local blockage have been observed numerically by Schluntz and Willden (2015), who explored the effect of local blockage on rotor design. It was shown that higher power output is possible when turbines designed for low blockage conditions are moved closer together, however greater performance is observed when turbines are designed for the higher

blockage conditions. Experimentally, Cooke (2016) has demonstrated the effect of local blockage in a flume through the use of thrust measurements on porous disks. More recently, scale turbine testing of two 1.2 m diameter turbines at a 0.25D tip-to-tip spacing by McNaughton et al. (2019) has provided further evidence of the constructive interference effect of local blockage, observing a performance improvement above the single turbine maximum power when placing a second turbine adjacent at a close spacing.

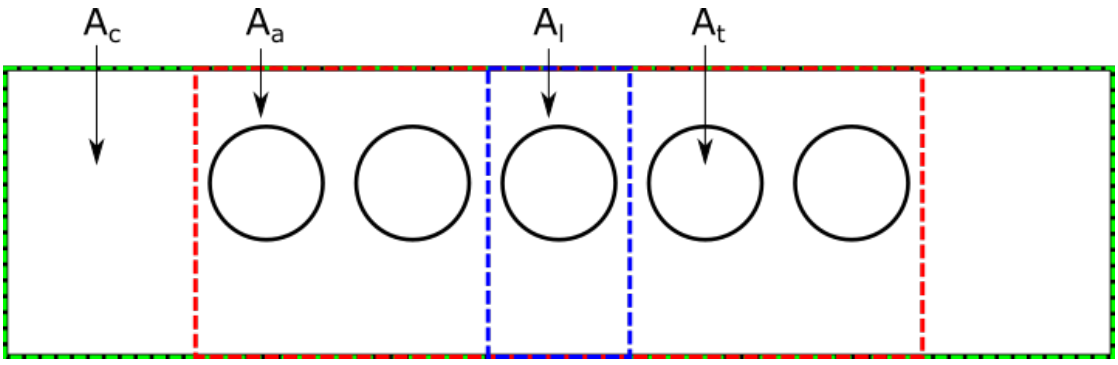

Figure 2.2: Cross section view of the representative areas for global (green), array (red) and local (blue) blockage, the circles represent individual turbines swept area.

2.3 End-losses

A further limitation of Nishino and Willden (2012) was the infinitely long turbine fence assumption where all turbines in the fence see uniform flow; in practise fences are a finite length and performance varies due to flow diversion around the ends of the fence as illustrated in Figure 2.3. The effect of fence length was investigated by Cooke (2016) who used a fence of porous discs in a flume to investigate the effects of spacing and variation in performance along the fence. Their results showed that power could be increased by adjusting the spacing as suggested by Nishino

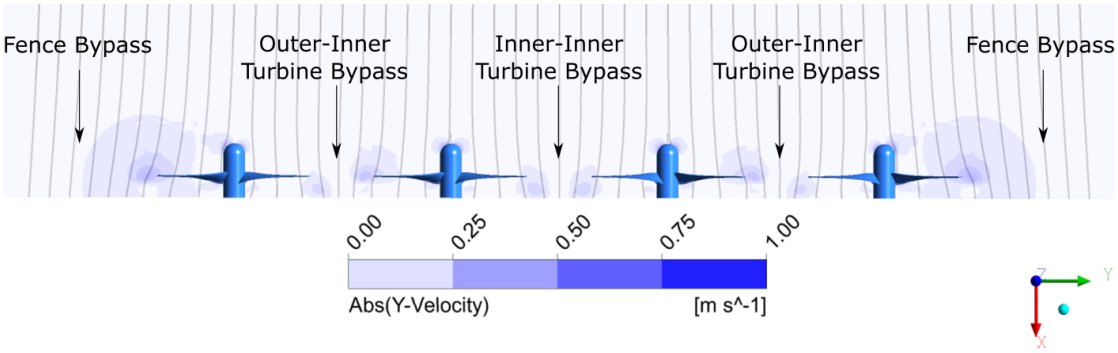

Figure 2.3: Streamlines of flow approaching a turbine fence, highlighting the greater flow diversion around the end turbines over the inner turbines. The contours are the absolute value of the cross-stream flow velocity.

and Willden (2012), however energy losses arising from viscous effects and flow diversion around the ends of the fence limited the power to less than hypothesised in the ideal case. The reduction in power due to flow diversion around turbine fences has also been observed numerically in a RANS-BE model by Vogel and Willden (2017). Vogel and Willden (2017) observed a drop in performance along a fence of four turbines ($B_l = 0.196$, $C_p = 0.535$ for the inboard turbines and $C_p = 0.528$ for the outboard turbines), crediting this reduction in performance to flow diverting around the fence, reducing the flow speed through the turbines.

The performance loss at the end of a turbine fence is often referred to as the fence end-loss. This loss is a result of insufficient confinement at the end of the fence allowing flow to bypass the turbines, leading to a performance reduction for the end turbines. While an attempt to include this effect in analytical models has been made by Cooke (2016), this model does not accurately capture the thrust distribution across the fence. Instead estimates for short array performance require the use of numerical models to resolve the performance variation along the array (Schluntz, 2014; Vogel and Willden, 2017).

2.4 Methods to improve turbine performance

Turbine performance can be augmented by either a physical manipulation to the turbine design (physical optimisation) or through a modification to how turbines are operated and oriented (operational optimisation). Within these two classes various methods have been investigated to improve total energy output. This section presents a selection of these methods which are further developed throughout this thesis.

2.4.1 Physical optimisation

The physical optimisation of turbines requires adjusting the design of the rotor (blade profile, twist and solidity) as well as the infrastructure surrounding the rotor (nacelle design and ducting).

2.4.1.1 Turbine design

The design of a turbine is a loosely constrained problem with many potential blade cross-sections and geometries, making it difficult to define an optimal design. Consequentially, simplifying assumptions are required to constrain the problem and optimise. Typically, this includes constraining the design to a single aerofoil or family of aerofoils such as the MHKF1 (Shiu et al., 2012) which has been specifically designed to suit the needs of tidal turbines (high lift-to-drag ratio, low susceptibility to cavitation and structurally efficient) or the NACA-63-XXX family which have previously been used in turbine design (Bahaj et al., 2007; Laurens et al., 2016; Park et al., 2016). It is also common to transition between profiles (Bahaj et al., 2007; Shiu et al., 2012) as the optimal profile is a function

of the radial position on the blade.

Various methods have been suggested for defining the blade twist and solidity distribution along the span of a turbine blade (Masters et al., 2011; McIntosh et al., 2011; Malki et al., 2013). While methods vary slightly, they all rely on the blade element method and its underlying assumptions (outlined in Section 3.1.2) to determine the optimal turbine blade twist and solidity. This method targets an optimal angle of attack, α, (angle where the ratio of lift to drag is a maximum) and a target local thrust coefficient, c_x, along the blade length. These variables are not independent of each other due to feedback between α, which maximises torque ($rF_l \sin\phi - rF_d \cos\phi$), and c_x. A change in c_x directly affects the F_l and F_d over the turbine blades as well as the flow through the rotor. Given this, the target c_x is usually determined from iteration until an optimal C_p is achieved. c_x may also vary over the blade length as regions along the turbine may require different c_x to optimise power production or the target c_x may cause intersecting geometries as large c_x results in a larger chord; in which case target c_x can be reduced. A blade element method is used for the initial design of a turbine in Chapter 6.

For the design of turbine fences, local blockage effects allow the fence to sustain a slightly higher thrust which alters the optimal c_x between turbines within an array. Cao et al. (2019) showed this effect over a four-turbine fence in highly blocked conditions ($B_g = 14.1\%$) with the maximum fence power being achieved when the inboard and outboard turbines were designed with a uniform c_x of 3.4 and 3.6. In contrast the optimal c_x for a single turbine in an identical blockage conditions was 3.0.

2.4.1.2 Ducting of turbines

Some designs (European Marine Energy Centre, 2018) of tidal turbines have included ducting around rotors to improve power output by convective acceleration of flow through the throat of the duct. This has previously been considered in the wind industry (Igra, 1981; Khamlaj and Rumpfkeil, 2018) in order to improve the mass flow rate through turbines to achieve greater power output per swept area of rotor and has lead to the development of various prototype designs (Wind-works, 2019; Halo Energy, 2019). Work by Khamlaj and Rumpfkeil (2018) has demonstrated, using a Reynolds-Averaged Navier-Stokes (RANS) model with an embedded blade element (BE) actuator disk model, that the introduction of ducting on wind turbines can marginally improve the total power output ($\sim 2\%$).

Despite an increase in total power output, radially ducted wind and tidal turbines tend to have a reduced C_p when the performance is normalised for the area at the opening of the duct. This has been investigated for tidal applications by Belloni (2013) who, like Khamlaj and Rumpfkeil (2018), used RANS-BE simulations to investigate the performance of ducted turbines. Belloni (2013) observed an overall reduction in η with the introduction of ducting due to the higher thrust it imposed onto the flow. This study was limited as it only analysed one type of radially symmetric ducting around a turbine drawn from observations of a proposed commercial devices. Work in this area by Fleming and Willden (2016) produced similar results to Belloni (2013) when investigating a variety of duct shapes. Using an actuator disc model and taking advantage of radial symmetry, 2D simulations were carried out on a total of 8 duct profile shapes of equal length to the turbine diameter, D. Like Belloni (2013), the results indicated that the C_p, normalised

using frontal area of the duct, was reduced for all turbines when compared to the unducted case. Despite the decreased performance Fleming and Willden (2016) observed an overall increase in power output due to the higher flow through the ducted turbine. Additionally, the shape of the ducting was important to improve η, as the thrust applied to the flow varied with ducting profile. Fleming found that a thick cambered profile was a superior design as the camber in the profile allowed for the convective acceleration of flow to the rotor plane and the thick side wall reduced overall viscous losses. Large viscous losses were observed in the case of thin cambered profiles due to large re-circulation zones forming on the outer surface of the duct as the flow separated.

Ducting of tidal turbines has also been shown to improve the power output in yawed flow conditions up to angles of 20° due to better alignment of the flow with the rotor plane inside the duct (Belloni et al., 2013). While turbine performance is improved, η is reduced as the thrust applied to the duct increases due to asymmetric flow separation from the ducting. Although the total load is higher on the structure and turbine, Belloni et al. (2013) were able to demonstrate that a duct removed almost all of the azimuthal variation in loading on the rotor when compared to the bare turbine.

Ducting of turbines is further explored in this thesis in Chapter 4 at the turbine fence scale.

2.4.2 Operational optimisation

Adjustment to turbine orientation and operation has been shown to improve performance. Operational improvements are advantageous for energy providers as

they provide additional power output at little to no additional investment in infrastructure.

2.4.2.1 Differential speed controls

A common way to adjust the power output from a rotor is to modify the rotational speed. Rotors are designed for a specific λ where power production is optimised for target inflow conditions. Within a turbine fence, local flow interactions between turbines and bypass flows around the fence's end alter the inflow conditions from the solitary design case for each turbine. Consequentially, the rotational speed needs to be modified to locally optimise power for each turbine or to balance the force distribution along the fence. This has been studied experimentally by McNaughton et al. (2021) who demonstrated that differential speed controls are an effective control strategy to balancing the thrust between inboard and outboard turbines on a turbine fence, exposing them to similar loading over their life cycles. This is explored further in Chapter 6.

2.4.2.2 Yawing of turbines

An operational control common to both wind and tidal turbines is yaw. Yaw adjustments are often required to ensure that the turbine is positioned normal to the flow, in wind this is due to the continually changing inflow direction and for tidal, the reversal of the tide. The operation of a single tidal turbine yawed relative to the inflow produces less power than when it is normal to the flow due to the reduced mass flux through the turbine. In addition there is increased unsteady loading as a result of blade advancing and retreating effects (Galloway et al., 2011). Yawing a turbine imposes a lateral force onto the flow, which could be used

to constrain the inflow and wake expansion through a turbine fence. Furthermore, outboard turbine yaw may compensate for the flow diversion around the fence end. This control strategy is investigated in Chapter 6.

Chapter 3

Simulation of tidal turbines

This chapter presents some common methodologies for simulating tidal turbines which are used in this thesis. There are two broad classes of models for simulating tidal turbines, analytical - where assumptions are made about the turbines to simplify the model, and numerical - where at least some part of the analytical problem is solved numerically. This chapter explores analytical and numerical models, discussing the incremental changes in the models as complexity is increased and accuracy is improved.

3.1 Analytical models

Analytical models are typically a low computational cost method for simulating turbines. These models tend to be steady approximations, requiring the resistance from the turbine blades to be distributed over the entire swept area. Computationally they are treated as an actuator disk with a surface of negligible thickness that imposes, at a minimum, a momentum loss term on the fluid domain. The turbine

model is usually embedded with a secondary set of equations to simulate the fluid flow. These include the momentum, continuity and energy equations (Garrett and Cummins, 2007; Nishino and Willden, 2013), the shallow water equations (Bonar et al., 2018) and Reynolds-Averaged Navier-Stokes (RANS) equations (Hunter et al., 2015).

The practical application of these models are to provide insights by simulating the leading order physics of the system. Using this model Garrett and Cummins (2007) were able to demonstrate the performance improvement when turbines are placed in a constrained channel (blockage effect).

3.1.1 Porous disk models

The porous disk model is a type of actuator disk model which does not require the specification of turbine geometry or rotational speed, instead simplifying the problem by using a single resistance coefficient (K) to determine the thrust (T) a turbine imposes on the flow following,

$$T = K\frac{\rho}{2}u_x|u_x|A_t \tag{3.1}$$

where ρ is the density, u_x is the velocity through the rotor and A_t is the swept area of the turbine. An estimate for the power production of porous disk is often made by assuming that there are no efficiency losses of the turbine allowing power (P) to be calculated directly from the turbine thrust,

$$P = Tu_x \tag{3.2}$$

When incorporated within the momentum equations, the porous disk model

gives rise to linear momentum actuator disk theory (LMADT) which has been used to evaluate the theoretical maximum efficiency of a turbine (Garrett and Cummins, 2007; Houlsby and Draper, 2008; Nishino and Willden, 2012). This model is popular as it removes turbine geometry as a variable, replacing the unconstrained geometry problem with a single parameter which can be iterated over to determine optimal turbine performance.

3.1.2 Blade element models

Blade element (BE) models are commonly used in the design and performance analysis of tidal turbine rotors (Malki et al., 2013; Olczak et al., 2016; Belloni et al., 2017; Cao et al., 2019). The BE method uses lift and drag data from 2D aerofoil sections at varied angles of attack (α) in conjunction with the blade twist angle (β) and chord length (c) to approximate the forces at different radial stations on the blade. This imposes a pressure drop (Δp) and swirl velocity (u_θ) across the actuator disc. The use of 2D data assumes no radial flow component along the span of the rotor which is typically violated by span-wise pressure gradients on rotor blades. Despite this, the flow component can be considered small relative to the primary inflow velocity over the majority of the blade with the exclusion of the hub and the tip region; correction models exist in these regions and are discussed further in this section.

The BE equations can be derived by considering the velocity triangle in Figure 3.1 at a point along the blade and equating the relevant forces. This yields the following expressions for pressure drop and swirl velocity for an element at radial location r within the swept area:

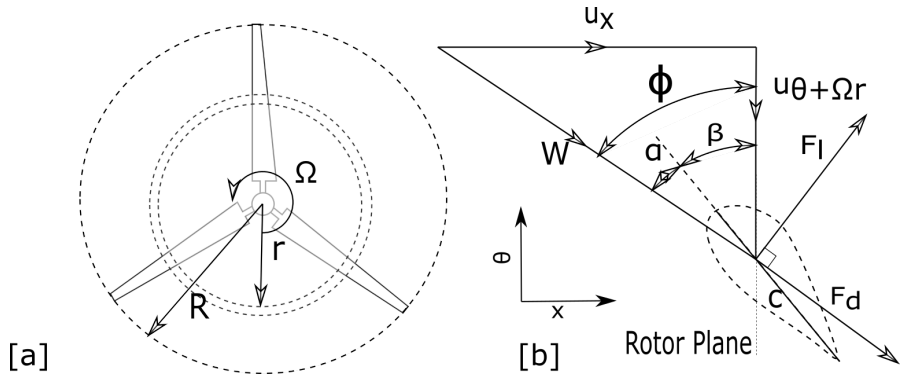

Figure 3.1: (a): Rotor discretisation; (b): resolution of lift and drag forces at radius r.

$$\Delta p = \frac{1}{2}\rho W^2 \sigma \left(c_l \cos\phi + c_d \sin\phi\right), \tag{3.3}$$

$$u_\theta = \frac{W^2 \sigma \left(c_l \sin\phi - c_d \cos\phi\right)}{4u_x}, \tag{3.4}$$

where W is the relative speed of the flow to the blade, ϕ is the flow angle between the approach flow and rotor plane (which is the sum of α and β), c_l is the 2-dimensional lift coefficient at α, c_d is the 2-dimensional drag coefficient at α, u_x is the stream-wise velocity component at the radial position r within the rotor plane and σ is the blade solidity defined as

$$\sigma = \frac{N_b c}{2\pi r} \tag{3.5}$$

where N_b is the number of blades and c is the chord length at radial position r.

W can be determined by analysing the components of the flow and the rotation of the blades to arrive at the expression,

$$W = \left[(\Omega r + u_\theta)^2 + u_x^2\right]^{1/2} \tag{3.6}$$

where Ω is the rotational speed of the turbine.

The derivation of the BE model implies that fluxes are constrained to each concentric streamtube as flow is only permitted in the stream-wise and azimuthal directions, not allowing an exchange of radial momentum. In reality a radial pressure gradient is introduced between the pressure and suction surfaces of the hydrofoil at the blade tip driving a spanwise flow (Masters et al., 2011). Various tip correction models attempt to account for the reduction in power resulting from this flow, an overview of the performance of some common implementation can be found in Koh and Ng (2016). For this study the commonly used tip correction model of Glauert (1935) was included in the BE model; this factor reduces the loading on the outboard blade span following:

$$F_{tip} = \frac{2}{\pi}\cos^{-1}\left[\exp\frac{N_b\left(1-\frac{R}{r}\right)}{2\sin\phi}\right] \tag{3.7}$$

where R is the turbine radius.

Like the porous disk model, the blade element model can be embedded within the momentum equations. This gives rise to the blade element moment (BEM) model. Various forms of this model exist (Masters et al., 2011; Galloway et al., 2014; Vogel et al., 2018) which serve as quick estimates of turbine power production and allow the effect of basic control strategies such as pitch-to-feather to be investigated. One noteworthy example is proposed by Vogel et al. (2018) who analytically accounted for the effects of blockage in BEM theory. Vogel et al. (2018)

verified the model by showing that close agreement with power output (within 3% of blade resolved simulation) can be achieved using the computationally inexpensive constrained BEM method.

The implementation of the BE model within this thesis embeds the BE equations into a RANS model (RANS-BE) using a user defined function (UDF) within ANSYS Fluent 15.0 ANSYS Inc. (2013). When called, the UDF applies a pressure drop and swirl velocity across a cell face within the turbine swept area as a boundary condition for the RANS model. This approach has previously been used by McIntosh et al. (2011) and Cao et al. (2019) to simulate a turbine within a highly blocked channel. Further refinement of this model is detailed in Chapter 6 of this thesis. Details of the RANS model can be found in Section 3.2.1.

Careful consideration of the model limitations have to be made prior to the implementation. As discussed previously in this section the set up of the model restricts radial flow and imposes a permanently present resistance at all radial locations in the rotor's swept area. The later restriction limits the use of the model to uniform inflow conditions normal to the rotor plane, however some implementations of BEM models have been shown to have favourable results in comparison to experimental data (Galloway et al., 2014) when these restrictions are relaxed. This suggests a similar implementation may be possible in a RANS-BE model. Nevertheless, the restriction to steady conditions limits the ability to simulate turbines under wave motion or rapidly varying flow conditions. Furthermore the restriction limiting the radial exchange of momentum along the blades also has implications for the flow conditions the RANS-BE model can be used in. Conditions where the flow is not orthogonal to the rotor, such as yawed inflow, induce a radial component to the flow, impacting the accuracy of the model.

3.1.3 Actuator line models

Actuator line models are an unsteady implementation of the blade element equations which permit an approximation for the temporal and spatial variation of turbine loading and performance to be modelled. The model approximates turbine blades as a number of discrete segments which experience 2-dimensional flow locally. At each timestep, the inflow velocity is determined based on the relative motion between the flow field and blade motion following

$$W = \left[(\Omega r + u_\theta)^2 + u_x^2\right]^{1/2} \tag{3.8}$$

and the angle of attack (α) is calculated following Figure 3.1. Individual element forces can then be determined through looking up c_l and c_d from a set of 2-dimensional aerofoil data, allowing a blade force and drag to be determined for a given actuator line section following

$$\begin{aligned} L_m &= \frac{1}{2}\rho W^2 c_l(\alpha) c \Delta r \\ D_m &= \frac{1}{2}\rho W^2 c_d(\alpha) c \Delta r \end{aligned} \tag{3.9}$$

where L_m and D_m is the lift and drag on element m, respectively, and Δr is the length of the actuator line segment in the radial direction.

Unlike the BE method these forces are not smeared over the rotor's swept area, instead, forces are applied over a spatially and temporally varying region. Given the model resolves the forces along a discrete line, the application of this line source in a numerical model may lead to some numerical instabilities. For this reason, a technique of smearing of the force over adjacent cells is used. This is achieved by applying a scaled force over the adjacent cells using a Gaussian kernel function, η,

defined as

$$\eta_m = \frac{1}{\epsilon^3 \pi^{3/2} \exp\left[-(\frac{\mathbf{p}}{\epsilon})^2\right]} \tag{3.10}$$

where ϵ controls the width of the Gaussian and $\mathbf{p}$ is the distance vector between the grid point and the actuator line element. The application of the Gaussian is such that the integrated force applied over the adjacent cells matches that of the forces defined from Equation 3.9. This process is repeated every timestep within the simulation.

The actuator line method has been implemented in studies of both wind (Schmitz and Jha, 2013) and tidal (Baratchi et al., 2017) turbines. With both models capable of reproducing observed physical phenomenon, such as the formation of a tip vortex. Despite the actuator line models promising performance, it has not been used in this thesis due to the additional simulation time required to achieve converged results that are periodic in time.

3.2 Numerical models and methods

As discussed in the above section analytical models are useful for resolving the leading order physics of a tidal turbine. However, additional factors such as turbulence, tip vortices and sheared inflow profiles, which are not readily resolved in these models, are often important when designing and determining the performance of turbines. In these conditions the use of a numerical model is often required. While there are many methods of numerically solving this problem (such as Large Eddy Simulations and Direct Numerical Simulation) only the Reynolds-

Averaged Navier-Stokes is discussed in this section. Two approaches for turbine simulations within this framework are discussed in this section, the Multiple Reference Frames (MRF) and the Sliding mesh approach.

3.2.1 Reynolds-Averaged Navier-Stokes equations

The Reynolds-Averaged Navier-Stokes (RANS) equations are a fundamental component of modern computational fluid dynamics (CFD). These equations are a time-averaged version of the Navier-Stokes equations which themselves are a per-volume expression of Newton's second law:

$$\frac{ma}{V} = \frac{\sum F}{V} \tag{3.11}$$

where $\sum F$ are the forces acting on a control volume of fluid, a is the acceleration of the fluid, V is the volume of the fluid element and m is the fluid mass. The fluid density, ρ can be used in place of the $\frac{m}{V}$ fraction. Considering the shear and normal stresses drawn on the infinitesimally small control volume in Figure 3.2 and making the assumption of an isotropic incompressible fluid, an expression for fluid motion can be derived:

$$\rho \frac{\mathrm{D}u}{\mathrm{D}t} = \rho \mathbf{g} - \bigtriangledown T \tag{3.12}$$

where u is the velocity, g is the acceleration due to gravity, $\frac{\mathrm{D}}{\mathrm{D}t}$ is the material derivative consisting of both temporal and convective terms, $\bigtriangledown$ is the grad operator and T is the Cauchy stress tensor. In 3D T_c is defined as

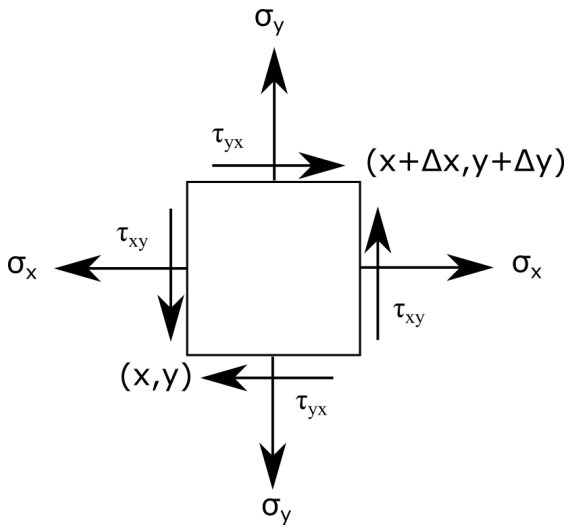

Figure 3.2: Stresses acting on an infinitesimally small control volume in 2D

$$T_c = \begin{bmatrix} \sigma_x & \tau_{xy} & \tau_{xz} \\ \tau_{yx} & \sigma_y & \tau_{yz} \\ \tau_{zx} & \tau_{zy} & \sigma_z \end{bmatrix} \tag{3.13}$$

where σ are normal forces and τ are shear forces. The expression for motion prescribed by Equation 3.12 is useful as it describes how fluid will behave when stresses act upon it. However, knowing what these stresses are requires the formation of a constitutive relation between the stress and strain rate of the fluid (transverse velocity) through the viscosity (μ). Details of how this constitutive law is applied can be found in Schlichting and Gersten (2000). This leads to the more common expression for the Naiver-Stokes equation as:

$$\rho \frac{\mathrm{D}u}{\mathrm{D}t} = \rho \mathbf{g} - \bigtriangledown p + \mu \bigtriangledown^2 u \tag{3.14}$$

where p is the fluids static pressure.

When appropriately discretised, the equation presented above is capable of describing fluid flow across all length and time scales with a simulation methodology known as direct numerical simulation (DNS). This is exceptionally computationally intensive both in terms of memory and CPU requirements. For this reason additional assumptions are made to reduce the complexity of the problem. The approach adopted for the RANS equations is to decompose the velocity into a time-averaged and a fluctuating components such that

$$\mathbf{u}(\mathbf{x},t) = \overline{\mathbf{u}}(\mathbf{x}) + \mathbf{u}'(\mathbf{x},t),\ \overline{\mathbf{u}'} = 0 \tag{3.15}$$

where $\mathbf{u}$ is the velocity vector which has a component direction ($\mathbf{x}$), primes represent fluctuating components and the overbar indicates a time average. Substituting this expression into Equation 3.12 yields

$$\rho\frac{\mathrm{D}\overline{u}}{\mathrm{D}t} = \rho\mathbf{g} - \frac{\partial p}{\partial x_i} + \frac{\partial}{\partial x_j}(\mu\frac{\partial\overline{u_i}}{\partial x_j} - \rho\overline{u_i'u_j'}) \tag{3.16}$$

the $\rho\overline{u_i'u_j'}$ is commonly referred to as the Reynolds stress tensor. Similar to T_c this expression describes how fluid moves when stresses are applied, in this case the stresses arrive from fluctuations in the flow. However, unlike T_c there is not a constitutive law which can be applied. This is to say the velocity fluctuations are not directly related to the time average velocity. This leads to a closure problem and the need for additional models to account for the effect of turbulence.

3.2.1.1 Turbulence modelling

Various models exist for approximating turbulence in flows dependant on the application. One of the most common turbulence models simulates the transport

and dissipation of energy using an eddy viscosity. This is achieved by applying the Boussinesq hypothesis to relate the turbulent stresses to the mean velocity gradients similar to how the viscous stresses are related to the complete velocity gradient by

$$-\overline{u_i' u_j'} = \nu_t \left(\frac{\partial \overline{u_i}}{\partial x_j} + \frac{\partial \overline{u_j}}{\partial x_i} \right) - \frac{2}{3} k \delta_{ij} \tag{3.17}$$

where ν_t is the eddy viscosity, k is the turbulent kinetic energy ($k = \frac{1}{2}\overline{u_i' u_i'}$) and δ_{ij} is the Kronecker delta.

This relation extends into the 2-equation $k - \epsilon$ turbulence model which tracks the transport of k and ϵ (dissipation rate of k). The $k - \epsilon$ model is commonly used in industrial and environmental flow applications without adverse pressure gradients (Mansour et al., 1988). In the presence of an adverse pressure gradient (such as flow over aerofoils) the $k - \omega$ turbulence model (ω in this model is the *specific* dissipation rate of k) has been shown to be more reliable. While better in the near-wall region the $k - \omega$ model has been noted to be sensitive to the free-stream turbulence conditions (Kok, 2000) and unreliable away from the wall region.

A model by Menter (1994) introduced a blending function between the $k - \omega$ and the $k - \epsilon$ models to leverage the best of the $k - \omega$ model, which performs well in the near-wall region, and the $k - \epsilon$ in the far field (ANSYS Inc., 2013). This model also introduces a limiter on the production of k which was observed to be good in adverse pressure gradient regions (Menter, 1994). Menter's $k - \omega$ shear stress transport (SST) model has previously been used to model flow over an airfoil profile with a favourable comparison to observations (Menter, 1994) and

to directly simulate flow through a tidal rotor (Cao et al., 2019). Due to these benefits and the prior applications the $k-\omega$ SST model was used throughout this study. This model does have some limitations in the application to tidal turbines which have to be carefully considered. Specifically this model does not account for transitional flows and care must be taken to check that the flow is fully turbulent over the entire turbine blade. If it is not, then a four equation model such as the $\overline{Re_{\theta,t}}, \gamma$ may be required (Menter et al., 2006). This model introduces two additional transport variables $\overline{Re_{\theta,t}}$ (momentum thickness Reynolds number) and γ (fraction of time where the flow is fully turbulent) to simulate transitional flows.

3.2.2 Numerical Solution Process

Solver

The three-dimensional RANS equations were solved using a pressure-based finite volume solver by the commercial software ANSYS Fluent 19.2 (ANSYS Inc., 2018). The solution approach first solves the velocity field then uses a pressure correction, derived from the continuity and momentum equations, such that the velocity field is corrected by the pressure. This correction is then applied back onto the model and the process is repeated until the convergence criteria is met. This convergence criteria is based on the scaled residuals of the conserved variables. These residuals are defined as the average magnitude of the error within each cell (for example continuity error) scaled by a term representative of the flux of the variable through the domain. For this study a residual magnitude of $<$ 1e$-$10 was targeted.

Spatial discretisation

A requirement of the solver is a spatial discretisation of the flow domain. This was performed using a meshing approach with ANSYS ICEM (ANSYS Inc., 2013) and ANSYS Workbench (ANSYS Inc., 2018) for structured and unstructured meshes respectively. The finite volume method employed by ANSYS Fluent applies the integral form of the conservation equations to each cell as a control volume. The integral form can be written as

$$\int_V \frac{\partial \rho\phi}{\partial t} dV + \oint \rho\phi \mathbf{u} \cdot d\mathbf{A} = \oint \Gamma_\phi \nabla\phi \cdot d\mathbf{A} + \int_V S_\phi dV \tag{3.18}$$

for a scalar quantity ϕ within a control volume V, where Γ_ϕ is a diffusion coefficient for ϕ, S_ϕ is the volumetric source term and $\mathbf{A}$ is the surface area vector around the control volume such that $\mathbf{A} = A \cdot \mathbf{n}$, where A is the cell area and $\mathbf{n}$ is the surface normal vector. This equation is applied to the control volume such that

$$\frac{\partial \rho\phi}{\partial t} V + \sum_f^{N_{\text{faces}}} \rho\phi_f \mathbf{u}_f \cdot \mathbf{A}_f = \sum_f^{N_{\text{faces}}} \Gamma_\phi \nabla\phi_f \cdot \mathbf{A}_f + S_\phi V \tag{3.19}$$

where N_{faces} is the number of cell faces, f is the face and the sub-script f refers to the value passing through the face. Values of ϕ are stored at the cell centre however ϕ is required at the cell faces. The solver is therefore required to interpolate values to the cell faces. This is achieved using a second-order upwind scheme in ANSYS Fluent.

Temporal discretisation

Sometimes features of the flow can be considered steady in the time, however in certain cases, such as explicitly resolving the flow around a turbine blade, the unsteady flow features are of interest. This requires a discretisation of the solver in the time domain, both steady and unsteady models are considered in this thesis.

The time evolution of ϕ can be expressed as

$$\frac{\partial \phi}{\partial t} = F(\phi) \tag{3.20}$$

where the function F incorporates any spatial discretisation. This can be approximated to the first and second-order using

$$\frac{\phi^{n+1} - \phi^n}{\Delta t} = F(\phi) \qquad \text{and} \qquad \frac{3\phi^{n+1} - 4\phi^n + \phi^{n-1}}{2\Delta t} = F(\phi) \tag{3.21}$$

where Δt is the time-step size, n is the value at the current time-step and $n+1$ and $n-1$ are the values at the following and previous time-steps, respectively. For a forward marching explicit time integration scheme, the solver is restricted to a maximum time-step size defined by the Courant-Friedrich-Lewy condition (CFL). This condition states that

$$C = \Delta t \sum_{i=1}^{N} \frac{u_{x_i}}{\Delta x_i} \leq 1 \tag{3.22}$$

where C is the Courant number, Δx_i is the length across the cell in the x_i direction and u_{x_i} is the velocity in the x_i direction. This condition is not restrictive when using an iterative approach to solve for time (implicit scheme). This can be achieved using a backward differencing appraoch such that Equation 3.21 becomes

$$\frac{\phi^{n+1} - \phi^n}{\Delta t} = F(\phi^{n+1}). \tag{3.23}$$

A second-order implicit approach was used for the unsteady simulation in this thesis. Further information on the numerical scheme can be found in the Fluent

science manual (ANSYS Inc., 2018).

3.2.3 Multiple reference frames

A common way to simulate a turbine within the RANS framework in a computationally efficient way is to solve the equations over multiple reference frames (MRF). This method reduces the computational complexity of the model and allows a steady solver to be used by separating the computational domain into stationary and a moving reference frames. For the application to turbines the inner region is solved in a rotating reference frame equal to the turbine's angular speed, and the outer region (encasing the inner region) is solved in the absolute reference frame; a transformation between the reference frames is applied at zone boundaries allowing fluxes between them. Using this method ensures that the rotor remains still in the simulation allowing a single mesh to be used. If the outer domain is also radially symmetric, the mesh can be further simplified by reducing it to a wedge containing one blade with periodic boundary conditions at the sides, significantly reducing the model size.

Within the moving domain a relative velocity formulation is used, transforming the following

$$\mathbf{u_{rel}} = \mathbf{u} - \omega \times \mathbf{r} \tag{3.24}$$

where $\mathbf{u_{rel}}$ is the relative velocity vector, $\mathbf{u}$ is the velocity vector in the stationary reference frame, ω is the angular velocity of the internal reference frame and $\mathbf{r}$ is the position vector from the origin of the moving reference frame.

While this method is computationally efficient, the application is limited to radially symmetric inner domains that are steady in time. Consequently this

method is unable to fully resolve the helical vortex which forms at the blade tip, vibration loading (Liu et al., 2016) and is not applicable in anisotropic blockage conditions or in sheared profiles. Nevertheless this method is a useful tool for sensitivity analysis of designs (Siddiqui et al., 2016) and in the initialisation of sliding mesh simulations due to the speed of the model (ANSYS Inc., 2013).

3.2.4 Sliding mesh

The sliding mesh approach is the most computationally expensive method and accurate method for the simulation of a turbine presented in this thesis. This transient model explicitly resolves the rotation of a turbine through the decomposition of the domain into rotating and stationary sub-domains, similar to the MRF model. Unlike the MRF model the inner domain rotates, sliding within the outer domain. Consequently, the sliding mesh interface is nonconformal between the domains requiring fluxes to be interpolated across the interface. Care is required in the mesh development at the interface zones to ensure that the resolution on either side of the interface is approximately the same to assist in the interpolation. The sliding mesh is capable of resolving the higher detailed physical flow processes around a tidal turbine such as the helical vortex at the blade tip and flow separation. Unlike the MRF approach, this methodology is able to capture non-radially symmetric flow features, such as a rectangular domain and spatially varying inflow conditions.

Chapter 4

End-wall constrained turbine fences

This chapter presents a numerical analysis of a four turbine long fence, examining the effect of reduced inter-turbine spacing on performance variation along the fence. It presents a potential solution to reduce this variation through a constraint to turbine fence end-losses by using a fence end-wall to reduce bypass flow and improve efficiency.

Section 4.2 explains the numerical model used to analyse the fence and design the end-wall, Section 4.3 examines the effect that altering the inter-turbine spacing has on a turbine fence of four turbines and Section 4.4 presents an end-wall design methodology and characterises fence performance with an end-wall. A summary of the results is outlined in Section 4.5. The work presented in this chapter is closely linked with the experimental results presented in Chapter 5.

4.1 Introduction

As discussed in Section 2.2, the local blockage effect, first analysed by Nishino and Willden (2012), shows that decreasing the inter-turbine spacing (s) can result in an increase in turbine power production. This result has been verified both numerically (Schluntz and Willden, 2015; Vogel and Willden, 2017) and experimentally (Cooke, 2016; McNaughton et al., 2019). While these results reaffirm the key findings from Nishino and Willden (2012), deviation from the theoretical framework arises at the end of the turbine fences due to an around-fence flow diversion, decreasing outboard turbine performance. This effect is not captured in Nishino and Willden (2012) due to the assumption of a "long fence", but is observed in the experiments of Cooke (2016) and the numerical analysis of Vogel and Willden (2017). Some improvements to the theory based modelling for shorter turbines fences were made by Nishino and Willden (2013) who considered a two-scale approach to model shorter fences. However, this work did not include consideration for fence end-effects.

While long fences may be desirable theoretically, shorter fences are more likely to be designed as technology develops. Within shorter fences, the losses resulting from flow diversion around the outer turbines and insufficient flow confinement may represent a more significant percentage of the total fence power and, therefore, should not be ignored when optimising overall performance. The work presented in this chapter aims to further understand this "end-effect" by investigating flow diversion at varied inter-turbine spacing for a short fence of four turbines. Following this, a turbine fence end-wall is designed and characterised numerically as a possible mitigation strategy for end-losses. The end-wall is investigated further

experimentally in Chapter 5.

Floating turbine structures require sufficient buoyancy to support the turbines, nacelles and connecting structure, this may require a buoyancy aid with relatively large displacement. There is an opportunity that this support structure in floating tidal fences can be designed to re-align flow normal to the turbine and potentially improve power output. This would take the form of a turbine fence end-wall, which provides a physical barrier to reduce the flow diversion around the ends of a fence. End-walls may improve performance by confining the flow in a similar way to ducting around a single turbine. The impact of single-turbine ducting has been investigated previously (Belloni, 2013; Fleming and Willden, 2016). These studies concluded that placing ducting around a turbine's circumference improved the power density through the rotors; however, this improvement was not as effective as increasing rotor diameter to match the ducting opening size. Unlike the single turbine ducting, which requires additional material to be added to the turbine, this study focuses on providing confinement at the turbine fence scale by utilising buoyancy aids that are necessary for a floating tidal turbine platform. Positioning an end-wall adjacent to the end turbine imposes a lateral force that helps channel flow that would otherwise have been diverted around the end of the fence through the fence.

This study presents the design of a turbine fence end-wall for a four turbine fence composed of 1.2 m diameter (D) turbines (modelled as two turbines with a symmetry plane). These turbines were designed for deployment in a four turbine fence configuration by Cao et al. (2018) and manufactured and first tested at floWave by McNaughton et al. (2019). Towing tank testing of the end-wall at the SSPA facility is discussed in Chapter 5.

4.2 Methods

A four turbine fence was analysed at varied inter-turbine spacings using the RANS-BE model detailed in Section 3.1.2. Following this, a parametric study was undertaken to determine an end-wall geometry which improved the total power output from the fence.

The turbine modelled in this study was that designed by Cao et al. (2018), which uses a FX-84-W-140 aerofoil profile with a thickened trailing edge (defined as per Xu et al. (2014)) across the entire blade span. The aerofoil two-dimensional lift and drag coefficients were supplied by Cao from CFD simulation and used in the present study to model the turbines through a RANS embedded BE actuator disk (AD) method. The aerofoil data compared favourably to lift and drag measurements at $Re = 1.6 \times 10^6$ from Bertagnolio et al. (2001) in Cao et al. (2018) and achieved a peak lift to drag ratio at 6°. The three-bladed rotor of Cao et al. (2018) achieves a $C_p = 0.580$ at a design $\lambda = 7$ for a blockage of 11.8%.

4.2.1 Numerical model

The incompressible RANS equations were solved numerically using the computational fluid dynamics (CFD) software ANSYS Fluent 15.0 (ANSYS Inc., 2013). The $k - \omega$ shear stress transport (SST) turbulence model of Menter (1994), with updated coefficients from Menter et al. (2003), was implemented. This modelling approach blends the $k-\omega$ model, which performs well in the near-wall region, with the $k - \epsilon$ model in the far-field. The model also implements a k limiter function which is well suited to adverse pressure gradients, such as in the wake of a turbine. This approach has previously been used to model flow over an aerofoil profile

with a favourable comparison to observations (Menter, 1994) and to simulate flows through tidal rotors (Liu and Hu, 2015; Kolekar and Banerjee, 2015; Cao et al., 2019).

A blade element actuator disk model was embedded into the RANS solver through an in-house subroutine developed by McIntosh et al. (2011). This steady analysis method utilises the zero thickness fan internal boundary condition available in Fluent, with the pressure drop and downstream swirl velocity determined by solving the blade element equations. The subroutine samples the simulated flow field in each cell within the rotor's swept area and used the blade element approach to incorporate the hydrofoil properties (in the form of the 2D lift and drag coefficients c_l and c_d) of the turbine blades to determine the local pressure drop and swirl velocity. The Glauert (1935) tip correction model was applied to account for the required blade tip flow losses and reduce the loading on the outboard sections of the blades.

A structured computational mesh was developed using ANSYS ICEM (ANSYS Inc., 2012). The cross-section of the rectangular numerical domain matches the cross-section of the SSPA towing tank facility where physical experiments were conducted (Chapter 5); 10 m wide ($8.33D$), 5 m deep ($4.17D$) and the domain is 36 m long ($30D$) in the stream-wise direction as illustrated in Figure 4.1. Two turbines of 1.2 m diameter were placed perpendicular to the flow 12 m downstream ($10D$) of the inlet and towards the side of the tank. The turbine centres are located 1 m below the simulated free surface which is represented by a symmetry plane. A uniform velocity profile with inflow speed 0.8 m/s and turbulence intensity of 8% was specified at the velocity inlet; turbulence intensity decayed to approximately 5% at the rotor plane. A zero-gradient pressure outlet was specified on the

downstream boundary. Symmetry boundary conditions were applied to the upper, lower and side boundaries. By placing the turbines towards a side boundary using a symmetry condition we enable a simulation of a fence of four turbines placed centrally within a 20 m ($16.67D$) wide channel, thus halving the computational cost of the full simulation (the same approach was used for the physical experiments in Chapter 5). The inter-turbine spacing s was one of the design variables in the study and so varied; the turbine-symmetry plane spacing was set to $s/2$ so that the four turbine fence was uniformly spaced. The global blockage of the fence was 4.5%.

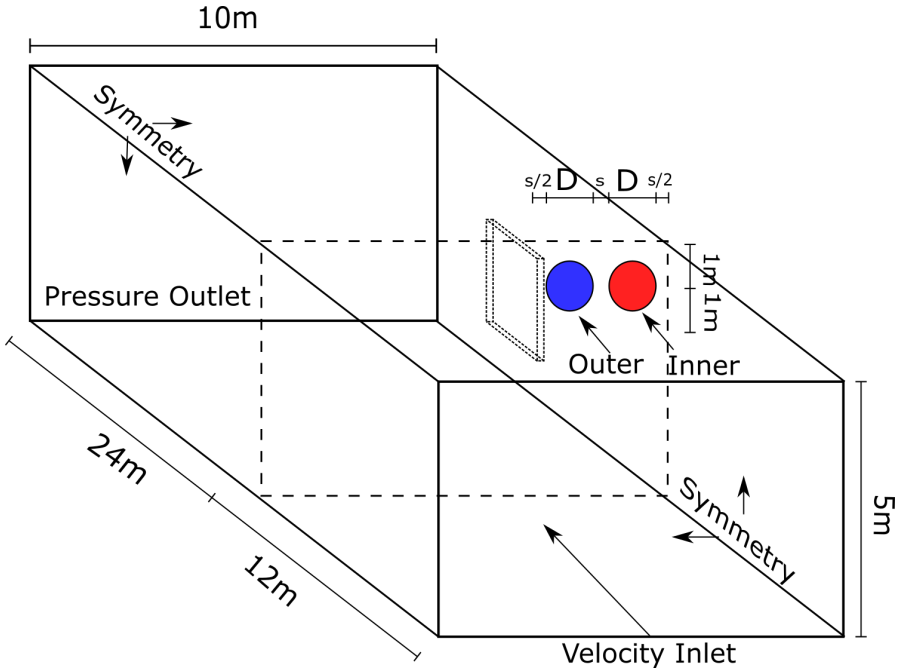

Figure 4.1: Computational domain and boundary conditions for the numerical model, $D = 1.2$ m is the turbine diameter and s is the inter-turbine spacing. Inner (red) and outer (blue) turbines are represented by disks, with the streamlined fence end wall shown beyond the outer blue disk.

Table 4.1: Fence-averaged C_p and C_t for different inter-turbine meshes (two turbines, $D = 1.2$ m, $s/D = 0.25$). *Highest resolution model was used as the baseline for error calculations.

Max element size (D)	C_p	C_t	% C_p Error *	% C_t Error *
0.0083	0.580	1.199	-	-
0.0125	0.579	1.199	-0.163%	-0.051%
0.0167	0.576	1.196	-0.691%	-0.245%

4.2.2 Mesh convergence

The disk meshing strategy followed that of Cao et al. (2019) which was developed for the same turbine model. The disk mesh used an identically parameterised structured mesh constructed using a total of 15 million hexahedral elements (27 million elements when the end-wall was included) with the rotor disk discretised using 82 elements in the radial direction and 164 around the azimuth. The mesh growth rate was limited to 1.05 across the rotors and in the stream-wise direction.

Mesh refinement, reported in Table 4.1, was investigated in the zone between the turbines, with the element size growth rate fixed at 1.05 and the maximum element size varied. Table 4.1 reports the integrated power and thrust coefficients for three inter-turbine mesh resolutions. Results illustrate close agreement between all three resolutions with the finest element sizes of $0.0083D$ and $0.0125D$ exhibiting less than 0.163% relative difference in simulated fence-averaged C_p. A smaller relative error of less than 0.051% was observed for the fence-averaged turbine thrust coefficient, C_t. Due to the close agreement in performance coefficients, a maximum element size of $0.0125D$ was selected for the inter-turbine spacing.

Mesh independence around the end-wall was also examined. As part of this study, both the non-dimensional wall distance, y^+, and maximum stream-wise

element length, L_{el}, were varied. y^+ is defined by

$$y^+ = \frac{u_* y}{\nu} \tag{4.1}$$

where y is the distance from the wall u_* is the friction velocity defined as

$$u_* = \sqrt{\frac{\tau_w}{\rho}} \tag{4.2}$$

where τ_w is the wall shear stress. y^+ is an important criterion for resolving the loading on the end-wall as the $k-\omega$ SST turbulence model is used in this study. This model is capable of implementing a log-law wall function to simulate the boundary layer where there is insufficient detail to resolve the viscous sub-layer, requiring y^+ as an input. Further discussion of this model can be found in Section 3.2.1.1 and in Menter (1994).

Convergence was determined based on the wall's two-dimensional (pressure based) lift coefficient at mid-rotor depth following:

$$C_l = \frac{\oint (p\widehat{n} \cdot \widehat{k}) d\mathbf{S}}{\frac{1}{2}\rho u_\infty^2 L_c} \tag{4.3}$$

where $\widehat{n}$ is the surface normal unit vector, $\widehat{k}$ is the unit vector in the direction of lift which is perpendicular to the flow, $\mathbf{S}$ is the curve around the perimeter of the hydrofoil end-wall, u_∞ is the free-stream velocity and L_c is its chord length. As shown in Figure 4.2, meshes with y^+ between 100-225 converge to similar values. The smallest y^+ tested diverges from the other results, likely due to the scale of resolution introducing cells that overlap with the buffer layer between the viscous sublayer and the log layer; ANSYS Inc. (2013) recommends that y^+ be no less

than 30 for this reason. Accordingly, a mesh with L_{el}/L_c of 0.056 that achieves a maximum y^+ of 100 at 50% chord was adopted for the end-wall mesh in the present study.

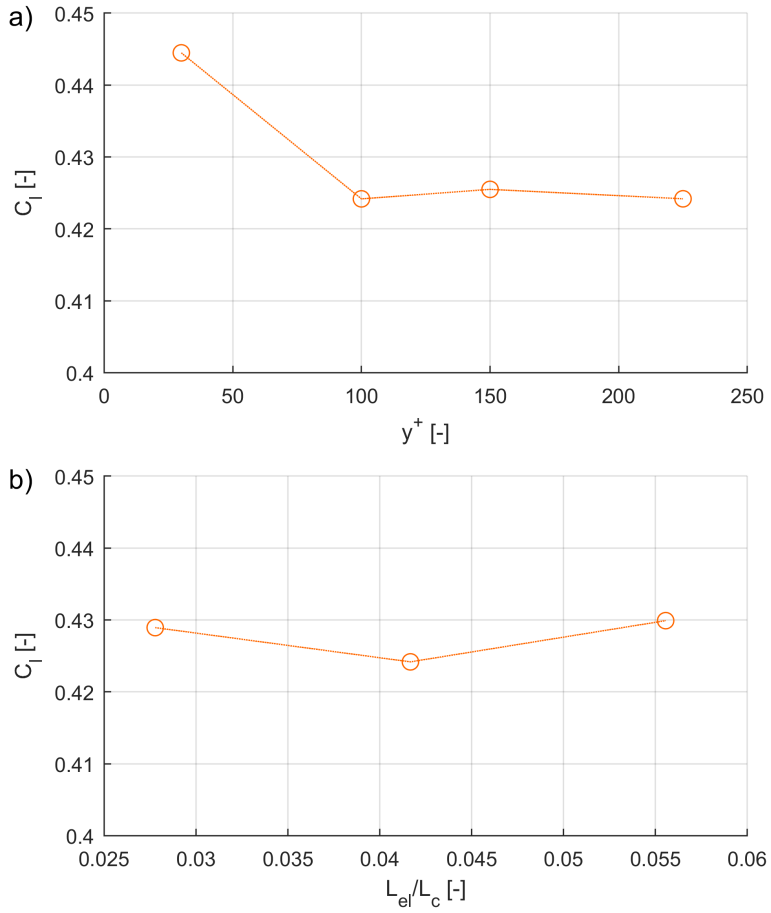

Figure 4.2: End-wall model mesh convergence of C_l as defined by Equation 4.3 (a) with non-dimensional wall normal distance y^+ at 50% chord, fixed $L_{el}/L_c = 0.056$, and (b) with minimum element length to chord length ratio L_{el}/L_c, and fixed first wall normal dimension (achieves maximum $y^+ = 100$ at 50% chord).

4.2.3 Root bending moment extraction

Individual blade root bending moments were calculated from the RANS-BE model by applying the blade element equations to the converged velocity field. This process first involved identifying the velocity components and radial positions of each node within the structured mesh over the turbine swept area. At each blade angle (θ) and radial location (r) the velocity components from the RANS-BE model were transformed into normal, radial and azimuthal components following,

$$\begin{bmatrix} u_{norm} \\ u_r \\ u_\theta \end{bmatrix} = \begin{bmatrix} 1 & 0 & 0 \\ 0 & \cos(\theta) & -\sin(\theta) \\ 0 & \sin(\theta) & \cos(\theta) \end{bmatrix} \begin{bmatrix} u_x \\ u_y \\ u_z \end{bmatrix} \tag{4.4}$$

where u_x, u_y and u_z are the velocities in the x, y and z directions from the RANS-BE model and u_{norm}, u_r and u_θ are the transformed velocities normal to the turbine plane, in the radial direction and in the azimuth direction. The blade element equations from Section 3.1.2 (Equation 3.3 and 3.4) were rearranged to solve for the angle of attack (α) and velocity magnitude (W). Using this information c_l and c_d from the 2D hydrofoil data set could be extracted and transformed into stream-wise and rotational thrust coefficients, c_x and c_t,

$$\begin{aligned} c_x &= c_l \cos(\phi) + c_d \sin(\phi), \\ c_\theta &= c_l \sin(\phi) - c_d \cos(\phi) \end{aligned} \tag{4.5}$$

where ϕ is the sum of the angle of attack and the blade twist angle ($\phi = \alpha + \beta$). Forces per unit span in the stream-wise and rotational directions on each element

were calculated using

$$F_x = \frac{1}{2}\rho W^2 c_x c(r),$$
$$F_\theta = \frac{1}{2}\rho W^2 c_\theta c(r). \tag{4.6}$$

The bending moments about the hub were determined in the edge-wise (M_{EW}) and the flap-wise (M_{FW}) direction by integrating the loading along an annular segment following

$$M_{EW} = \int_{r_{hub}}^{R} F_\theta r dr, \quad M_{FW} = \int_{r_{hub}}^{R} F_x r dr. \tag{4.7}$$

This process was repeated for each azimuthal segment in the turbine swept area to extract the variation in root bending moment with the azimuthal position. Finally, the root bending moments were non-dimensionalised by

$$C_{FW} = \frac{N_b M_{FW}}{\frac{1}{2}\rho u_\infty^2 A_t R}, \quad C_{EW} = \frac{N_b M_{EW}}{\frac{1}{2}\rho u_\infty^2 A_t R} \tag{4.8}$$

where R is the turbine radius.

4.2.4 Model iteration methodology

Due to shifting inter-turbine spacing and varied end-wall designs, the tip-speed-ratio (λ) that achieves the highest average C_p (λ^*) changed across configurations. Therefore λ^* must be accurately calculated to facilitate the comparison of turbine performance across configurations. To limit this study's scope, inboard and outboard turbines are operated at the same λ (synchronised controls).

λ^* was determined by running a set of three simulations at different λ close to the expected optimal value based on previous studies by Cao et al. (2019). A

quadratic curve was then fit to the average turbine C_p output from the model and λ. The λ corresponding to the maximum C_p from this curve was used for the next simulation. The results from this iteration were compared to the approximated value from the quadratic curve; if the error between the values was less than 0.01%, this λ was adopted as λ^*. If this criterion was not met, the new iteration results were used to fit a curve to the three largest values of C_p, and the search process was repeated. This methodology helped determine the optimal operating point in the 100+ simulations examined as part of this study, taking advantage of the parallel computing resources available on the ARCUS cluster (ARC, 2022).

4.3 Effect of inter-turbine spacing on tidal fence performance

The effect of inter-turbine spacing was investigated to characterise the performance improvement from increased local blockage (B_l) and quantify the end-losses. Based on this analysis, a spacing was selected for further examination and physical testing.

4.3.1 Turbine performance

λ^* and the corresponding turbine C_p and C_t were found for six inter-turbine spacings, s, ranging between $0.25D$ to $2.333D$. The tip-speed-ratio was specified to be the same for all turbines within the fence. Fence-averaged results from these simulations are presented in Figure 4.3. As the fence spacing is decreased from $s = 2.333D$ ($B_l = 5.7\%$) to $s = 0.25D$ ($B_l = 15.1\%$), there is an increase in

fence-averaged C_p of 5.6%. To achieve this improvement C_t and λ^* increased by 6.0% and 4.5%, respectively. This concurs with Nishino and Willden (2012), who demonstrated for a fixed global blockage, B_g, that an increase in B_l can improve the fence's performance. The increased performance arises from the greater pressure gradient (thrust) that can be sustained across the rotor plane as turbine spacing is reduced and downstream flow expansion is constrained by neighbouring wakes and the free surface.

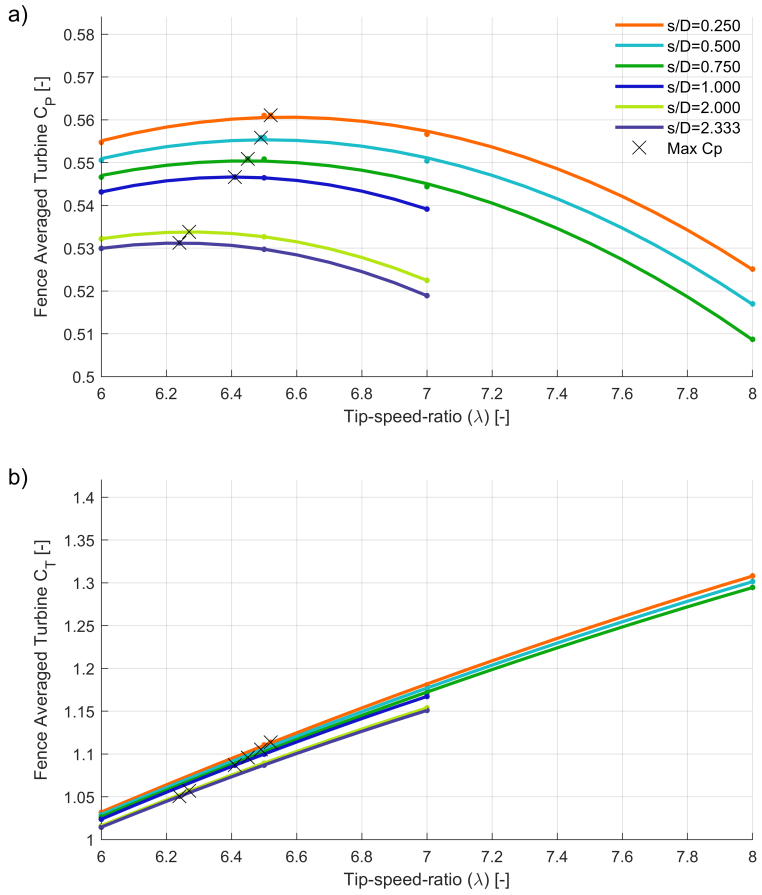

Figure 4.3: Variation of (a) average fence power coefficient, C_p, and (b) average fence thrust coefficient, C_t, with tip-speed-ratio, λ, as a function of inter-turbine spacing, s/D. The optimal operating point, λ^*, is marked on each curve with a black cross and the global blockage is constant at 4.5% for all cases.

Table 4.2: Turbine C_p and C_t at λ^* for varied inter-turbine spacing.

Spacing $[D]$	λ^*	$\mathbf{C_p}$			$\mathbf{C_t}$		
		Outer	**Inner**	**Average**	**Outer**	**Inner**	**Average**
0.250	6.52	0.553	0.569	0.561	1.108	1.119	1.114
0.500	6.49	0.548	0.564	0.556	1.099	1.111	1.105
0.750	6.45	0.543	0.559	0.551	1.090	1.102	1.096
1.000	6.41	0.539	0.554	0.547	1.081	1.093	1.087
2.000	6.27	0.530	0.538	0.534	1.054	1.060	1.057
2.333	6.24	0.528	0.534	0.531	1.048	1.053	1.051

C_p and C_t at λ^* for inner and outer turbines over a range of inter-turbine spacings are presented in Table 4.2. This table highlights that as spacing is reduced, C_p and C_t increase, so too does the disparity between inner and outer turbines (Figure 4.4). The inner turbines can achieve a slightly higher C_p (and corresponding C_t) than the outer turbines for all s/D due to the greater flow confinement effects experienced towards the centre of the fence; see Figure 4.4a and 4.4b. Wake expansion downstream of the inner turbines is laterally constrained by the presence of the wakes of the adjacent turbines, allowing larger stream-wise pressure gradients to be maintained through the wake, which in turn enables a greater pressure drop across each turbine improving their performance. Such lateral flow constraint is only present for the outer turbines as they pass the inner turbines, and so the reduced flow constraint for the outboard turbines presents as a fence end-loss. The resulting asymmetry can be quantified by a symmetry factor between the rotors, which we defined as:

$$\Phi_X = \frac{X_{inner} - X_{outer}}{X_{inner}} \tag{4.9}$$

where Φ is the symmetry factor for the parameter X, with positive values indicat-

ing a bias towards the inner turbines.

Figure 4.4 plots the variation in turbine symmetry factor as a function of inter-turbine spacing. Similar trends in the symmetry factor for both C_p and C_t are observed, with ΦC_p being more than twice that of ΦC_t. The smallest asymmetry between the turbines' performance was observed when they were most separated at $s = 2.33D$, although there still remained a 1.2% bias towards the inner turbine's performance due to the slight but differing local blockage of the inner and outer turbines even at this wide spacing.

A maximum was observed for Φ at $s = 0.75D$, with the inner turbine producing 2.9% more power and 1.1% more thrust. As turbine spacing decreases from $s = 0.75D$, the difference in power and thrust along the fence is slightly reduced. Examining the mass flow rate, Q, in Figure 4.4f provides some evidence of the interference effects experienced along the fence. Moving the turbines closer together results in a small increase in mass flux for the inner turbine due to the increased local blockage. The picture is more complex for the outer turbine with close spacing permitting increased mass flux, and competition between end-losses and constructive interference constraints resulting in a minimum flow rate at $s = 0.75D$. Examining the flow yaw angle in Figure 4.5 supports these results, with reducing yaw angles on the inner turbine as they are positioned closer together. Interplay between the constructive interaction of turbines and fence end-losses are responsible for the varied response of flux at decreased spacing for the outer turbine (highlighted in Figure 4.5). This figure shows an increased yaw over the outermost region of the outer turbine as the spacing decreases from $s = 2.33D$ to $s = 0.75D$, which outweighs the improvement on the inner most region due to improved local blockage. The yaw over the inner edge of the outer turbine contin-

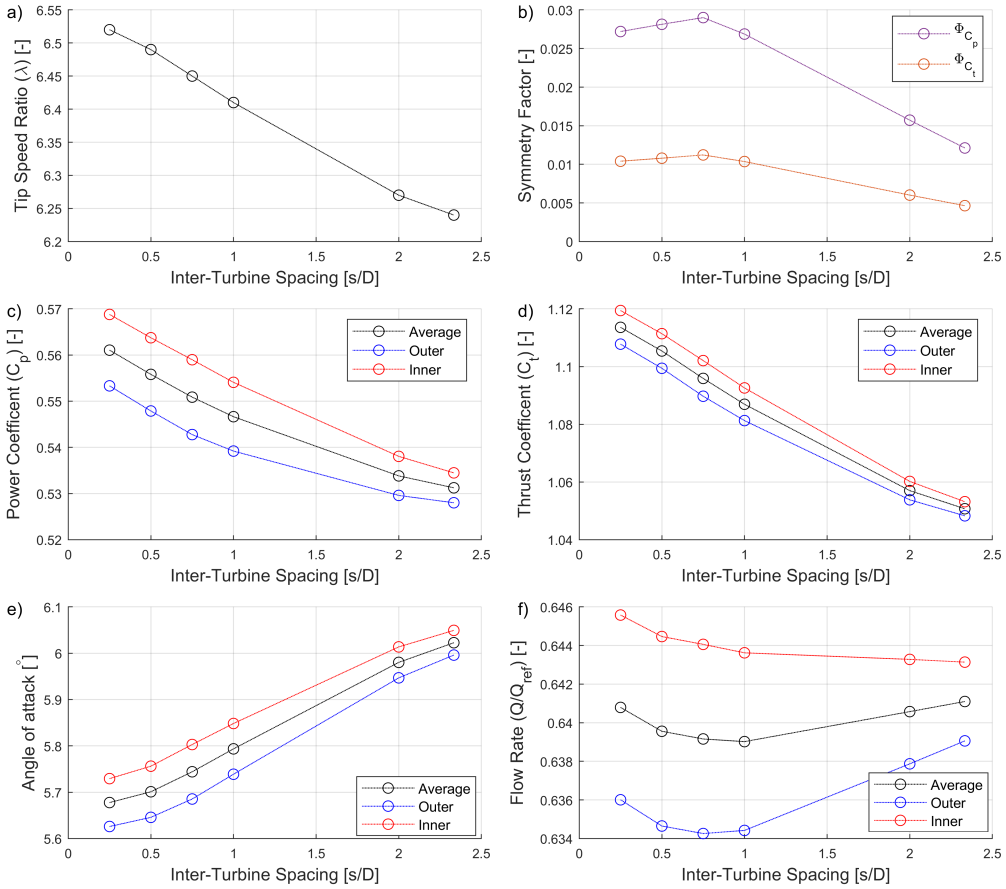

Figure 4.4: (a) λ^*, (b) Φ, (c) C_p, (d) C_t, (e) α, span-wise averaged between 0.3R-0.85R, and (f) turbine flow rate, Q, variation with inter-turbine spacing, s/D, at λ^* for maximum power at each spacing. Q_{ref} is the flow rate through each turbine with no flow resistance.

ues to reduce as the turbines move closer together and the turbine flux increases for $s < 0.75D$.

The changes in flow-rate with inter-turbine spacing are small, remembering that λ is re-tuned for each spacing. The increases in turbine thrust (and thus power), Figure 4.4d and 4.4c, are more substantial. The effect of turbine interference is to constrain the flow diversion around each turbine which helps to maintain a high flow rate. This enables a greater pressure drop to be achieved across each turbine

than would be possible in unconstrained flow. As the turbines are brought closer together, at a given operating point λ, their flow rate at first increases, which then allows an increase in the resistive force to be applied whilst still increasing power. The increase in λ to λ^* (Figure 4.3) for each s/D to achieve this greater resistive force (Figure 4.4c) results in the fence achieving a total flow rate that is broadly independent of s/D (Figure 4.4f).

It should be noted that while adjusting the operating point (tip-speed-ratio) as spacing is reduced, can help to bring the angle-of-attack distribution back towards the design point, changing angular speed does not change angle-of-attack uniformly along the blade and hence the resulting spanwise variation in angle-of-attack can be sub-optimal. Further performance enhancement is therefore achievable by redesign of the rotors to achieve optimum angle-of-attack along the entire length of the blade for the spacing in which they are to be deployed, see Vogel and Willden (2019). Figure 4.4e plots the effect of spacing on angle of attack averaged over the primary power producing region of the blades (0.3R-0.85R), where span-wise flow terms are small and the 2-dimensional flow assumption is valid. The optimal angle of attack for the single aerofoil section used in this study was 6°, close to the average α at the maximum spacing of $2.33D$. It can be noted that decreasing the spacing decreases the angle of attack after a correction to λ was made to extract the optimal power. The distance from $\alpha = 6°$ highlights a potential for further performance improvements with altered designs at closer spacings.

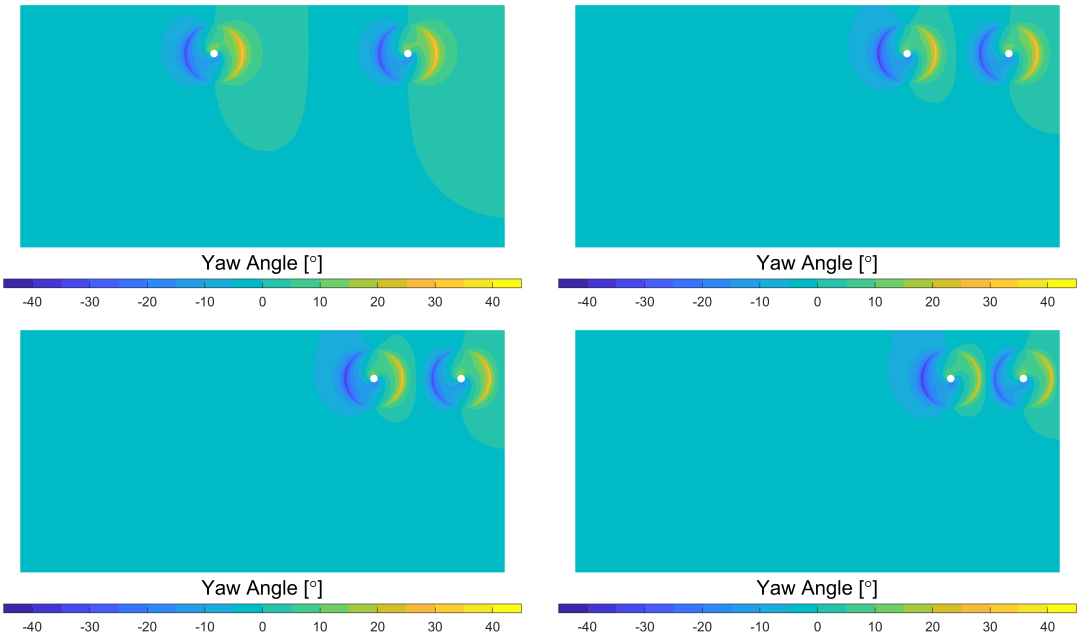

Figure 4.5: Yaw angle at the turbine plane for $s = 2.33D$ (top left), $s = 0.75D$ (top right), $s = 0.50D$ (bottom left) and $s = 0.25D$ (bottom right). Positive yaw is to the right.

4.3.2 Unsteady loading on turbine blades

Due to the non-uniform confinement between the inner and outer turbines and the local flow area's aspect ratio (nacelle of the turbine is $0.83D$ below the surface and $3.33D$ from the bottom of the domain), the flow is not axisymmetric about the nacelle leading to a positional variation in blade root bending moments through a rotation, this can be extracted from the RANS-BE model following the method from Section 4.2.3. Figure 4.6 plots the flap-wise (C_{FW}) and edge-wise (C_{EW}) root bending moment coefficients with inter-turbine spacing. The plot demonstrates that decreasing the inter-turbine spacing increases the root bending moments at all azimuthal angles and in both the edge-wise and flap-wise directions, with the inner turbine having greater bending loads than the outer turbine.

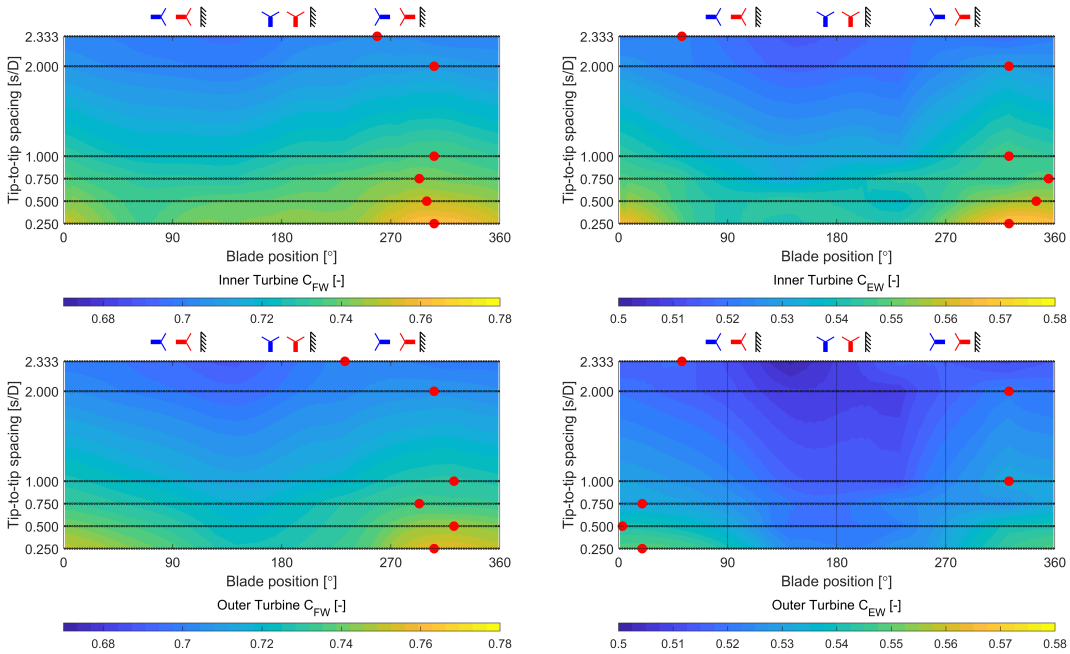

Figure 4.6: Azimuthal variation in flap-wise (left) and edge-wise (right) root bending moment coefficients with inter-turbine spacing for the inner (top) and outer (bottom) turbines. The red dots indicate the azimuthal position of maximum root bending moment. The illustrations at the top of each plot show the location of the blade (bold lines), with blue and red representing the outer and inner turbines respectively. Turbines are viewed from upstream so that flow is into the page and turbines rotate anti-clockwise.

For the inner turbine, the edge-wise and flap-wise moments are typically highest in the upper right quadrant of rotation just after the blade makes its nearest pass to the centre of the fence at 270°. As the blades pass through this region they experience an increased bypass flow speed, and hence higher loading, due to constructive interference with the counter-rotating turbine on the other side of the symmetry plane. A similar observation can be made for the flap-wise moments of the outer turbine as it rotates through the same quadrant; although the loading is due to constructive interference from the co-rotating inner turbine.

Both turbines experience elevated bending moments as blades rotate past the

upper symmetry boundary. Although the distance to this surface is not altered, these elevated loads increase as the inter-turbine spacing is reduced and the flow between the turbines is diverted into alternate flow passages causing accelerated bypass flow above the turbines.

For the outer turbine, there is a reduction (relative to the average root bending moments at a specified spacing) in the root bending moment as the blade sweeps the 90° to 200° portion of the rotation; this is due to the relief on flow constraint as the flow diverts around (Figure 4.5) and underneath the fence (Figure 4.7).

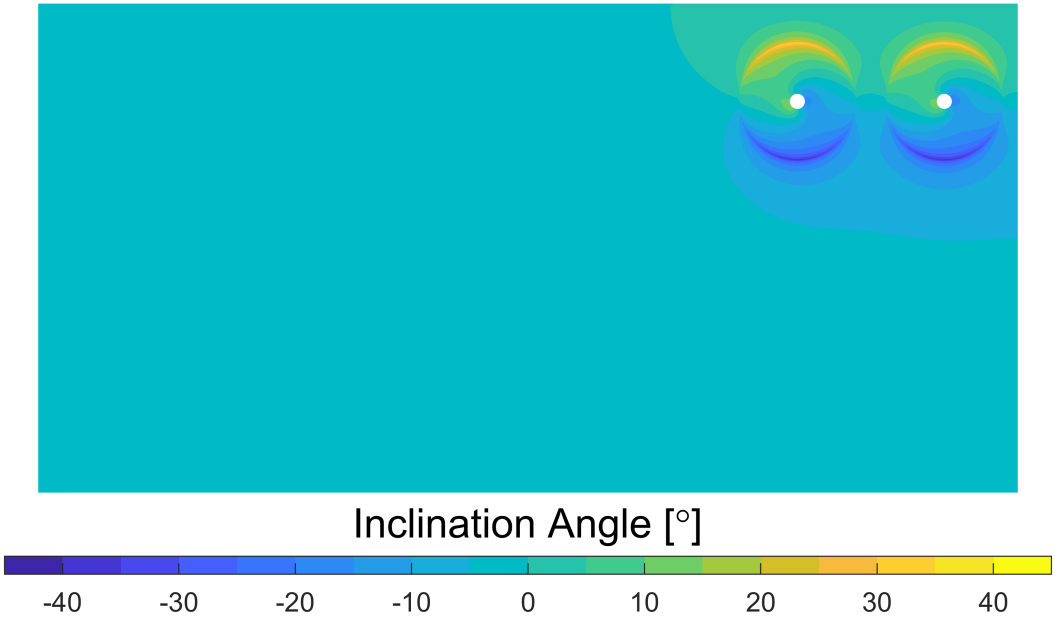

Figure 4.7: Inclination of flow at the turbine plane for s/D=0.25 with turbines operating at λ^*. Positive is up.

Using the results from the $s = 0.25D$ simulation at λ^*, the stream-wise velocity (u_x) through the rotor plane was extracted and decomposed into an annular averaged ($\langle u_x \rangle$) and a deviatoric component (u'_x) such that $u_x = \langle u_x \rangle + u'_x$. This metric indicated the angular and radial position where flow (as a proxy for loading

on the blades) is changed; in contrast, root bending moments only indicated the angular position of a change in load. The results of the velocity decomposition (u_x, $\langle u_x \rangle$, u'_x) are presented in Figure 4.8 for the inboard and outboard rotors. This figure highlights that there is a significantly reduced flow rate ($\langle u_x \rangle$) through the outer turbine when compared with the inner turbine. Higher u'_x for the inboard and outboard regions of the inner turbine and the inboard region of the outer turbine highlight the constructive interference effects between the turbines. At the outboard section of the outer turbine, bypass flow is yawed around the rotor, reducing the flow rate in the u_x direction (this can be observed in Figure 4.5).

4.4 Numerical design of turbine fence end-wall

Based on the results presented in Section 4.3, the minimum inter-turbine spacing of $s = 0.25D$ was selected for analysis with a end-wall. This spacing was chosen as it produced the highest power output from the spacings tested and a noticeable decrease in outer turbine performance relative to inner turbine performance was observed.

A parametric study of end-wall shape was carried out to determine whether an end-wall could be used to provide lateral flow constraint to improve flow alignment and reduce the loss in outer turbine performance at close spacing. Several end-wall cambers and thickness were investigated for a $1D$ long elliptical cross-section placed adjacent to the outer turbine at half the inter-turbine spacing (i.e., $0.125D$ tip-to-wall spacing) so that inner and outer turbines saw similar geometric constraints. The length of the end-wall was constrained by the maximum size that manufacturing allowed for the physical testing discussed in Chapter 5. The ellipse

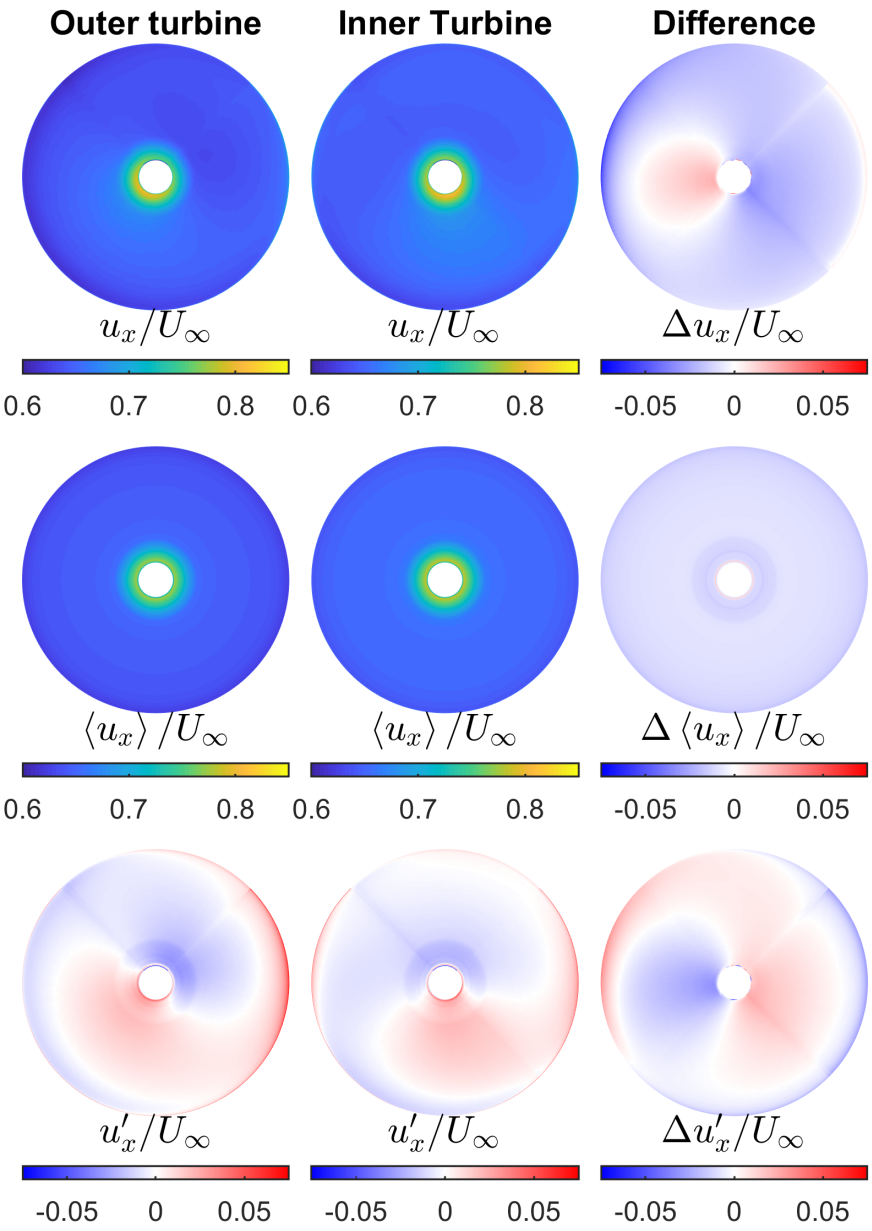

Figure 4.8: Total (top), azimuthally averaged (middle) and deviatoric (bottom) components of the stream-wise velocity at the outer (left) and inner (middle) turbines as well as the difference, Δ, of the inner turbine's velocity component minus the outer turbine's velocity components turbine (right) for $s = 0.25D$ spaced rotors operating at λ^*. The free-stream flow direction is into the page.

is centred on the plane of the rotor fence. A parabolic camber was applied to the ellipse's major axis. The bottom of the 2 m ($1.67D$) deep end-wall was rounded using a semi-circular section, with the depth set to be symmetric above and below the turbine's axis of rotation. For each end-wall design considered, λ^* was determined following the method outlined in Section 4.2.4. Three end-wall thicknesses ($0.05D$, $0.10D$ and $0.15D$) and five cambers (-4%, -2%, 0%, 2%, 4%) were tested, these cross-section profiles are presented in Figure 4.9. Positive camber implies that the end-wall's inner surface is more convex, and is achieved by displacing the leading and trailing edges of the cambered ellipse further outboard of the fence, so that the tip-to-wall spacing of $s/D = 0.125$ is maintained at mid-length of the ellipse.

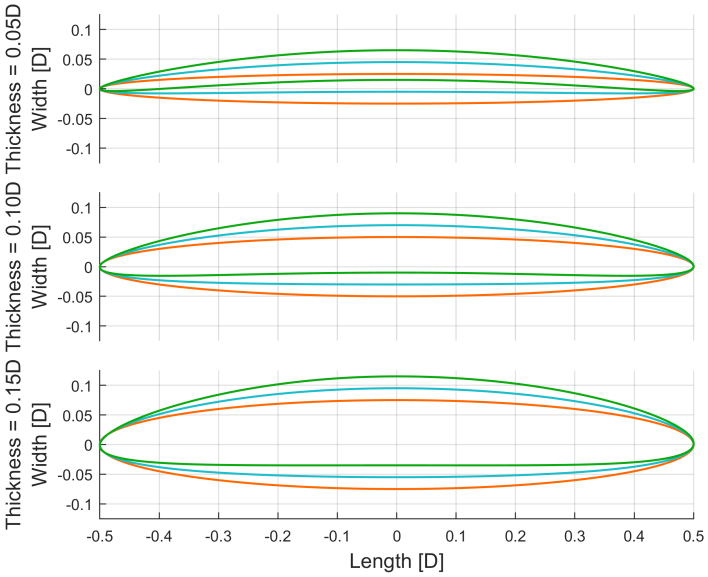

Figure 4.9: End-wall cross-section profiles for thicknesses of $0.05D$ (top), $0.10D$ (middle) and $0.15D$ (bottom) and cambers of 0% (orange), 2% (blue) and 4% (green).

4.4.1 Effect of end constraint on turbine performance

Four metrics were used to quantify end-walls performance, C_p, C_t, Φ_X and basin efficiency (η). η is a metric for the efficiency with which power is extracted, defined as the ratio between the power extracted from the flow (P) and the total power removed from the flow (from the turbine, wake mixing, support structure etc.). The formulation of Belloni (2013) was used to determine η following Equation 2.7. The performance of the fence with respect to these metrics is examined in this section.

4.4.2 Fence power

Fence power at λ^* for each end-wall profile, scaled by the optimal power coefficient achieved without a end-wall for the same spacing, is presented in Figure 4.10. Values greater than one indicate an improvement in fence power output. High positive camber (curvature of the end-wall nearest to the turbines is convex) and thicker end-walls produced greater power, with an increase of 3.95% for the highest end-wall camber and thickness (4% camber and 15% thickness). The performance of both turbines was improved, with a 5.59% increase in outer turbine power and a 2.36% increase for the inner turbine. Improvement in the fence performance can be credited to the increase in global blockage from the thicker end-wall and the end-wall improving flow alignment. The end-wall increases the mass flow rate through the turbines (4.6% and 2.8% increase for outer and inner turbines respectively) and improves the angle of attack on the turbine blades towards the blade tips. Figure 4.11 plots the impact on the flow yaw due to the presence of the end-wall. A significant reduction in flow diversion around the turbine fence is observed

adjacent to the end-wall's interior face. There are also minor improvements of the innermost turbine's flow alignment.

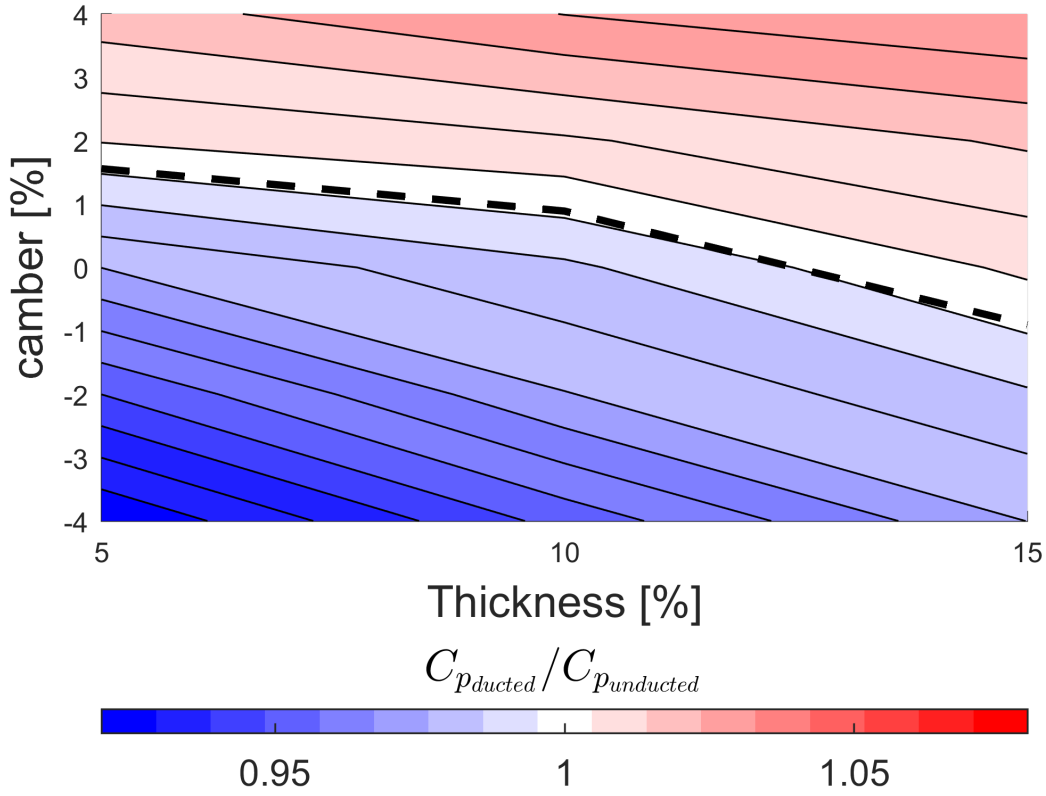

Figure 4.10: Fence averaged power with an end-wall at λ^* scaled by the without end-wall fence averaged power for s/D=0.25. The dashed line plots the region where the with and without end-wall power is the same.

4.4.3 Fence thrust

Across the parameter space investigated for the end-wall geometry, fence averaged thrust decreased relative to the no end-wall case (Figure 4.12); this is partly due to the lower λ^* of fences with end-walls. Improved flow alignment and mass flow rate due to the end-wall allows the outer turbine to operate in more uniform flow.

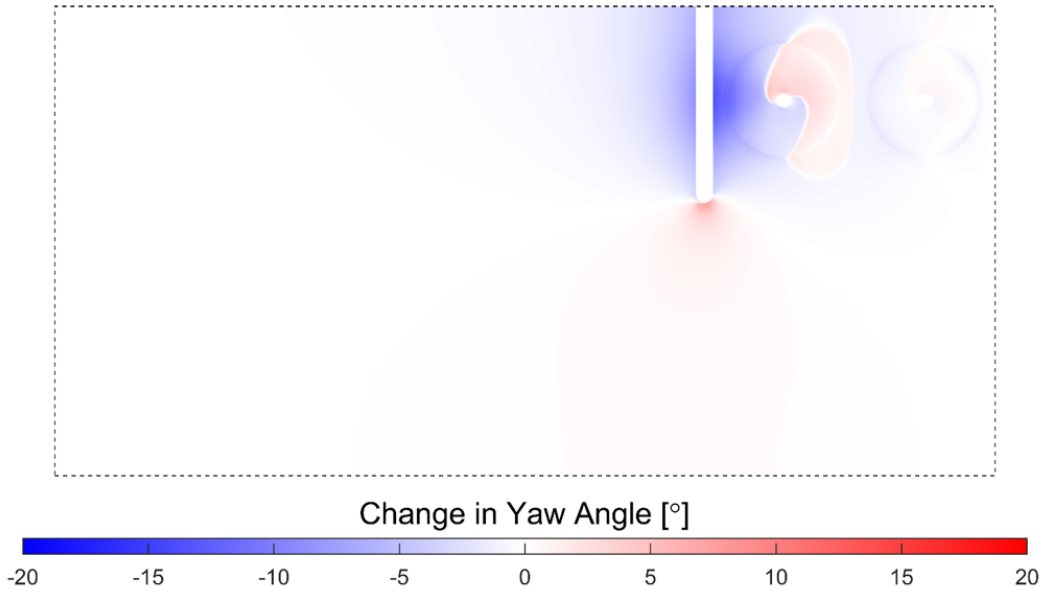

Figure 4.11: Change in yaw angle magnitude with the inclusion of an end-wall for a fence with $s = 0.25D$ turbine spacing operating at λ^* ($\lambda^* = 6.52$ without an end-wall and $\lambda^* = 6.37$ with an end-wall). Change in yaw angle magnitude is determined as the yaw angle with an end-wall minus the yaw angle without; a negative change in yaw angle magnitude indicates the flow is closer to normal to the turbine plane.

As a result, λ^* is reduced as is the thrust on the turbines. For the end-wall that achieved the highest C_p, the smallest reduction in thrust to the without end-wall case was observed; average turbine C_t decreased by 0.67%.

4.4.4 Fence basin efficiency

Basin efficiency brings together the two performance metrics (power and thrust) discussed previously, relating them as the efficiency of power extraction from the flow. Figure 4.13 plots the basin efficiency over the set of end-wall profiles investigated. Although turbine power is improved and thrust is reduced with the end-wall, the overall efficiency of energy extraction does not improve due to the par-

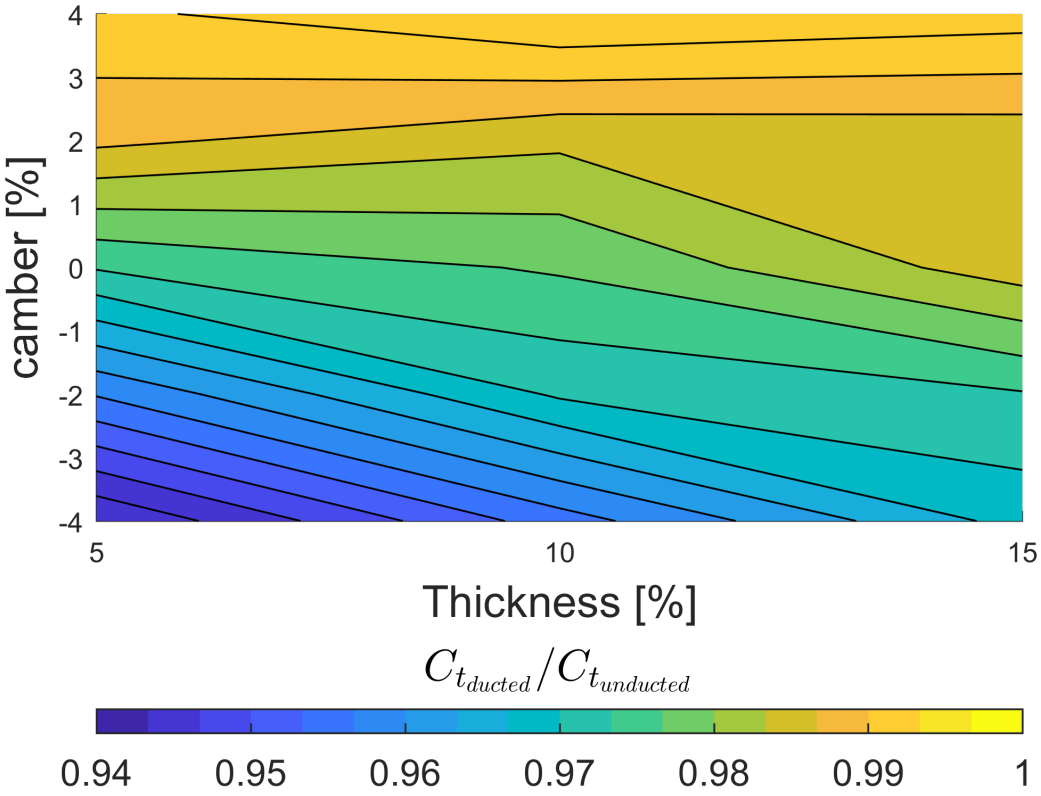

Figure 4.12: Fence averaged thrust with an end-wall at λ^* scaled by the without an end-wall fence averaged power for $s = 0.25D$.

asitic drag from the end-wall and associated energy dissipation in wake remixing. η decreased, relative to the without an end-wall case, for all end-walls examined due to the thrust contribution of the structure. Despite this, the impact on η was relatively small with $\eta_{ducted}/\eta_{unducted}$ remaining close to unity. A maximum basin efficiency with the end-wall of 99.93% the without end-wall value was achieved for a 2% camber and 10% thickness end-wall. The modest change in η is a result of the end-wall having a relatively small stream-wise thrust component, as shown in Figure 4.14. The stream-wise wall loading is a function of both thickness and camber, whereas the lateral wall loading is a function of camber and largely inde-

pendent of thickness. Overall the lateral force is significantly larger than the force in the stream-wise direction; this results from the exchange of momentum as the flow is realigned towards the free-stream direction by the end-wall.

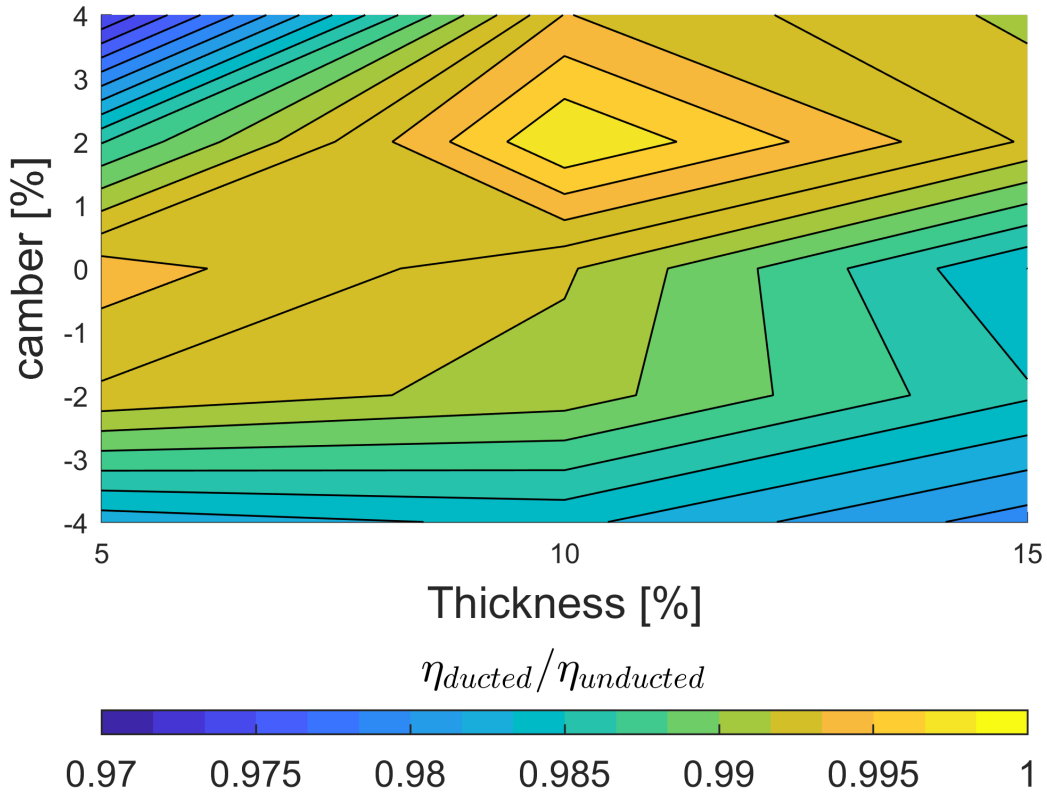

Figure 4.13: Fence basin efficiency (η) with an end-wall at λ^* scaled by the without an end-wall fence basin efficiency for s/D=0.25.

Increasing camber is correlated with increasing the stream-wise thrust due to the larger frontal area presented to the flow and separation occurring on the more highly cambered profiles. Separation is more prevalent with thinner profiles due to the sharper curvature at the leading edge resulting in increased drag; this is demonstrated by the sharp increase in the stream-wise thrust curve with camber for the 5% thickness end-wall in Figure 4.14. This highlights the importance of

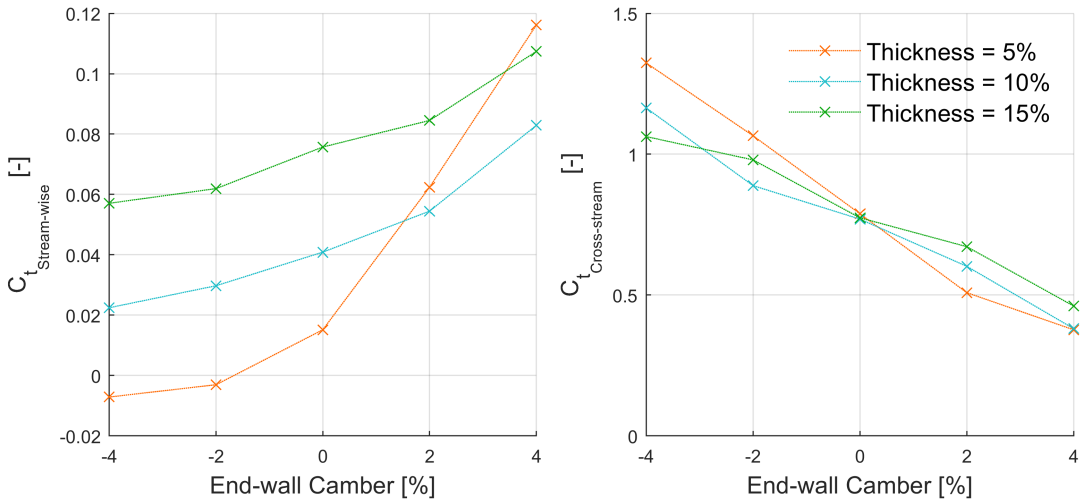

Figure 4.14: Force coefficients, normalised by the free-stream momentum flux through a turbine, acting on the end-wall in the stream-wise (left) and cross-stream (right) direction for a variety of wall cambers and thicknesses, with the turbines operating at λ^*. Positive stream-wise thrust is in the free-stream flow direction and positive cross-stream thrust is away from the centre of the fence.

end-wall thickness to avoid flow separation which was also observed by Fleming and Willden (2016) in their analysis of various turbine ducting shapes. Figure 4.15b and Figure 4.15e plot the flow field at hub height around a profile of 4% camber at 5% and 15% thickness, respectively. The plot shows flow separation at the leading edge of the thinner end-wall and delayed flow separation for the thicker wall, supporting the observations of Fleming and Willden (2016).

Figure 4.15 also shows an improvement in flow symmetry about the centre-line of the turbine with the 4% camber end-wall. An increase in bypass flow speed is observed at the outboard section of the fence when the end-wall is in place, more closely resembling the inner side's bypass flow field. The improved bypass flow speed is a function of the lateral confinement, which is observed to be smaller when the end-walls camber is lower (Figure 4.15d, Figure 4.15e and Figure 4.15f).

A similar bypass flow is observed between matched camber profiles (but varied thickness), suggesting that lateral confinement is not strongly influenced by end-wall thickness. This is confirmed by Figure 4.14, which shows similar lateral force across profile thicknesses.

4.4.5 Fence symmetry factor

The symmetry factor was used to analyse the thrust and power distribution along the fence, where positive values indicate higher inner turbine loading. As observed for the fence without an end-wall in Section 4.3, the ΦC_p and ΦC_t are offset by a constant value; for conciseness, only ΦC_p is plotted in Figure 4.16. This plot shows most end-wall profiles continue to bias the inner turbine; however, the thickest (15%) and most positively cambered (4%) profile biased the outboard turbine by 0.4% .The ability to make the flow more uniform across the fence with an end-wall means that approaches which design turbines for uniform blockage ratios, e.g. McIntosh et al. (2011); Schluntz and Willden (2015); Cao et al. (2019) can also be applied to shorter fences of turbines.

4.4.6 End-wall profile selection

Table 4.3: C_p and C_t at λ^* for a four turbine fence at a spacing of $s = 0.25D$ with and without an end-wall of $1D$ length, 4% camber and 15% thickness.

	No End-wall		With End-wall	
	C_p	C_t	C_p	C_t
Inner Turbine	0.569	1.119	0.582	1.107
Outer Turbine	0.553	1.108	0.584	1.108
Average	0.561	1.114	0.583	1.108
Symmetry Factor	2.72%	1.04%	-0.35%	-0.08%

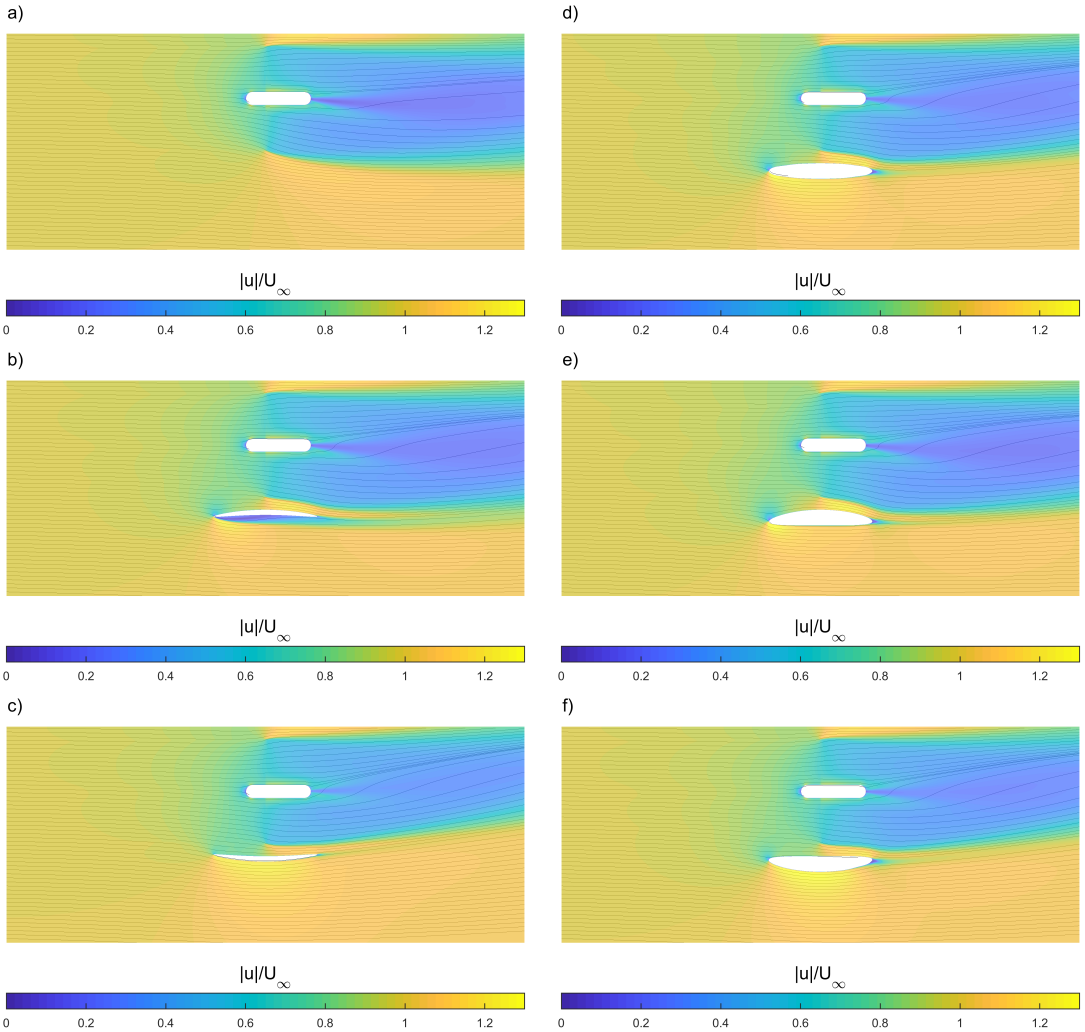

Figure 4.15: A plan view of the outboard turbine and side wall at the hub height showing the non-dimensional flow speed $|u|/u_\infty$ field for operation without an end-wall (a), an end-wall of 4% camber and 5% thickness (b), -4% camber and 5% thickness (c), 0% camber and 15% thickness (d), 4% camber and 15% thickness (e) and -4% camber and 15% thickness (f).

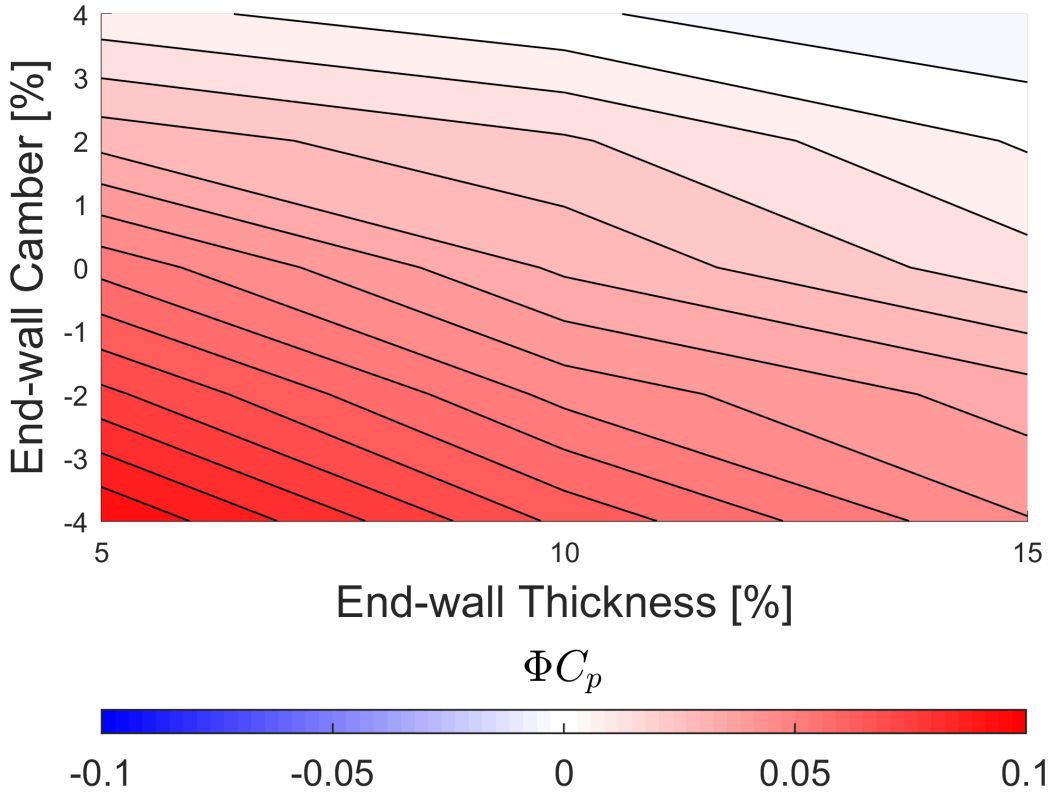

Figure 4.16: ΦC_p over a range of end-wall cambers and thickness at λ^* for a turbine spacing of $s = 0.25D$.

An end-wall of stream-wise length D, 15% thickness and positively cambered by 4% was determined to be the best candidate geometry for the four turbine fence with $0.25D$ tip-to-tip spacing based on the performance metrics examined in this section. When the end-wall is at a $0.125D$ tip-to-wall spacing, it provides sufficient lateral constraint to increase the power and decrease turbine thrust; this is quantified in Table 4.3. The wall profile selected was both the thickest and most heavily cambered of the geometries analysed. It is anticipated that thicker and more heavily cambered profiles will not significantly improve performance due to the increased stream-wise load they experience (decreasing η) and shifting of the

power bias towards the outboard turbine (negative ΦC_t and ΦC_p).

4.4.7 Unsteady loading on turbine blades

Following the methodology used in Section 4.3.2 differences in the azimuthally averaged ($\langle u_x \rangle$) and deviatoric components (u'_x) of the stream-wise velocity through inboard and outboard turbines are presented in Figure 4.17. The difference in total velocity (u_x) suggests that the outer turbine's proximity to the end-wall could introduce some unsteady blade loading as the blade passes. Comparing the difference in azimuthally averaged velocity between the inner and outer turbines ($\Delta \langle u_x \rangle$) from Figure 4.8 (no end-wall) and Figure 4.17 (with end-wall) shows a reduced disparity in turbine flux. This indicates that the end-wall has reduced the bypass losses and forced more flow through the outer turbine's swept area.

Figure 4.18 demonstrates the influence of the end-wall on the stream-wise flow through the turbine plane. As can be observed in this plot, flow is accelerated between the end-wall and the turbine to be faster than the bypass flow between the inner and outer turbines; this demonstrates the end-wall's effectiveness in reducing end-losses and highlights potential for increased loading over this region. Alongside the increase in flow speed, the end-wall increases the flap-wise blade root bending moment as the blade passes the end-wall (Figure 4.19). However, the average load and load amplitude over a rotation is smaller than the without end-wall case (Table 4.4). In the edge-wise direction, the outer turbine loading appears to be offset from the without end-wall case, this may be due to the increased mass flux through the majority of the turbine swept area and the change in λ^* required when the end-wall is installed.

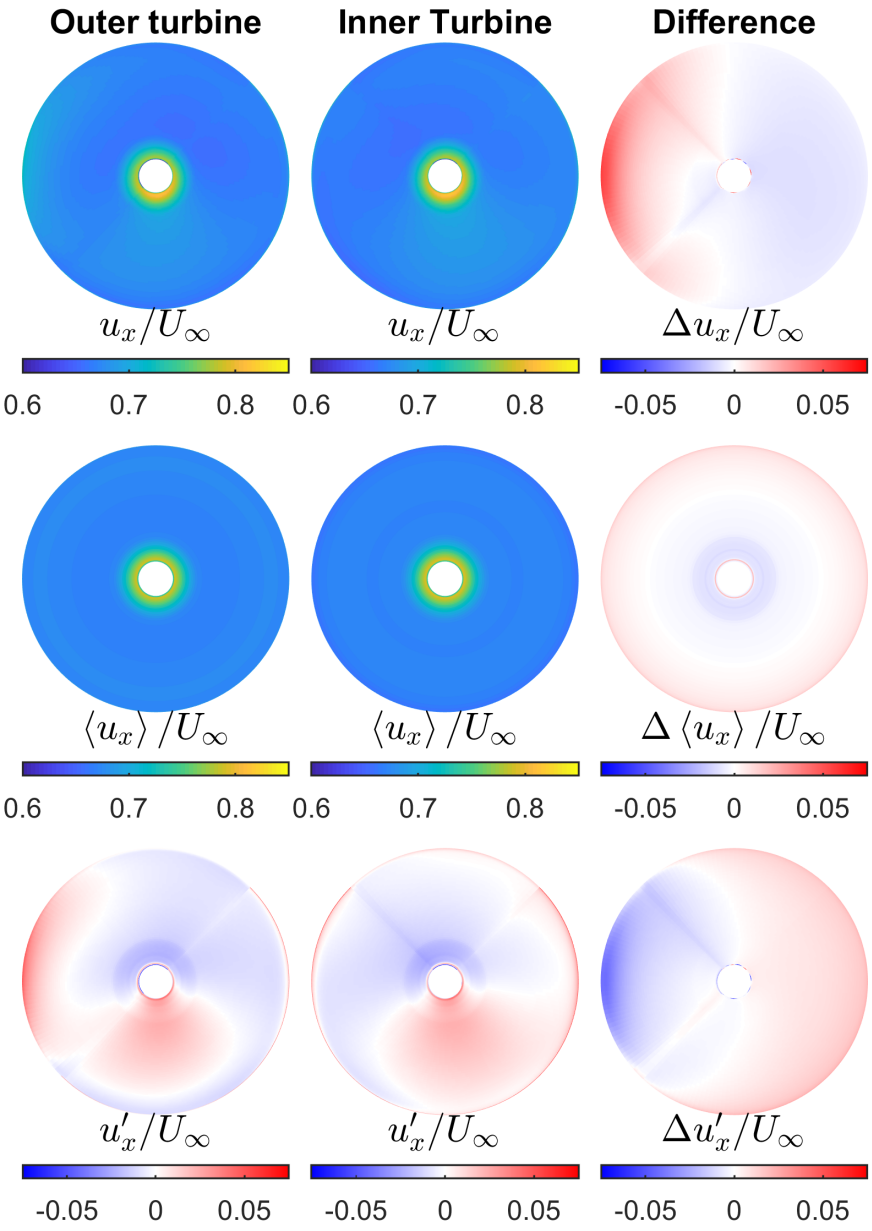

Figure 4.17: Total (top), azimuthally averaged (middle) and deviatoric (bottom) components of the stream-wise velocity at the inner (left) and outer (middle) turbines as well as the difference, Δ, of the inner turbine's velocity component minus the outer turbine's velocity components turbine (right) for $s = 0.25D$ spaced rotors operating at λ^* with a end-wall. The free-stream flow direction is into the page.

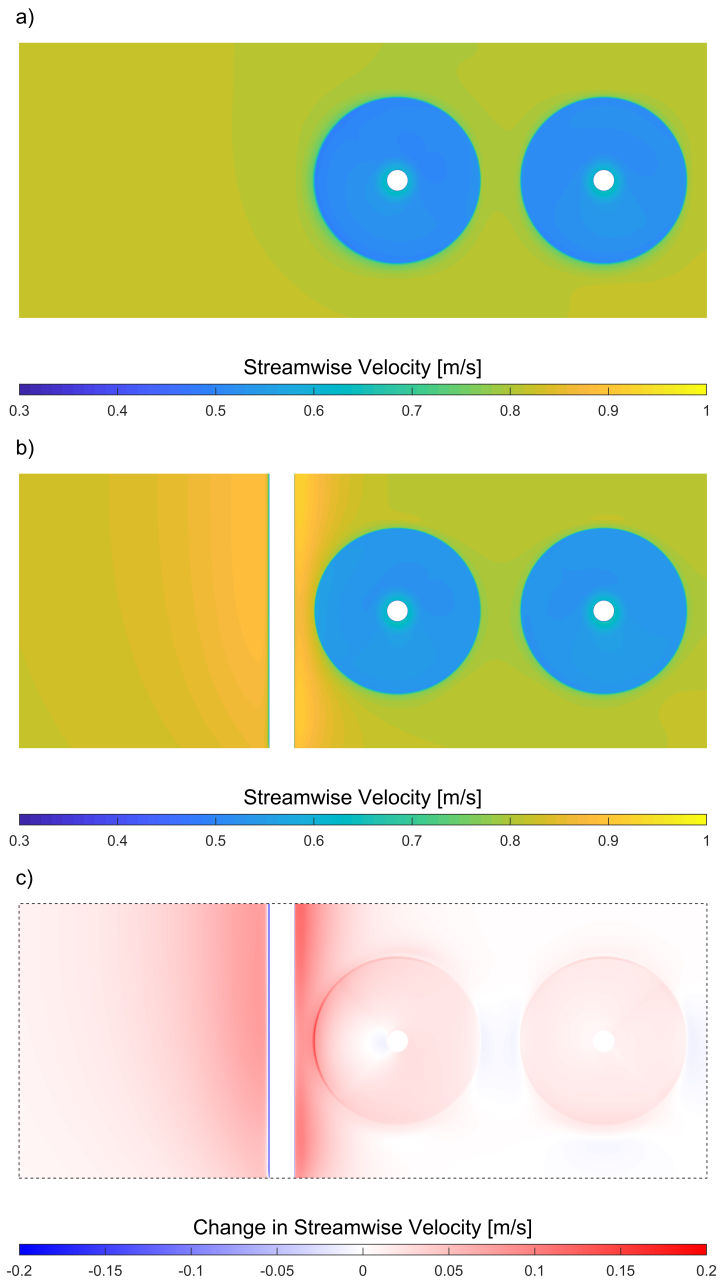

Figure 4.18: Stream-wise flow velocity through the turbine plane for a fence with $s = 0.25D$ turbine spacing operating at λ^* without an end-wall (a), with an end-wall of 15% thickness and 4% camber (b) and the difference, determined as the flow velocity with end-wall minus the flow velocity without (c). The free-stream flow direction is into the page.

Table 4.4: Comparison of root bending moment between the inner and outer turbines with and without a end-wall

Bending Direction	Turbine	Without end-wall			With end-wall		
		min	max	mean	min	max	mean
Flap-wise root bending (C_{FW})	Inner	0.736	0.764	0.748	0.723	0.753	0.737
	Outer	0.726	0.756	0.741	0.729	0.750	0.738
	Difference	0.010	0.008	0.007	-0.006	0.004	-0.001
Edge-wise root bending (C_{EW})	Inner	0.540	0.571	0.552	0.551	0.588	0.566
	Outer	0.523	0.550	0.537	0.552	0.584	0.567
	Difference	0.017	0.021	0.015	0.000	0.005	-0.001

The change in loading around the azimuth for the inner turbine is similar to that of the outer turbine in the edge-wise direction, with constant changes in loading at all angular positions. For the flap-wise direction this shift is negative, a result of the lower λ^* relative to the without end-wall case. The increased mass flux and change in λ^* also appears to increase the edge-wise root bending moment of this turbine.

The impact of the end-wall also reduced the difference in magnitude between the root bending moment for outer and inner turbines, meaning throughout the life cycle of the fence, similar fatigue damage will occur between the turbines. This is useful for improving the structure's design life estimate as there is balanced degradation of the turbines across the fence.

4.5 Conclusions

Analysis of a fence of four 1.2 m diameter turbines at varied inter-turbine spacings was undertaken. Decreasing the spacing between the turbines from $s = 2.33D$ to $s = 0.25D$ was shown to increase the fence's performance by 5.6%. A smaller improvement in the outboard turbine's performance (relative to the inboard turbine)

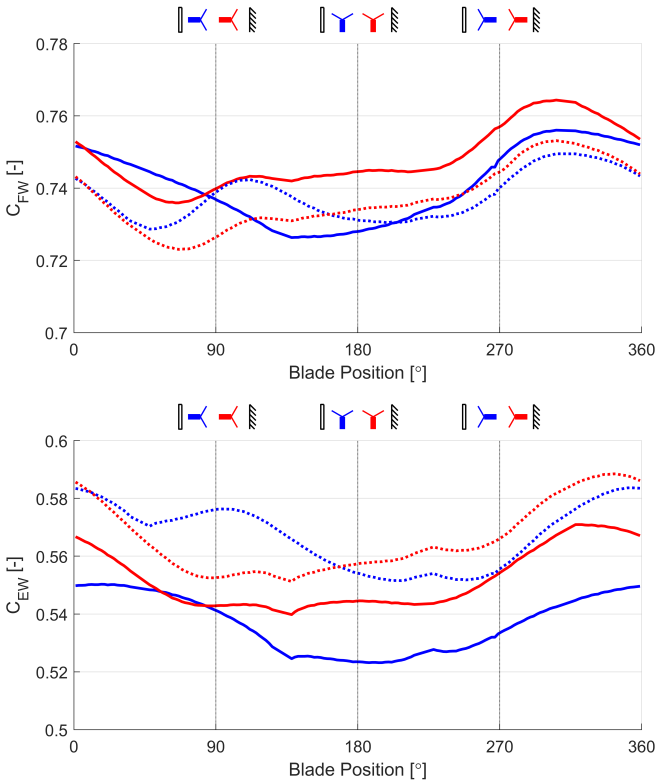

Figure 4.19: Flap-wise (top) and edge-wise (bottom) root bending moment for inboard (red) and outboard (blue) turbines operating at λ^* at $s = 0.25D$. Solid lines represent the without end-wall case and the dotted line represent the with end-wall case. The three illustrations at the top of each plot show the location of the blade (in bold) in the domain, with blue and red representing the outboard and inboard turbines.

was observed as the turbines were placed closer together, with the greatest imbalance occurring at $s = 0.75D$. This spacing produced the largest relative difference in loading between the inboard and outboard turbines due to fence end-losses being larger than the constructive interference from local blockage. As the spacing decreased further, the pressure drop over the turbine increased due to improved local blockage. This result suggests that there are spacings which give higher imbalances between the inboard and outboard turbine loading. These spacings

may not necessarily be the closest, indicating that designers may wish to consider inter-turbine spacing if trying to balance fatigue along a fence. It was hypothesised that the fence end-loss could be reduced by introducing a fence end-wall, which could correct the skewed flow towards the ends of a fence, mimicking the effect of additional turbines in a longer fence.

A parametric study of the effect of thickness and camber of an elliptical cross-sectioned end-wall of length ($1D$) was undertaken for an inter-turbine spacing of $0.25D$. The end-wall was able to improve the power of all turbines in the fence, with fence C_p improving by 3.95%. This was achieved by better aligning the approach flow to the fence, such that turbines operated in closer to uniform flow. This improvement in turbine performance coincided with a small reduction in thrust owing, in part, to the reduction in λ^*. As a result, the impact on the overall basin efficiency (which included the parasitic power removed from the flow by the end-wall) was small, with reductions between 0.07% and 3% relative to the no end-wall case.

The end-wall reduced the difference in root bending moments between the inboard and outboard turbines bringing the averaged loading closer together and balancing the turbine fatigue across the rotors in the fence. While this work is promising in terms of improved performance, further investigation into integrating the end-wall into the BE turbine blade design methodology may further improve performance. The improvements observed here are based solely on adjusting λ and inter-turbine spacing; further enhancement of the power output could be achieved by designing the turbine for the specific blockage conditions as shown by Schluntz and Willden (2015). The rotors used in this model were designed for a global blockage (B_g) of 0.142 and local blockage of 0.377 (Cao et al., 2019); however,

blockage conditions analysed in this study are far lower than this, with a B_g of 0.045 and B_l of between 0.057-0.168. The optimal shape of the turbine blades is expected to change as the global blockage is reduced by a factor of three. Furthermore, the operating conditions examined in this study restricted λ to be the same for all turbines along the fence. It is expected that, given the different flow conditions between the inboard and outboard rotors, altering λ along the fence would improve performance.

Chapter 5

Experimental testing of an end-wall constrained turbine fence

This chapter expands on the numerical analysis of the end-wall from Chapter 4 through an experimental study of a candidate geometry. This experiment is carried out with two closely spaced turbines between an end-wall and the sidewall of a towing tank (representative of a symmetry plane), facilitating a comparison to the numerical results of the four turbine fence.

Section 5.2 explains the experimental setup and manufacture of the end-wall, Section 5.3 and Section 5.4 present the results from the towing tank experiments and compares them to the numerical results from Chapter 4 and Section 5.5 discusses potential sources of error in both the numerical and experimental model.

5.1 Introduction

Details considering local blockage and the reasoning for installing a turbine fence end-wall have previously been discussed in Chapter 4. This section is limited to introducing the experimental testing and the comparison to numerical results.

Physical testing of tidal turbines is a necessary step in the development and eventual implementation of tidal turbine technology. Through physical testing a comparison can be made to numerical results to validate their accuracy and underlying assumptions. This work seeks to compare the RANS-BE results from Chapter 4 with towing tank tests conducted at the SSPA test facility in Gothenburg, Sweden. Analysis of RANS-BE and experimental results has previously been conducted by Olczak et al. (2016) who examined the thrust and wake characteristics over a single turbine and multiple arrays configurations, including a fence. The comparison showed that for a turbine fence, the RANS-BE model over predicted thrust loading by between 3-12% depending on location. In addition to investigating the end-wall improvement, this works looks to extend the comparison which was made by Olczak et al. (2016) through additional comparison data with experiments also conducted at larger geometric scale with lower Re dependence. In addition to thrust measurements, the turbines were instrumented to measure torque, speed and angular positions, with each turbine blade instrumented to collect edge-wise and flap-wise blade root bending moments (r/R=0.175).

The end-wall was instrumented to collect stream-wise and cross-stream loads; however, due to a strain gauge failure in the stream-wise direction, only cross-stream loads were measured. Limitations on the number of available test slots over the testing program also restricted the analysis to only consider one end-wall

geometry (length D, 15% thickness and 4% camber) and inter-turbine spacing ($s = 0.25D$).

Details on the manufacture of the turbines used in this experiment can be found in Cao et al. (2019) and results from initial testing at the FloWave test facility in Edinburgh can be found in McNaughton et al. (2019). The focus of the previous work by Cao et al. (2019) and McNaughton et al. (2019) has been on constructive interference through the exploitation of the local blockage effect. This work focuses on fence end-losses, using the experimental results from McNaughton et al. (2021) to firstly quantify the fence end-losses before new experimental results are presented for the end-wall constrained fence. The results in this chapter were collected alongside McNaughton et al. (2021) and are the author's own original work.

5.2 Experimental methodology

The methodology presented in this section is relevant to the towing test tanks with an end-wall; further detail on the testing procedure and results for the without end-wall towing tank tests can be found in McNaughton et al. (2021). A total of ten tests were conducted across seven λ ranging between 5.7 and 7.1 for the turbine fence with end-wall. Duplicate testing at three λ close to λ^* were run to confirm the results and quantify the uncertainty.

5.2.1 Experimental facility

Experimental tests were conducted at the SSPA towing tank facility in Gothenburg, Sweden. This testing was part of the MaRINET2-funded ATHENA project,

results on the impact of inter-turbine spacing on fence performance have already been reported in McNaughton et al. (2021). The towing tank cross section matched the computational cross section (discussed in Section 4.2), measuring 10 m wide, 5 m deep and 240 m long.

Two turbines of 1.2 m (D) diameter were deployed in a co-planar arrangement as per Figure 5.1 with a tip-to-tip spacing of $0.25D$ and a tip-to-wall spacing of $0.125D$, matching the dimensions analysed in the numerical component of this study. Each turbine was supported from above by a tower located $0.33D$ behind the turbine plane. The tank wall was used as a symmetry plane, allowing only two turbines to be tested while emulating a four turbine fence. The end-wall that was tested had a thickness of $0.15D$ and a camber of $0.04D$. The bottom of the end-wall was positioned 2 m ($1.67D$) below the water surface and the edges were rounded to reduce drag. The turbines were submerged to a hub depth of 1 m and thus were symmetrically placed about the end-wall mid-depth.

Torque and thrust data were collected from a transducer on the drive shaft of each turbine. The root of each turbine blade was strain gauged to monitor the edge-wise and flap-wise root bending moments. Additional strain gauges were attached to the end-wall supports to measure the cross-stream forces acting on the wall.

Following some initial checks for Reynolds independence of the turbine performance, the testing speed was increased from 0.8 m/s (used in the RANS-BE model) to 1 m/s (McNaughton et al., 2021). Reynolds independence was checked through a comparison of $C_p - \lambda$ curves at 0.8, 0.9 and 1 m/s. The towing carriage was accelerated at a rate of 0.05 m/s^2, providing a minimum of 90 seconds of usable data for each run. A minimum settling time of 10 minutes was observed

between tests, with tests running approximately every 20 minutes.

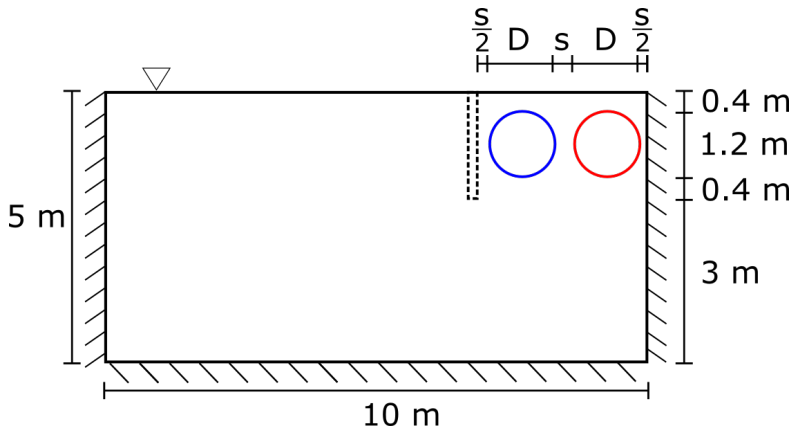

Figure 5.1: Diagram of the SSPA towing tank experimental setup. D is the turbine diameter of 1.2 m and s is the inter-turbine spacing of $0.25D$. The red and blue circles are the swept area of the inboard turbine and outboard turbines respectively and the dotted line is the turbine fence end-wall.

5.2.2 Prototype manufacture

Loading on the end-wall was estimated from the RANS-BE model to be 300 N in the cross-stream direction and 10 N in the stream-wise direction at λ^* (Section 4.4.3); these loads were used for the structural design of the wall. A conservative assumption that the load acted at the end-walls unsupported tip was used to estimate bending on the end-wall and support structure (Figure 5.2). Checks for shear, axial and bending loads were performed at critical locations in the frame to determine its capacity. This design's critical loading case occurred during installation if it were suspended by a single one of the two connecting members. In this scenario, one of the steel frame's connecting plates was 91% of its capacity. To avoid this loading condition, the wall was carefully rigged to distribute the 3600 N self-weight as it was placed into the water. The purple rigging equipment is visible

in Figure 5.2.

The end-wall was constructed using a Computer Numerical Controlled router (CNC) to shape it into four segments. The segments were formed by layering sheets of marine grade plywood and cutting away the excess material to the appropriate size. Hollow sections on the internal faces of the wall were added to allow a steel frame to be inserted as well as lead weights. 80 kg of lead weights were added to offset the buoyancy of the structure so that it was approximately neutrally-buoyant when assembled. The wooden surface was coated in a marine grade epoxy and boltholes, which held the wood to the steel frame, were filled with sealant. Whilst every effort was made to ensure a smooth finish, the nature of the wooden material and epoxy resulted in some surface roughness on the exterior of the end-wall which will have increased the skin friction drag on the structure. The steel frame was constructed from 3 mm thick 50 mm square hollow sections. Strain gauges were attached to the top of the supports, allowing measurements of the force acting in the cross-stream direction to be calculated. An image of the partially assembled end-wall is presented in Figure 5.2.

5.2.3 Processing of root bending moment from strain gauge data

A methodology for processing the phase averaged root bending moment was developed. This method was able to distil the time signal on the 90 second data recording into a single azimuthal variation in root bending moments through averaging the experimental data into 1° bins. Triplicate data was used when possible as the three identical blades on each turbine were instrumented. Integrated results

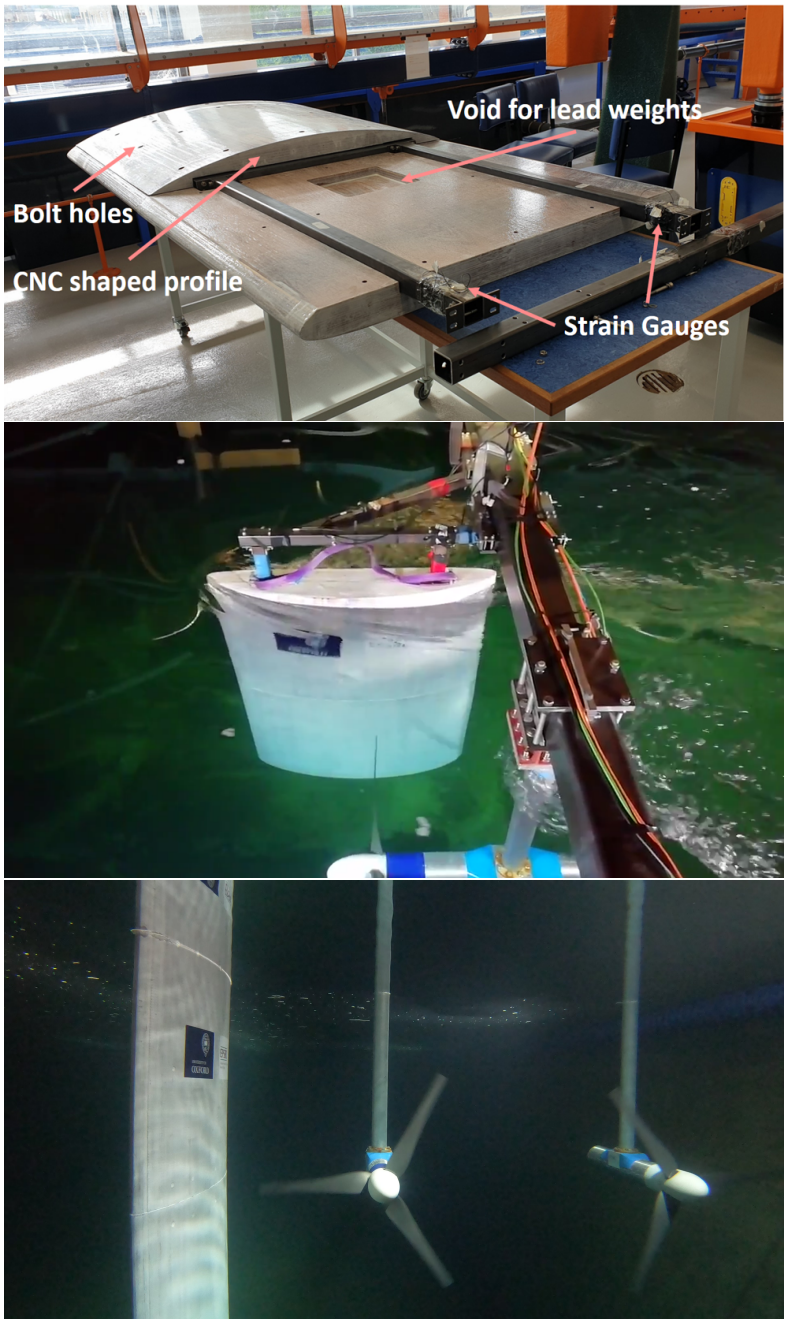

Figure 5.2: Partially assembled end-wall showing the steel frame, voids for lead weights and the locations of the strain gauges (top), installed end-wall and support structure (middle) and front view of the installed end-wall in the turbine fence (bottom).

were compared to the thrust and torque transducer data and scaled to have an internally consistent results set. The thrust and torque transducer data is preferenced when comparing the signals due to the external calibration of this piece of equipment. The processing method is outlined below.

Zeroing

Blade root bending moment data were first processed by removing the zero offsets from the strain gauges in the root bending moment sensors and the thrust and torque transducer. This was to account for any changes in the sensors' baseline due to variations in temperature or other environmental factors over the experiment. Zero offsets were recorded before each test run.

Azimuthal Averaging

Next, an azimuthal average was calculated for each blade and each bending direction by averaging the root bending moment in 1° bins. A blade averaged value was also derived from the thrust and torque transducer data following

$$M^*_{FW} = \frac{T}{N_b} r_T, \quad M^*_{EW} = \frac{Q_t}{N_b} \tag{5.1}$$

where M^*_{FW} and M^*_{EW} are the blade averaged flap-wise and edge-wise root bending moment from the thrust and torque transducer, Q_t is the torque, and r_T is the distance from the centre of the turbine to the line of action on the blade in the thrust direction. r_T was derived numerically from the blade resolved simulations of Cao et al. (2019) to be 0.4 m.

Scaling

Each strain gauge was scaled such that the average measurement from the thrust and torque transducer matched the resultant sum from the blade root bend-

ing moment sensors. This is such that

$$SG_{new} = SG_{raw}C \tag{5.2}$$

where SG_{new} is the scaled strain gauge value, SG_{raw} is the phase averaged strain gauge data, and C is a factor to match the mean of the strain gauge data to the measurement from thrust and torque transducer. The factor (C) is the ratio of M^*_{FW} or M^*_{EW}, dependant on the direction, and the mean strain gauge value over all three turbine blades. This process ensures the data set is internally consistent, using the average load measured from the thrust and torque transducer to adjust the blade sensors.

Blade Averaging

Finally, the root bending moment is averaged over the phase-offset blade loads to arrive at a blade and azimuthally averaged root bending moment following

$$M_j = \sum_{i=1}^{N_b} \frac{SG_{new_i,j}(\theta_i)}{N_b} \tag{5.3}$$

where M_j is the blade and azimuthally averaged root bending moment, the subscript j denotes the edge-wise and flap-wise directions, SG_{new_i} is the azimuthally averaged strain gauge data for blade i which has been phase corrected for the blade offset ($\theta = 0°$ for blade 1, $\theta = 120°$ for blade 2, and $\theta = 240°$ for blade 3). An additional quantity M_j^- was defined to compare directly against M^*_{FW} and M^*_{EW} by using $\theta = 0$ for all blades.

Self Weight Correction

A correction for the blade self-weight and buoyancy was applied to the edge-

wise root bending moments

$$M'_{EW} = M_{EW} - gr_B(m_B - V_B\rho)\sin\theta \tag{5.4}$$

where M'_{EW} is the edge-wise root bending moment corrected for blade self-weight and buoyancy, g is the acceleration due to gravity, r_B is the distance to the centre of mass of the blade, m_B is the mass of the blade, and V_B is the volume of the blade. The blade's geometric properties (r_B and V_B) were derived from a SolidWorks model developed by McNaughton et al. (2019).

Non-dimensionalised Parameters

The root bending moment was non-dimensionalised following

$$C_{FW} = \frac{N_b M_{FW}}{\frac{1}{2}\rho u_\infty^2 A_t R}, \quad C_{EW} = \frac{N_b M'_{EW}}{\frac{1}{2}\rho u_\infty^2 A_t R}. \tag{5.5}$$

5.3 Performance without end constraints

This section presents the experimental results of McNaughton et al. (2021) to provide context and as a reference case from which the effect of an end-wall constraint can be assessed. All results presented in this section were obtained with a constant tow speed of 0.8 m/s.

5.3.1 Performance parameters

Fence averaged C_p and C_t from the experimental work of McNaughton et al. (2021) are presented in Figure 5.3. These results confirm the observation of Nishino and Willden (2013) that closer turbine spacings produce greater power output. How-

ever, as discussed when examining numerical models for turbine spacing in Section 4.3, this performance improvement is not shared uniformly along the turbine fence due to end-losses. Instead, the increase in fence power is primarily driven by an improvement of inboard turbine performance; this is confirmed by ΦC_p and ΦC_t with bias being shifted towards the inboard turbine with decreased spacing.

At larger turbine spacings ($s = 0.72D$ and $s = D$), the inboard turbine generates less power than the outboard turbine; this result is surprising given the higher local blockage of the inboard turbine. A reduction of inboard turbine power may be due to the assumption of the tank wall as a symmetry plane. In the experiment, fluid and the tank wall do not move at the same speed due to the bow wave and wake of the turbine fence inducing a relative motion between them, forming a boundary layer and altering the inflow condition. This is considered in further detail in Section 5.5.

5.3.2 Root bending moments

Phase averaged root bending moment data is presented in Figure 5.4 for $s = D$, $s = 0.72D$ and $s = 0.25D$. The phase averaged root bending moment was calculated following the methodology outlined in Section 5.2.3. The triplicate data from the blade-mounted strain gauges provides a smooth phase-averaged signal across the entire rotation.

Figure 5.4 demonstrates the effect of both local blockage and end-losses on the root bending moment. The inboard turbine has a steady increase in C_{EW} with decreased spacing at all azimuthal locations; this leads to an improvement in C_p. The increased performance of this turbine is due to various factors associated

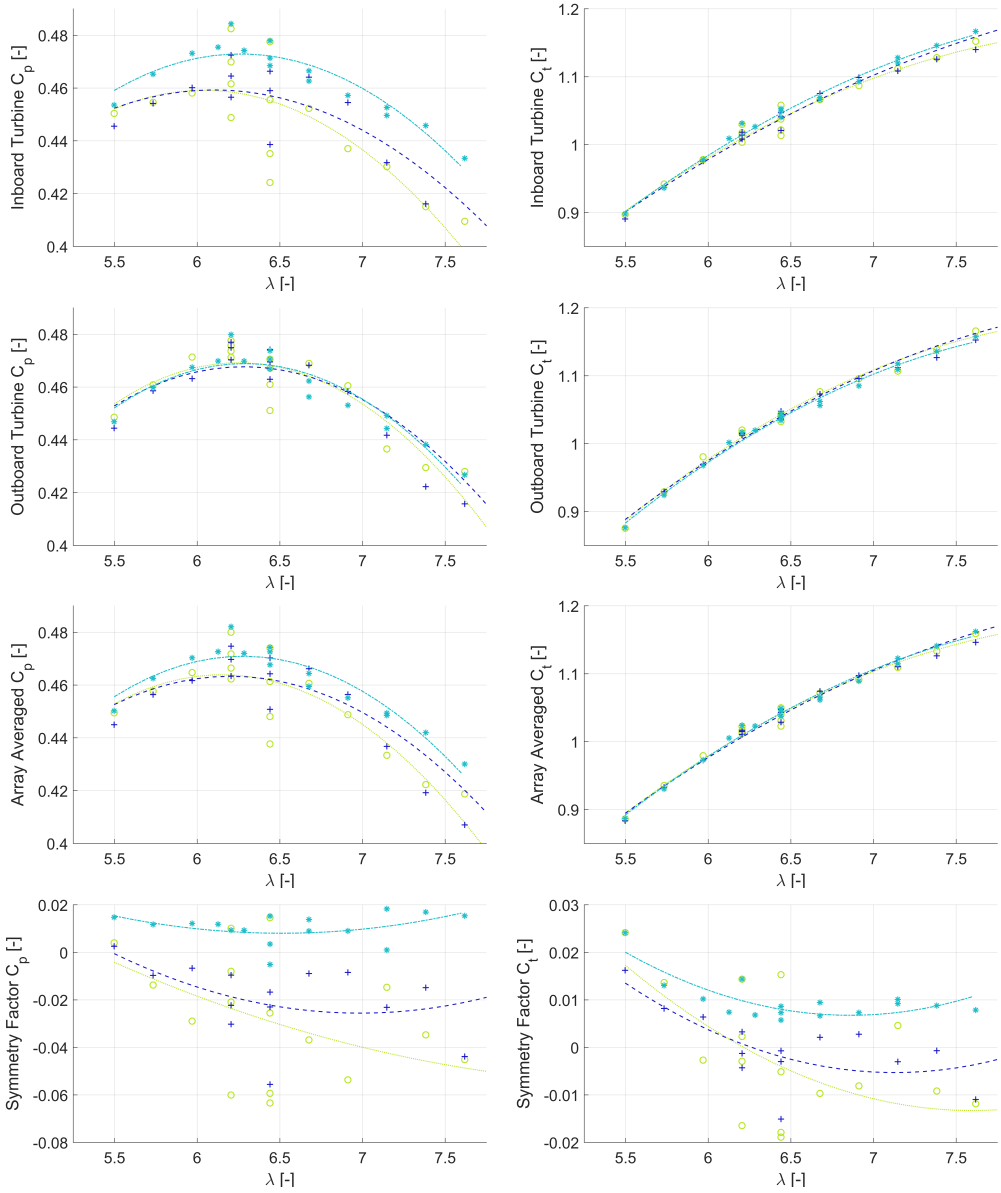

Figure 5.3: C_p and C_t performance curves from the experimental testing of McNaughton et al. (2021) for a tidal turbine fence at varied inter-turbine spacings of $s = D$ (green) $s = 0.72D$ (dark blue) and $s = 0.25D$ (blue). Results for the inboard turbine are plotted in the top row, outboard in the top-middle, fence averaged on the bottom-middle and symmetry factor in the bottom row. The wait time between tests is between 10 and 20 minutes. A second order polynomial has been fit to the data to improve readability.

with local blockage (improved flow speed, wake constraint, inflow angle) and is examined in further detail by McNaughton et al. (2021). Contrasting this result is the outboard turbine C_{EW} signal, where a noticeable improvement is observed as it passes the inboard turbine ($\theta = 270°$). At the outboard location ($\theta = 90°$), the root bending moment appears to be unaffected by the change in spacing. Outer turbine C_{FW} is also impacted by the varied spacing and has a minimum just prior to passing the exposed edge of the fence ($\theta = 60°$). This minimum decreases with inter-turbine spacing demonstrating a growing end-loss. These observations are consistent with the results from Section 4.3 and provide further justification for why an end-wall may be a practical solution for improving turbine performance, especially at close turbine spacing.

5.4 Performance of turbines with end-wall constraint

The performance of the turbine fence with an end-wall is examined in this section. Unlike the results presented in Section 5.3, the towing speed for these tests was 1 m/s (instead of 0.8 m/s). As discussed in Section 5.2.1, higher tow speeds were used to ensure Reynolds independence of the results. Consequentially there is a slight difference between the without end-wall results presented in this section at $s = 0.25D$ and those from Section 5.3.

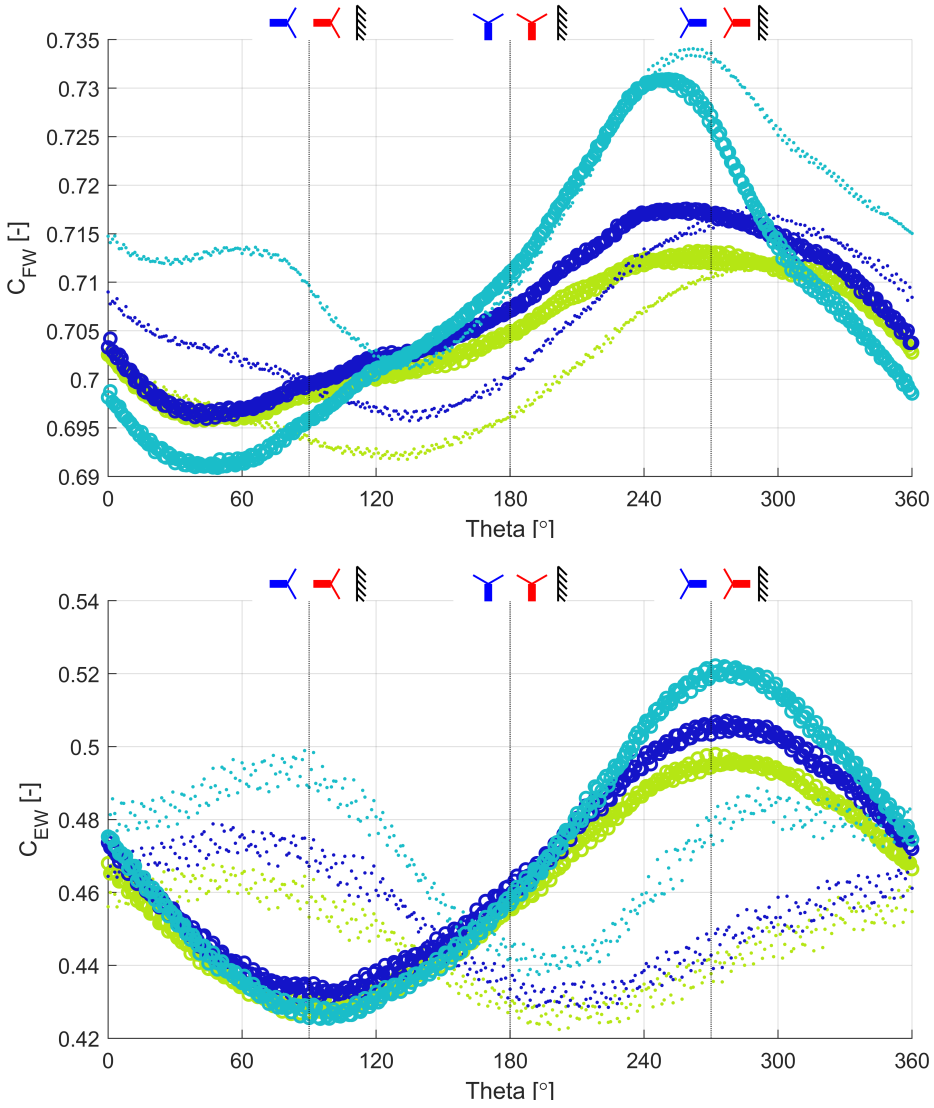

Figure 5.4: Phase averaged flap-wise (top) and edge-wise (bottom) root bending moments at varied inter-turbine spacing of $s = D$ (green) $s = 0.72D$ (dark blue) and $s = 0.25D$ (blue) for a fixed λ of 6.44. The inboard and outboard turbine data is represented by the dots and circles respectively. The wait time between tests is between 10 and 20 minutes and duplicate data has been averaged; blade self weight and buoyancy has been controlled for in the edge-wise root bending moment signal. The three illustrations at the top of each plot show the location of the blade (in bold) in the domain, with blue and red representing the outboard and inboard turbines in these illustrations. Data supplied by McNaughton et al. (2021)

Table 5.1: A comparison of turbine performance metrics C_p and C_t at λ^* for a four turbine fence at a spacing of s/D=0.25 from a RANS-BE model and an experimental study.

		Without end-wall			With end-wall		
		RANS-BE	Exper	Error	RANS-BE	Exper	Error
	$\lambda*$	6.52	6.44	1.2%	6.37	6.44	-1.1%
Inner Turbine	C_p	0.569	0.484	17.6%	0.582	0.480	21.3%
	C_t	1.119	1.058	5.8%	1.107	1.053	5.1%
Outer Turbine	C_p	0.553	0.479	15.6%	0.584	0.486	20.2%
	C_t	1.108	1.044	6.1%	1.108	1.048	5.7%

5.4.1 Performance parameters

Table 5.1 presents a comparison between performance metrics from the RANS-BE model and experimental study, highlighting that differences of up to 21.3% in C_p and 6.1% in C_t were observed. The causes for these disparities are primarily credited to the limitations of the RANS-BE model and experimental error (discussed further in Section 5.5). However, scaled values of C_p and C_t allow comparison between the data sets.

Figure 5.5 confirms the numerical model's observation that the outer turbine's performance (C_p and C_t) is improved by the end-wall, albeit to a smaller degree than predicted in the numerical model. The experimental results show a 1.5% increase in outer turbine power at λ^*, and a 0.8% decrease for the inner turbine, to achieve an overall improvement of 0.5% when the end-wall is in place. This is achieved at approximately the same λ and fence thrust as the case without the end-wall. At λ^*, the end-wall caused the outer turbine thrust to increase and the inner turbine thrust to decrease, bringing both values closer to the mean fence thrust and reducing ΦC_t.

Inner turbine C_p was observed to decrease when the end-wall was installed,

this goes against the findings of the numerical model which showed an increase in power alongside the outer turbine. This finding was consistent over the range of λ tested.

The experimental results are further understood by considering how the turbine performance is improved. Typically, this is through increasing the mass flux through the turbine or achieving a better angle of attack along the blades; the opposite is also true and worse performance comes from the reduced mass flux and worse angles of attack. For a reduced mass flux a drop in C_t and C_p is expected ($C_p \propto u^3$ and $C_t \propto u^2$). Given this relation, the 0.8% drop in power for the inboard turbine is expected to be accompanied by a 0.5% drop in thrust; this is close to the measured drop in thrust, which is just under 0.5%. In contrast, the 1.5% increase in power for the outboard turbine is expected to have a 1.0% increase in thrust; instead, only a 0.4% increase in thrust was observed. This result suggests that the improvement of the inboard turbine's performance may not be solely connected to an improvement mass flux and could also be a function of improved angle of attack on the blade. This is explored further in Section 5.4.2 with the analysis of root bending moment data.

In contrast to the above, the RANS-BE results suggested that the mass flux through both turbines increased with the end-wall installation. This resulted in a higher thrust on the outboard turbine and over-predicted the change in thrust with the end-wall, causing greater confinement (and therefore power generating capacity) of the inboard turbine and an over prediction of inboard turbine power. In practice, the use of RANS-BE models with yawed flows passing around the ends of turbine fences is not strictly valid as there is a shear profile in the flow; this is discussed in further detail in Section 5.5. Given the lack of Re independence

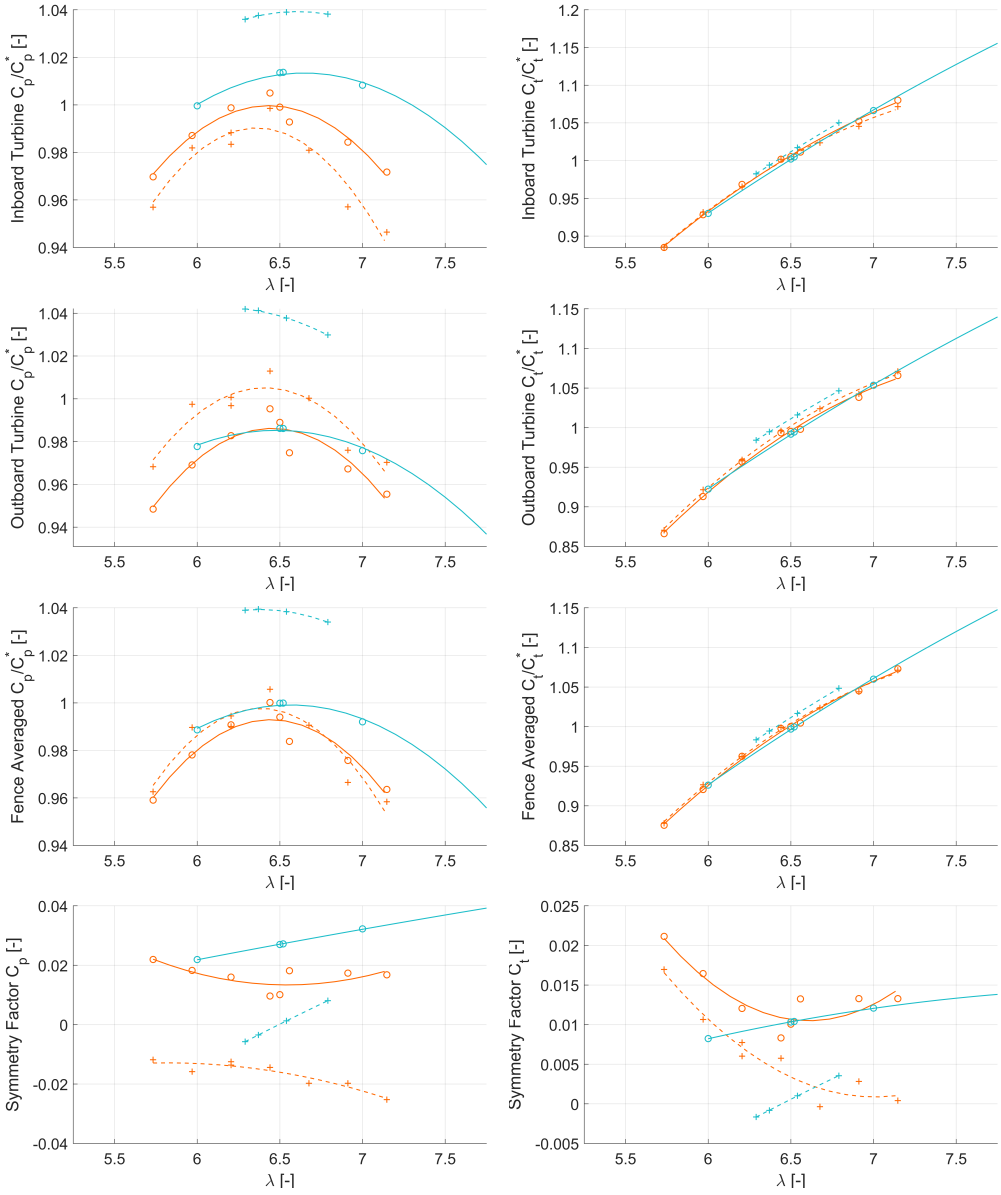

Figure 5.5: C_p (left) and C_t (right) performance curves comparing between experimental testing (orange) and the RANS-BE model (blue) for a tidal turbine with (dashed line and cross markers) and without (McNaughton et al., 2021) (solid line with circle markers) an end-wall. The results for the inner turbine are presented on the top row, the outer turbine in the second row and the fence-averaged in the third row. The symmetry factors for C_p and C_t are plotted on the bottom row. C_p curves have been scaled by the without end-wall fence averaged maximum power (C_p^*) and the C_t curves have been scaled by the fence averaged thrust at C_p^* (C_t^*). A second order polynomial has been fit to the data to improve readability.

observed for the 0.8 m/s towing experiments (McNaughton et al., 2021), there is more confidence in the results from the RANS-BE model at higher λ. This is due to the higher λ contributing to a higher relative velocity and Re.

Duplicate towing tank test results, shown in Figure 5.5, demonstrated some variability in the experiment, around the design point. While small, this impacted the accuracy to which the optimal operating point is defined. It was hypothesised that this difference was a function of the build up of turbulence in the towing tank which was observed to not fully decay between tests.

5.4.2 Root bending moments

Phase-averaged blade root bending moments in the flap-wise (C_{FW}) and edge-wise (C_{EW}) directions at λ^* are compared between the experimental results and the RANS-BE model in Figure 5.6. Blade self weight effects in the edge-wise direction have been controlled for in the experimental data set and a 5° wide moving average has been applied to the experimental results to improve the clarity in this figure. Figure 5.6 demonstrates the end-wall's influence on the blades of the outer turbine is localised around the 90° position, where they are closest to the end-wall.

The end-wall introduces a second local maximum into the loading signal of the outer turbine where the minimum loading was previously experienced. This reduces the loading amplitude and brings the azimuthal variation closer to that experienced by the inner turbine. Comparing the outer turbine with and without end-wall C_{EW} curves, the edge-wise root bending moment is increased in the 180° portion (0° to 180°) closest to the end-wall, and the remaining portion is relatively unchanged. The total improvement results in a higher overall turbine torque and

thus power.

More subtle changes are observed for the inner turbine, with a marginal reduction in C_{FW} just after the blade passes the outer turbine at 135° and negligible changes in C_{EW}.

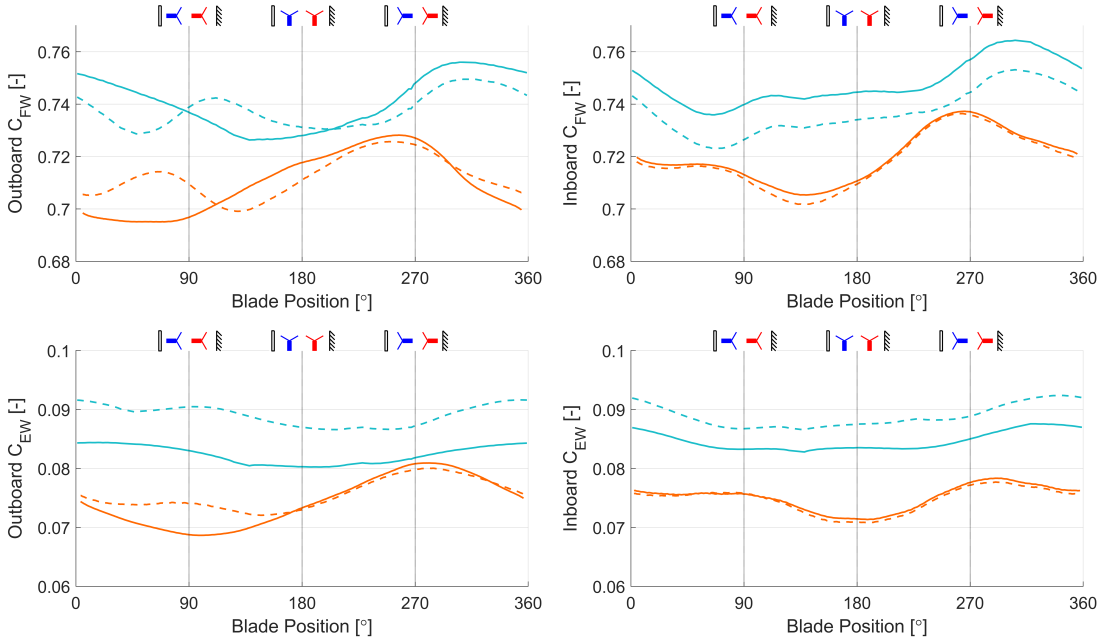

Figure 5.6: Phase-averaged flap-wise (top) and edge-wise (bottom) root bending moments comparison of RANS-BE (blue) and experimental (orange) results at λ^* for outer (left) and inner (right) turbines. Solid lines represent the without end-wall case and dashed lines the with end-wall case. The illustrations at the top of each plot show the location of the blade (in bold) in the domain, with blue and red representing the outer and inner turbines.

Both the numerical and experimental results show a peak in C_{FW} for the inner and outer turbines. The maximum flap-wise root bending moment was recorded at 260° in the experiment, whereas the simulations predicted this to be at 300°. In both cases, the maximum coincides with passing an adjacent turbine. A secondary local maximum in the C_{FW} signal was observed for the inner turbine as it passed the outer turbine in both data sets. Like the larger peak, a phase offset of $\approx 40°$

in blade position was observed between the data sets. The phase offset may be due to the RANS-BE model not explicitly modelling the rotation of the blades, and consequently phenomenon such as blade advancing and retreating in yawed flow are not resolved.

Overall the RANS-BE model overestimated the loading on the turbines and the loading change due to the end-wall. This is quantified in Table 5.2, which shows the difference in the average root bending moments between the RANS-BE model and the experimental data. The RANS-BE model's error was between 3.9% and 4.4% in the flap-wise direction and 10.8% and 18.9% in the edge-wise direction. Unlike the numerical results the impact from the end-wall is limited to the outer turbine, with no clear offset of the inner turbine C_{EW} or C_{FW}. A factor contributing to this is the different λ^* the RANS-BE model predicted when the end-wall was introduced. Optimal fence λ^* did not change in the experiments when the end-wall was introduced ($\lambda^* = 6.44$) whereas in the numerical model λ^* dropped from 6.59 to 6.37 with the end-wall. Consequently, the turbines are operating at different speeds between the experimental and numerical cases. Figure 5.7 plots the azimuthal variation in root bending moment for rotors operating at a constant λ=6.44. When the turbines are operated at the same λ in both the numerical and experimental models, closer agreement in blade loading is observed. Despite the offset to the mean root bending moment, the RANS-BE model captures the approximate amplitude of the variations in root bending moment through a rotation, albeit with differences in phasing (especially for the outer turbine).

The introduction of an end-wall appears to have a different response in the RANS-BE model and the experiment. In the RANS-BE model, a noticeable positive offset in edge-wise root bending moment and a negative offset in the flap-wise

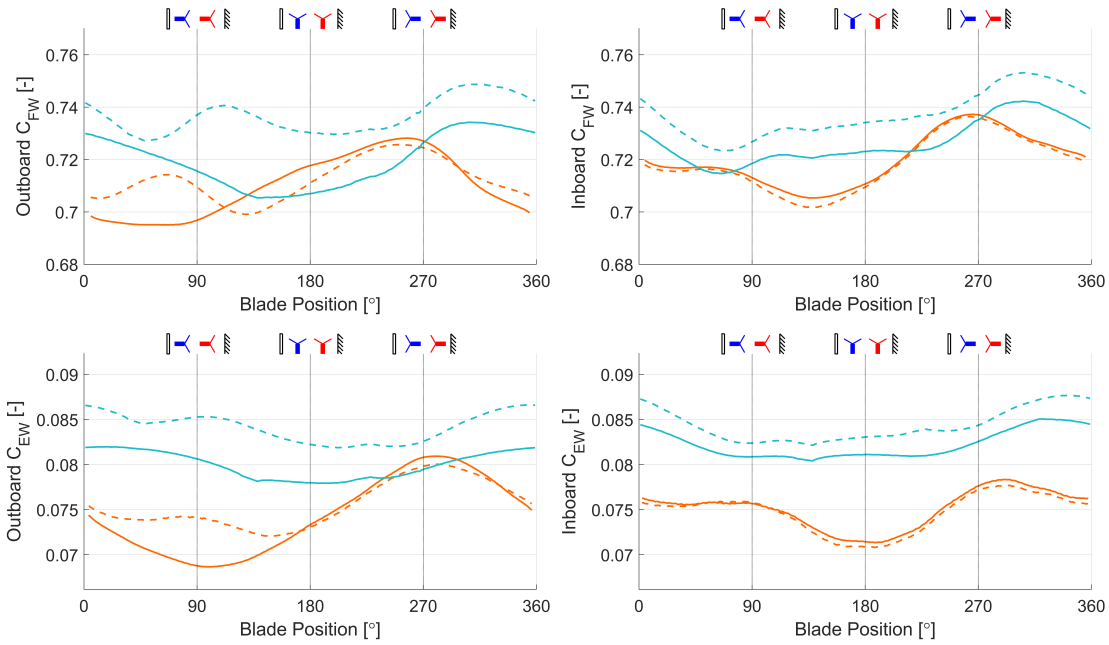

Figure 5.7: Phase-averaged flap-wise (top) and edge-wise (bottom) root bending moments comparison of RANS-BE (blue) and experimental (orange) results **at the same λ=6.44** for outer (left) and inner (right) turbines. Solid lines represent the without end-wall case and dashed lines the with end-wall case. The illustrations at the top of each plot show the location of the blade (in bold) in the domain, with blue and red representing the outer and inner turbines.

root bending moment was observed (due to lower λ) alongside a secondary peak in the outboard turbine loading. While there is little evidence of an offset in the experimental data, an additional loading peak is present. Like the loading peaks without the end-wall, this was observed to be out of phase by 40° between the data sets.

5.4.3 End-wall loading

Due to a strain gauge's failure during the end-wall installation, data were available from only one strain gauge measuring bending moment in the cross-stream

Table 5.2: A comparison of mean root bending moments over a rotation for a fence of four turbines operating at λ^* and $s = 0.25D$ with and without a end-wall.

		Without End-wall			With End-wall		
		RANS-BE	Exper	Error	RANS-BE	Exper	Error
	λ^*	6.52	6.44	1.2%	6.37	6.44	-1.1%
Inner Turbine	$\overline{C_{FW}}$	0.748	0.720	3.9%	0.737	0.718	2.6%
	$\overline{C_{EW}}$	0.085	0.075	12.6%	0.089	0.075	18.9%
Outer Turbine	$\overline{C_{FW}}$	0.741	0.710	4.4%	0.738	0.712	3.6%
	$\overline{C_{EW}}$	0.082	0.074	10.8%	0.089	0.076	17.9%

direction at the connection between the end-wall and the supporting beam. A linear elastic frame model was developed in SPACE GASS 12.85 to determine the relationship between the measured bending moment and cross-stream loading. A factor to convert bending moment to a cross-stream force was determined by applying a unit load in the cross-stream direction at the centre of pressure (determined from the RANS-BE model) and scaling the load to match the measured bending moment.

The cross-stream loading on the end-wall, presented in Figure 5.8, corresponds to the confinement force on the bypass flow. Cross-stream loading was observed to increase approximately linearly with rotor λ, as higher turbine thrust tends to produce greater acceleration of the bypass flow. The loading on the wall has been non-dimensionalised using the same representative area as the turbines (A_t) to allow direct comparison with turbine C_t. At λ^*, the cross-stream force on the end-wall is close to half the turbine thrust.

Good agreement between the experimental results and the RANS-BE model is observed for the end-wall cross-stream loading. The loading range shown in the experimental data highlights the variability in the cross-stream force, which can be up to 15% of the turbine thrust. This fluctuation is likely a result of

transient effects, which include blade passing and vortex shedding (not captured in the RANS-BE model), experimental uncertainty of the turbulence conditions in the tank and the fixity of the end-wall with the towing carriage.

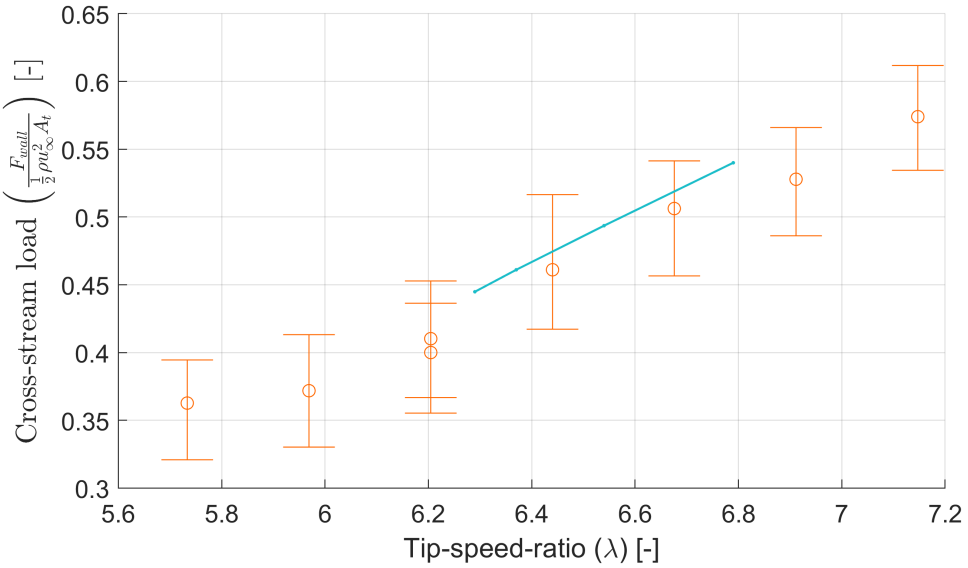

Figure 5.8: Cross-stream loading on the end-wall as a function of turbine tip-speed-ratio (λ) from the experimental (orange) and numerical (blue) studies. The 5th and 95th percentiles of the time series of the experimental data are indicated, and the marker is the median load. Results are non-dimensionalised using the turbine swept area.

5.4.4 Frequency analysis

Fast Fourier Transforms (FFTs) of the blade root bending moment, integrated power and thrust coefficients and end-wall cross-stream force are presented in Figure 5.9. The blade root bending moments all exhibit a peak at the once per-rotation frequency (f_0) with distinctive peaks at $2f_0$, $3f_0$, $4f_0$, $5f_0$ and $6f_0$ in some cases. As observed by Payne et al. (2018) the once-per-revolution loading spikes can be credited to a tower passing effect where the blade passing the support

tower causes a drop in thrust leading to a once-per-rotation frequency spike in blade loads. The tower was located a distance of $0.33D$ behind the turbine plane and its position corresponded to the 0° blade location.

Examining Figure 5.6, an increase in flap-wise bending just before the rotors pass each other (90° and 270° for the inboard turbine and 270° for the outboard turbine) is observed. Whilst there are two peaks for the inboard turbine, the flap-wise root bending moment is maximum when the blade is at 250° (just before it passes the tank sidewall); this is the same location for the outboard turbine. When the end-wall is introduced, a second peak in the outboard turbine loading immediately before passing the end-wall is present at 70°; this peak is offset 180° from the without end-wall maximum load and is slightly smaller in magnitude. As a result, an increase in the energy at $2f_0$ and its harmonic ($4f_0$) is observed when the end-wall is installed with energy at f_0 remaining relatively unchanged.

For the edge-wise root bending moment without an end-wall, a single loading peak is observed at 270° for the outboard turbine and two peaks at 90° and 270° for the inboard turbine. When the wall is installed, a second peak is introduced around 90° in the outboard turbine loading. This results in an increase in the energy at f_0 and the harmonics (up to the $6f_0$). For the inner turbine, little change is observed when the wall is in place, corresponding to no distinct difference in the flap-wise and edge-wise energy spectrum.

Harmonics exist at $2f_0$ and $3f_0$ in the power spectrum for the thrust and power coefficients. The $3f_0$ peak is likely associated with blade passing effects. The even harmonics may be explained through the tank's aspect ratio (5 m depth and 10 m width) and potential yaw misalignment of the rotors or end-wall, which would result in $2f_0$ spectral content.

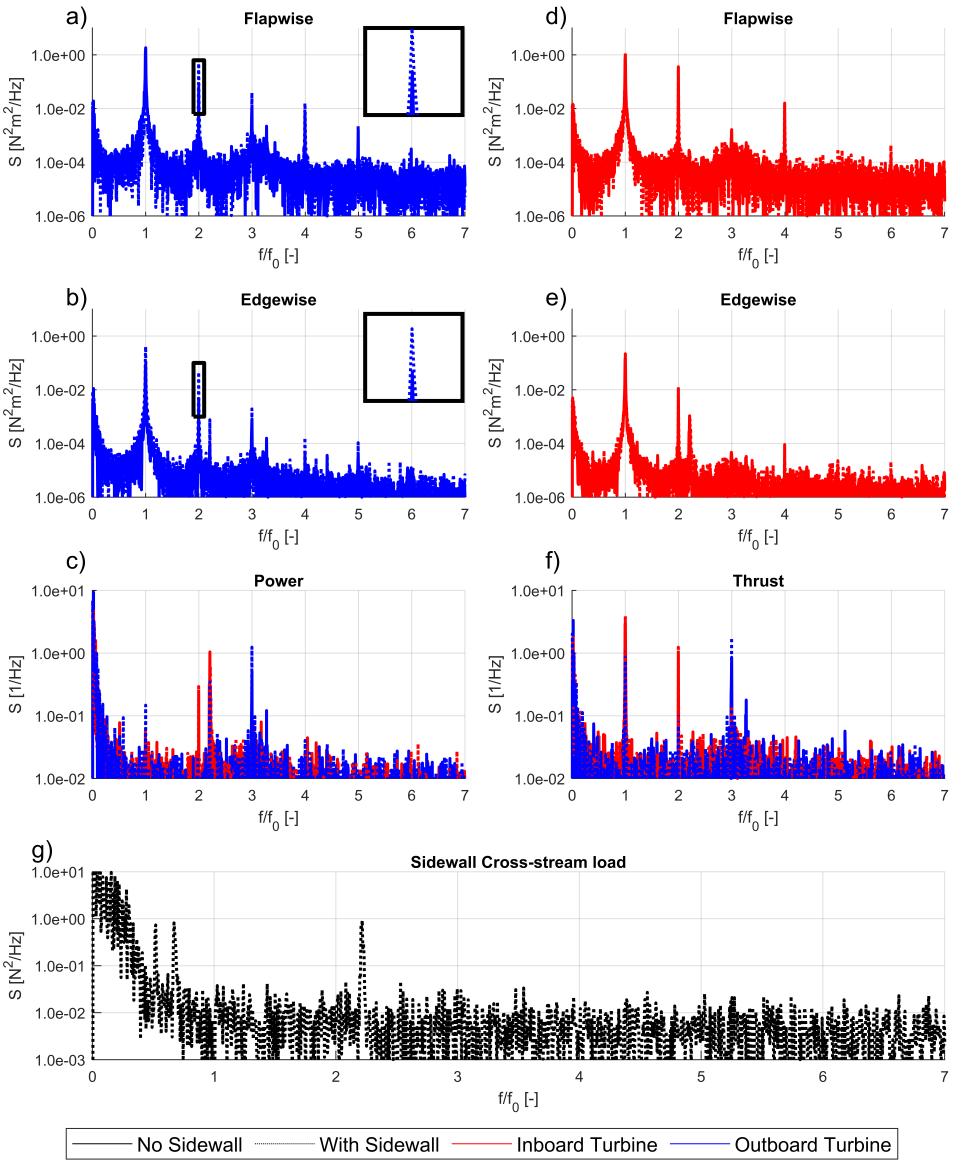

Figure 5.9: Typical power spectrum of turbine loading at λ=5.74. Flap-wise root bending moment is plotted on top with the edge-wise direction plotted below. The third row plots the spectrum's for the turbine power coefficient on the left and thrust coefficient on the right. The bottom level plots the power spectrum for the cross-stream loading on the end-wall. Red is the inboard turbine and blue is the outboard turbines, solid lines represent the case without the end-wall and dotted lines the case with the end-wall.

Finally, three significant peaks were observed in the cross-stream loading acting on the end-wall; the first two spikes corresponded to frequencies less than f_0 at $0.5f_0$ and $0.67f_0$, these vary slightly between the experiments as the λ was changed. There is no clear signal in the root bending moment or the integrated quantities at these frequencies, suggesting it may result from an external low frequency source such as vortex shedding from the end-wall. The final peak occurs at $2.2f_0$; however, its value was observed to vary linearly with λ and was present with and without an end-wall suggesting it may be the tow carriage response to the turbine operation.

5.5 Numerical and experimental limitations

The limitations of the blade element method are well documented (Vermeer et al., 2003; Snel, 2003; Malki et al., 2013) and are essential for the computationally efficient simulation of turbine rotors. Within the RANS-BE model used in the study the assumptions of azimuthal flow symmetry through the rotor and no span-wise flow were not strictly valid, especially as the turbines were positioned closely together. This is due to the closely spaced turbines introducing a shear profile to the incoming flow. Models such as the actuator line method (Section 3.1.3) and unsteady blade resolved RANS 3.1.2) are more capable of resolving these conditions, however come at a far higher computational cost. Regardless of this, the RANS-BE model was able to demonstrate the leading order physics at play and qualitatively match the experimental observations.

Furthermore, the RANS-BE method is a steady approximation to an unsteady process. As a result, the blade element method imposes resistance over the entire swept area throughout the simulation. Consequently, localised flow effects are

smoothed over the rotor swept area as the model cannot resolve the pressure relief on blades as flow accelerates between them. The effect of this is highlighted in Figure 5.7, which shows that the change in flap-wise root bending moment is localised to the end-wall side in the experimental data, whereas in the RANS-BE model an offset over the entire azimuth is present in addition to the localised change. This is examined further in Figure 5.10, which plots the difference in pressure drop across the outboard turbine due to the end-wall. Whilst there is a noticeable increase in pressure drop for the outboard section of the rotor as it passes the end-wall, there is a significant increase over the remainder of the swept area; this is the smoothed response of the RANS-BE model, causing the offset in the root bending moment.

Despite the RANS-BE model's shortcomings in evaluating the fence's performance, it accurately predicts the loading on the end-wall and approximates the turbine thrust to within 5% (when operating at the same λ). This is in line with the work of Olczak et al. (2016) who observed a 3-12% over-prediction of the RANS-BE model to experimental results.

In the experiment, the presence of a boundary layer on the tank wall may have caused a change in loading on the inner turbine. The symmetry assumption for the tank wall in the experiment is only completely valid when the fluid and boundary move at the same speed. However, this is not the case; while the wall and the water are still during the experimentation, the force exerted by the turbine on the flow causes relative motion between the fluid and wall, inducing a boundary layer that changes the velocity distribution across the rotor. The impact of this assumption was investigated numerically by using a smooth moving wall boundary condition in place of the symmetry plane in the RANS-BE model. Additional mesh

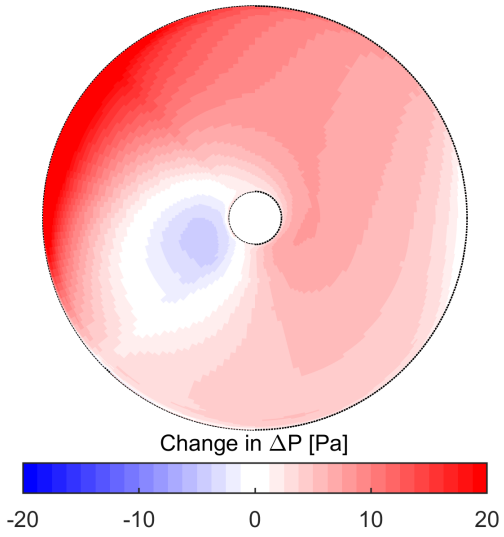

Figure 5.10: Change in pressure drop over the outboard turbine swept area from the RANS-BE model after the installation of an end-wall. The difference is calculated as the with end-wall case minus the without end-wall case for λ=6.44.

refinement was required between the side of the domain and rotors to achieve a y^+ <100 over the tank wall. Figure 5.11 plots the evolution of the velocity profile at stream-wise positions relative to the turbine plane. A slight decrease in velocity at the inboard section of the turbine is observed when the moving wall boundary is used; however, the greatest impact on velocity appears to be in the wake. Figure 5.12 compares the first three powers of the velocity normal to the turbine (the first power corresponds to flow rate, the second to momentum flux and the third to energy flux) and presents the area-weighted integral over the rotor plane. This boundary condition primarily affects the inboard section of the rotor resulting in a 1.8% drop in flow rate, 2.9% drop in momentum flux and a 3.5% drop in energy flux. The analysis goes part of the way to explaining why the power of the inboard turbine did not increase as predicted by the RANS-BE model when the end-wall

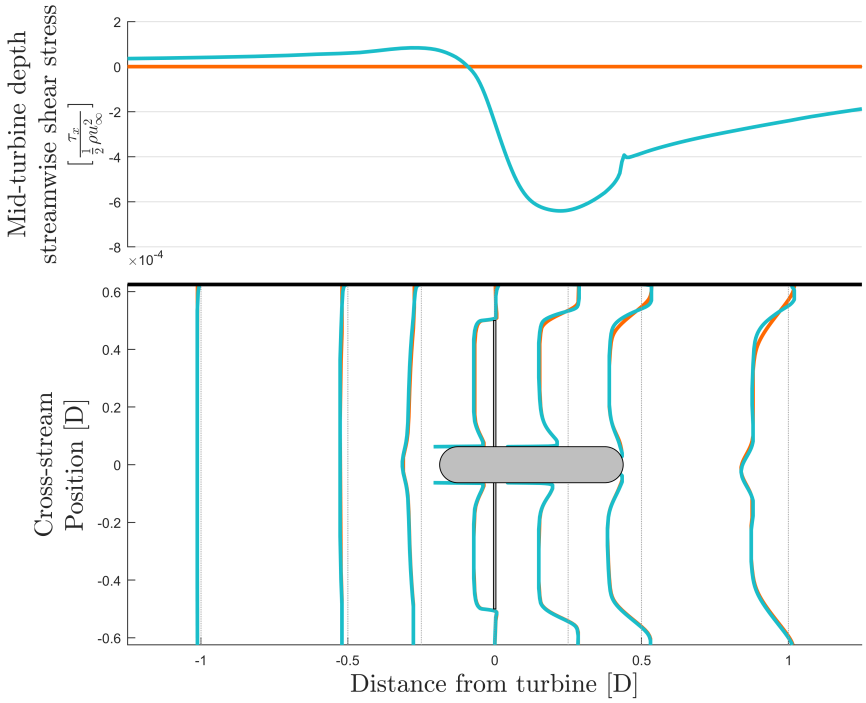

Figure 5.11: Variation in tank sidewall shear stress at nacelle depth in the streamwise direction (top) and profiles of velocity magnitude at nacelle depth for the inner turbine adjacent to the symmetry plane (orange) and wall (blue) boundaries. The boundary is located at the cross-stream position, $0.625D$, and the dotted grey lines represent the free-stream flow condition (0.8m/s). Flow is from left to right.

was installed.

5.6 Conclusions

Towing tank tests were performed to establish an end-wall's potential to improve performance over a short turbine fence and re-distribute thrust and power along the fence. While only a marginal improvement in overall fence performance was observed, outer turbine power increased by 1.5%, and the end-wall was observed to balance the thrust loading between the rotors and reduce the difference in the

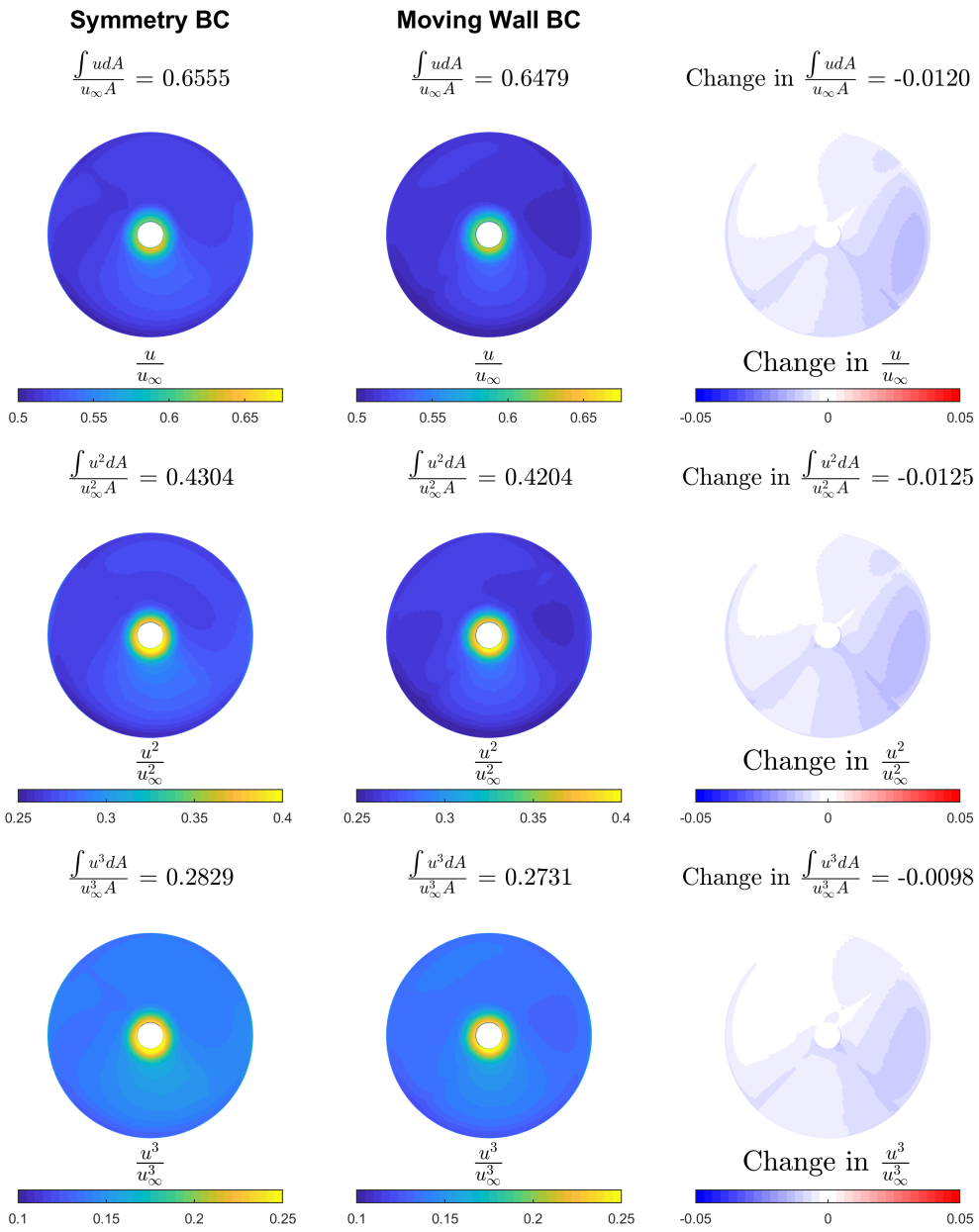

Figure 5.12: Powers of velocity normal to the turbine for the inboard turbine with a symmetry plane boundary condition (left) and a moving wall boundary condition (middle) and the difference between them (right). The location of the boundary is to the right of the turbine. The difference is calculated as the results using the moving wall boundary condition minus the symmetry plane boundary condition. The area weighted average is presented at the top of each plot.

loading cycle magnitude between the inner and outer turbine.

The experimental results were compared with the numerical results from Chapter 4. This comparison showed the improvement from installing an end-wall was significantly over-predicted by the RANS-BE model. The discrepancy was determined to be a factor of the model exaggerating the flow's response from the end-wall, limitations of the RANS-BE model, and the formation of a small boundary layer in the towing tank experiment which was not resolved in the model. The study also highlighted some of the difficulties in accurately modelling closely spaced tidal turbines, especially in anisotropic blockage conditions. Despite the RANS-BE model's poor performance in predicting power extraction, the average root bending moment in the flap-wise direction was conservatively estimated within 5% of the experimentally determined value. The model was also able to accurately predict the mean loading on the end-wall in the cross-stream direction.

This study highlights the potential for developers to enhance turbine performance by using elements of floating tidal platforms required to provide buoyancy to also align the flow approaching the turbines. Utilising end-walls may also be helpful as they allow for a reduced optimal tip-speed-ratio, reducing blade loading. Furthermore, the root bending moments between the inner and outer turbines were closer for both the averaged and cyclic loading components, equalising the accumulation of blade fatigue across the rotors in the fence. Integration of the end-wall into the turbine blade design methodology may enable further performance gains to be made by optimising the blade geometry for the flow conditions experienced by the turbines.

Chapter 6

8m diameter rotor design

This chapter presents a design methodology and analysis for a turbine for which the flow to the blade is fully turbulent. This rotor's development allows for the computationally efficient simulation of tidal rotors as fully turbulent conditions permit the $k-\omega$ SST turbulence model with enhanced wall treatment to be used. Smaller turbines, such as the one used in Chapter 4, require laminar-turbulent transitional turbulence closure models to determine the boundary-layer fluid mechanics. This is impractical when analysing turbine fences due to the computational requirements of such models. The 8 m diameter turbines developed in this Chapter allows for detailed blade resolved simulations of turbine fences (Chapter 7), improving the understanding of fence thrust and power distribution and mitigation options to reduce turbine fence end-losses. The tidal turbine was designed to operate in Strangford Lough, Northern Ireland.

6.1 Design process

A turbine was designed using the process presented in Figure 6.1. There were four phases of the design methodology, the first was to define the design parameters, and the following three were numerical simulations of the rotor with increasing levels of refinement and model complexity. The subsequent sections highlight the details of each design phase.

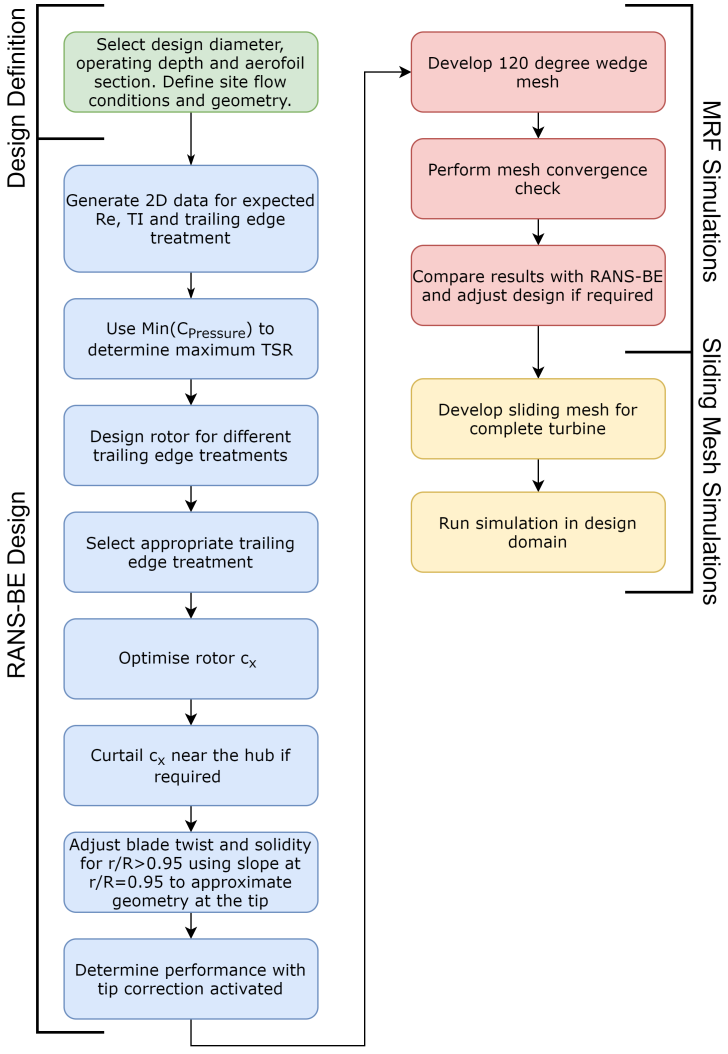

Figure 6.1: Turbine design methodology.

Table 6.1: Summary of hydrodynamic design conditions

Parameter	**Value**	**Notes**
Design velocity	2.5 m/s	Based on the study of Kregting and Elsäßer (2014) this value is reached on 55% of tidal cycles
Freestream turbulence intensity	6%	This is the average measurements from MacEnri et al. (2013) for the design velocity
Width	550 m	Survey data from Annika Clements and Service (2015)
Depth	30 m	Survey data from Annika Clements and Service (2015)

6.2 Design definition

Flow conditions used for the rotor design were derived based on the hydrodynamic conditions at Strangford Lough in Northern Ireland. This site provides a sheltered environment from wave action owing to the narrow channel leading into the Lough (Figure 6.2) and has previously been the test location of the SeaGen turbine (MacEnri et al., 2011). The channel's width is approximately 550 m at the test location and has a depth of 30 m according to a multibeam bathymetric survey of the Lough from 2014 (Annika Clements and Service, 2015). The area surrounding the site has a relatively flat terrain (between 0-1.9°).

Tidal currents through Strangford Lough's narrows can reach up to 3.5 m/s during spring tides with more typical peak velocities during flood and ebb tides of 2.5 m/s (Kregting and Elsäßer, 2014). A survey by MacEnri et al. (2013) indicated that the turbulence intensity in the channel ranges between 3% and 9%, with the values being inversely proportional to flow speed. The hydrodynamic conditions selected for the rotor design are summarised in Table 6.1.

Table 6.2 lists rotor design parameters. These parameters were selected based

Figure 6.2: Strangford Lough showing the SeaGen testing location within the Narrows.

on an overview of existing turbine technology and applying scaled values to an 8 m diameter turbine. The nacelle diameter was selected based on the Atlantis AR1500 (Simec Atlantas, 2016), Hammerfest Strøm (Andritz Hydro, 2016), and the experimental rotor of Cao et al. (2019) which all had a nacelle to rotor diameter ratio between 10% to 15%. A design range for λ was selected based on the AR1500 and the Hammerfest Strøm turbines, designed for λ between 4.15 and 5.75. This range is lower than in the smaller rotor of Cao et al. (2019) which was designed for $\lambda = 7$; this is partly due to the larger diameter rotors needing to limit tip speed to avoid cavitation inception. Finally, an operating depth placing the nacelle at 1/3 depth was selected based on comparison with the Orbital Marine O2 device (Orbital Marine Power, 2019). Positioning the turbine at this depth ensures it is located away from the seafloor in the more energetic flow region of the water column and provides additional cavitation protection due to the static pressure head. Additionally, this depth provides some tip clearance if vessels are to pass

Table 6.2: Summary of turbine design conditions

Parameter	**Value**
Diameter (D)	8 m
Inter-turbine spacing (s)	2 m
Operating depth of nacelle (Z_{hub})	10 m
Number of blades	3
Nacelle diameter	1 m
Aerofoil	NACA-63-415 with modified trailing edge
λ	4-6
Ω	2.5-3.75 rad/s
Re_{chord} at 80% span	2×10^6 - 3.2×10^6
B_g	1.2%
B_l	16.8%

over the fence.

6.3 RANS-BE actuator disk design

The RANS-BE actuator disk (AD) design tool developed by McIntosh et al. (2011) was used to determine the twist (β) and solidity (σ) distribution along the blade length. This tool applied the RANS-BE formulation outlined in Section 3.1.2 with an additional iterative loop that adjusted the blade twist and solidity to achieve a target α and target local thrust coefficient (c_x). The design tool did not consider discrete blade effects, which prevented the use of a tip correction model. Consequently, the initial rotor designs overestimated the performance; however, once the initial design was confirmed, addition of simulations were run with a tip correction model to improve the performance estimates.

A modification of the design tool was made to allow interpolation over multiple 2D aerofoil data sets, including 2D aerofoil geometry, chord-based Reynolds

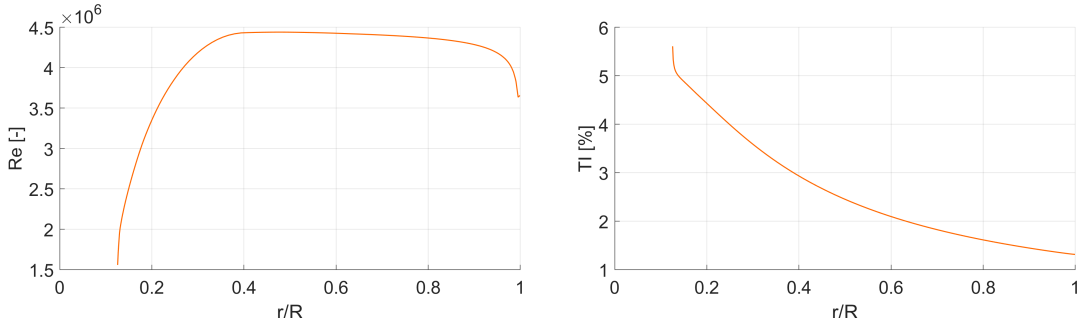

Figure 6.3: Typical Reynolds number (left) and turbulence intensity variation (right) with radial position on a rotor blade of 8 m diameter at $\lambda = 6$. The radius of the hub is 0.125R

number (Re) and turbulence intensity (TI). Figure 6.3 plots the expected variation in Re and TI along the length of a blade. Whilst it appears appropriate to interpolate TI owing to the monotonic variation along the blade's length, the variation in Re is relatively small, especially over the high power producing region of $0.4 < r/R < 0.95$. The advantage that Re interpolation provides is that no new aerofoil data has to be generated when adjusting the target thrust coefficient (c_x) or λ, which change the reference length and velocity in the Re calculations, respectively.

Furthermore, an alteration of the RANS-BE design code, similar to Cao et al. (2019), was included to allow interpolation between 2D profiles of different trailing edge thickness to chord ratio. This approach allowed varied aerofoil sections to be simulated without the explicit 2D modelling of the geometry for the constant trailing edge thickness case examined below.

6.3.1 2D aerofoil simulations

To provide input into the RANS-BE design tool, 2D aerofoil simulations were run for a range of TI and Re. The NACA-63-415 profile was selected for this rotor due to its high lift to drag ratio at high Re and the availability of experimental data to validate this geometry (Bak et al., 2000). This profile belongs to the NACA-63-4XX subfamily of aerofoils which are commonly used in wind turbines (Bertagnolio et al., 2001) and have also been used to design tidal rotors (Laurens et al., 2016).

6.3.1.1 Trailing edge treatment

An analysis varying trailing edge thickness (δ) and thickness to chord ratio (δ/c) of the NACA-63-415 profile examined the trade-off in performance between:

1. Sharp trailing edge ($\delta = 0$) - This edge treatment is the unmodified geometry of the NACA-63-415 profile. While this profile is likely to be the best performing due to the smooth edge transition, the sharp geometry is difficult to manufacture and may introduce a hazard when handling the blades.

2. Truncated trailing edge at constant trailing edge thickness to chord ratio ($\delta/c = constant$) - By applying the thickening function of Xu et al. (2014), the trailing edge thickness can be adjusted to a suitable size for manufacture and handling. Using the same section along the blade's length means that trailing edge thickness is dictated by the smallest chord length of the turbine (often the tip), resulting in an efficiency loss over the other portions of the blade due to unnecessarily thick trailing edges.

3. Constant trailing edge thickness ($\delta = constant$) - Applying the thickening function of Xu et al. (2014) at every section along the blade's length augments the aerofoil profile to maintain a constant thickness trailing edge. This reduces the losses due to an unnecessarily thick trailing edge on sections of the blade with large chord if δ/c is constant, but introduces additional complexity as there is a unique aerofoil profile at each section along the blade's length.

The final two trailing edge treatments in the above involve an iterative approach using the turbine design tool to generate a geometry before applying the desired trailing edge thickness. A minimum trailing edge thickness of 2 mm was chosen for the blade design as the thickness provides durability for manual handling without being too sharp. Minimum and maximum chord lengths of 250 mm ($\delta/c = 0.0080$) and 750 mm ($\delta/c = 0.0027$) were estimated based on a similar turbine design allowing the range of potential δ/c to be defined. Applying the thickening function of Xu et al. (2014) the profiles were thickened following

$$\begin{aligned} x = x_0, y = y_0 & \qquad 0 \leq x \leq x_t \\ x = x_0, y = y_0 \pm 0.5\delta \left(\tfrac{x-x_t}{c-x_t}\right)^n & \qquad x_t \leq x \leq c, \end{aligned} \tag{6.1}$$

where x_0 and y_0 are the original geometry, x and y are the thickened geometry, x_t is the location of maximum thickness along the chord (c), δ is the thickness of the trailing edge and n is a power exponent which is used to control the smoothness of the profile, taken to be 2 in this study. The profiles examined in this study are plotted in Figure 6.4.

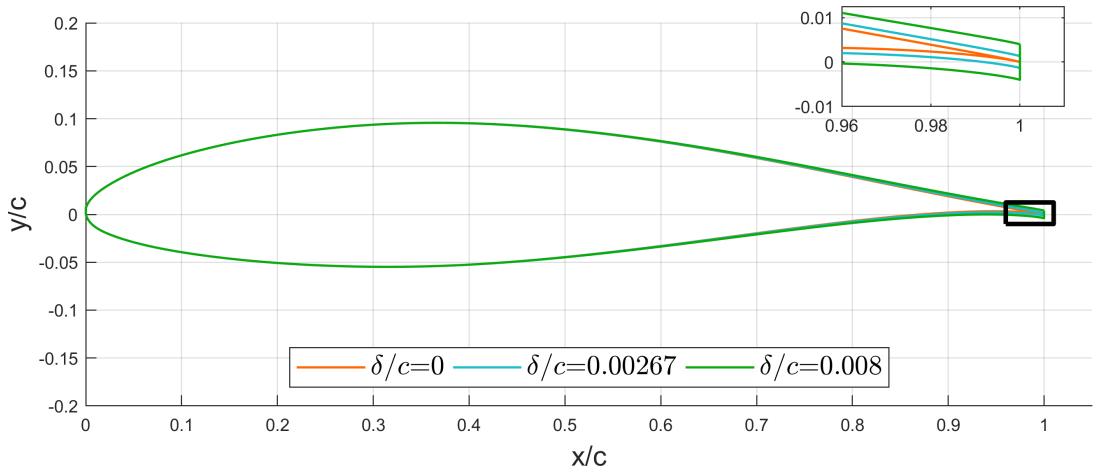

Figure 6.4: NACA 63-415 aerofoil with three different trailing edge thickness to chord ratio thickened following Xu et al. (2014)

6.3.1.2 2D aerofoil analysis

ANSYS Fluent 15.0 (ANSYS Inc., 2013) was used to perform a 2D analysis of the aerofoil sections. Lift, drag and pressure distribution data for four chord-based Reynolds numbers ($Re = [8 \times 10^5,\ 1.6 \times 10^6,\ 3.2 \times 10^6,\ 5 \times 10^6]$) and six turbulence intensities ($TI = [0.98\%, 1.92\%, 3.67\%, 5.27\%, 6.77\%, 8.15\%]$) were calculated for each of the trailing edge treatments.

Calibration results between the 2D numerical model and wind tunnel testing by Bak et al. (2000) are presented in Figure 6.5 for the NACA 63-415 profile without any trailing edge treatment. The experiments were conducted at $Re = 1.6 \times 10^6$ and $TI = 1\%$, which are slightly lower turbulence conditions than expected at the turbine. A favourable comparison observed with regards to c_l and $C_{pressure,min}$,

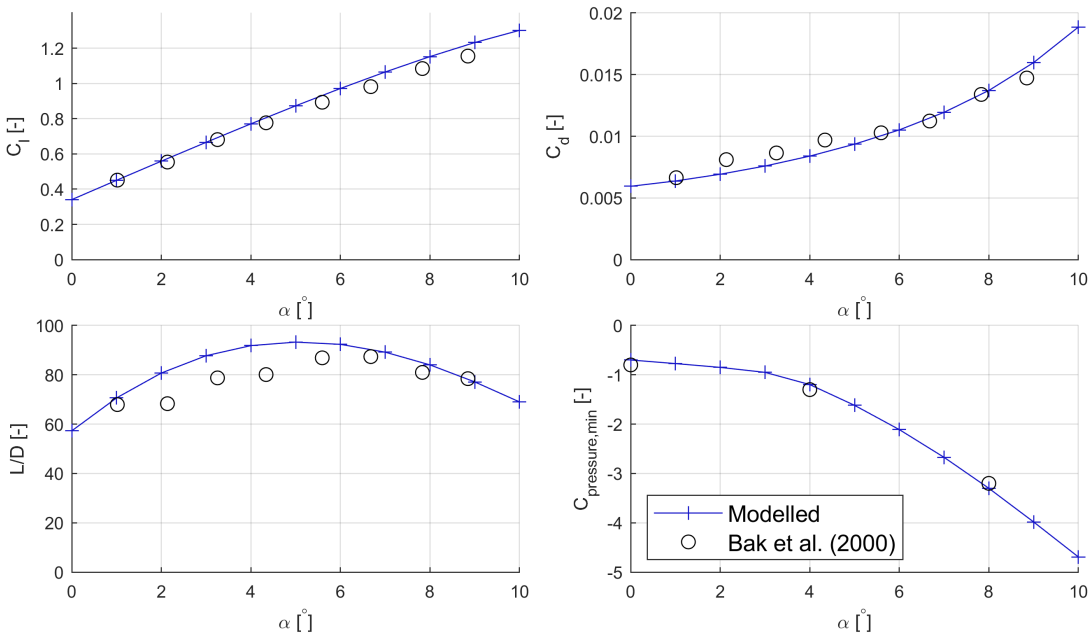

Figure 6.5: Calibration of c_l (top left), c_d (top right), lift to drag ratio (bottom left) and $C_{pressure,min}$ (bottom right) for a NACA 63-415 section at Re =1.6 $\times$ 10^6 and $TI = 1\%$, experimental data was sourced from Bak et al. (2000)

capturing the trend and magnitude of these quantities around the optimal angle of attack. There is a slight discrepancy in the c_d at low angles of attack, given the relatively low values of c_d, this error is compounded in the lift to drag ratio. Nevertheless these errors are within an acceptable range for use in the RANS-BE model. Lift and drag parameters are known to change dramatically during stall, therefore the calibration and analysis in the RANS-BE model was limited to conditions where α was less than 10°.

Results for Re =3.2 $\times$ 10^6 are presented in Figure 6.6; this value corresponds to the approximate chord based Re at 80% span and $\lambda = 6$ with a free-stream velocity of 2.5 m/s. The turbulence intensity has a significant impact on the lift to drag ratio (L/D) which the section can achieve. The primary cause for this is the

increased skin friction with higher TI, which increases c_d. Secondary to this, an increase in c_l is observed at lower turbulence intensity; however, as a proportion, this increase is significantly smaller ($\approx$20 times) than the decrease in c_d.

The simulations also demonstrate that increasing the trailing edge thickness form $\delta/c = 0.008$ to $\delta/c = 0.00267$ results in a lower L/D at the optimal angle of attack, α^*. Like the turbulence intensity, this is due to increased drag (increased drag was observed on thickened trailing edges at $0° < \alpha < 10°$). The thickened trailing edges had a higher α^* which shifted from $\alpha^* = 5°$ for the sharp edge to $\alpha^* = 6°$. This results from a slight reduction in the gradient of the drag coefficient with angle of attack as thickness increases. The cause of this appears to be due to the thickened sections delaying separation on the upper surface of the aerofoil as demonstrated by the zero intercept of the wall shear stress (τ_{wall}) in Figure 6.7.

The minimum pressure coefficient ($C_{pressure,min}$) appears to be relatively insensitive to the trailing edge treatment and turbulence intensity at $\alpha < 5°$. Beyond this value, the magnitude of $C_{pressure,min}$ rapidly increases and TI has greater influence; these results match the wind tunnel testing of Bak et al. (2000). Low $C_{pressure,min}$ indicates a lower pressure over the section, if this pressure drops below the vapour pressure of the liquid small vapour cavities may start to form (cavitation). As these cavities move into high pressure regions they collapse, generating a shock waves which can cause damage in their immediate vicinity. Measures to protect the tidal turbine from cavitation are discussed in Section 6.3.4.

Re also impacts aerofoil performance, as demonstrated by Figure 6.8, which plots the polars for a fixed TI of 1.92%, corresponding to the blade's expected turbulence conditions. Increased Re leads to a higher lift to drag ratio and magnitude of $C_{pressure,min}$.

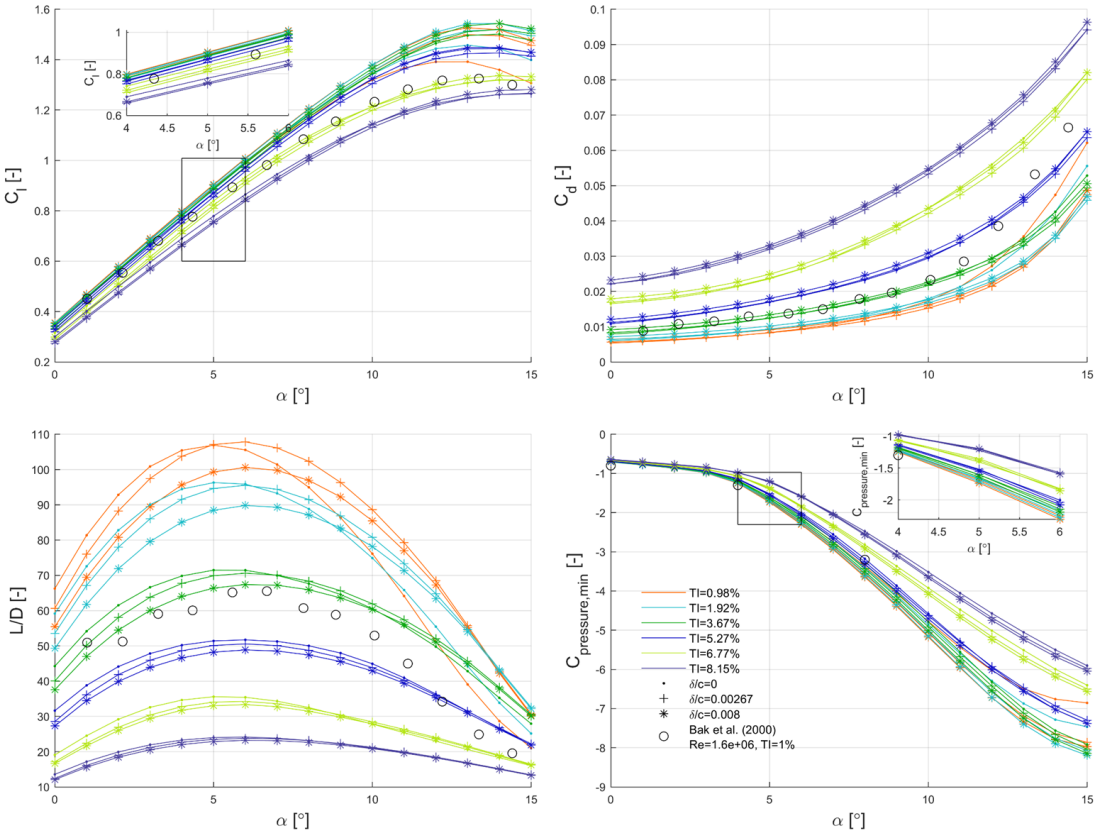

Figure 6.6: NACA 63-415 c_l (top left), c_d (top right), lift to drag ratio (bottom left) and $C_{pressure,min}$ (bottom right) variation with α for different trailing edge thicknesses and turbulence intensities at $Re = 3.2 \times 10^6$.

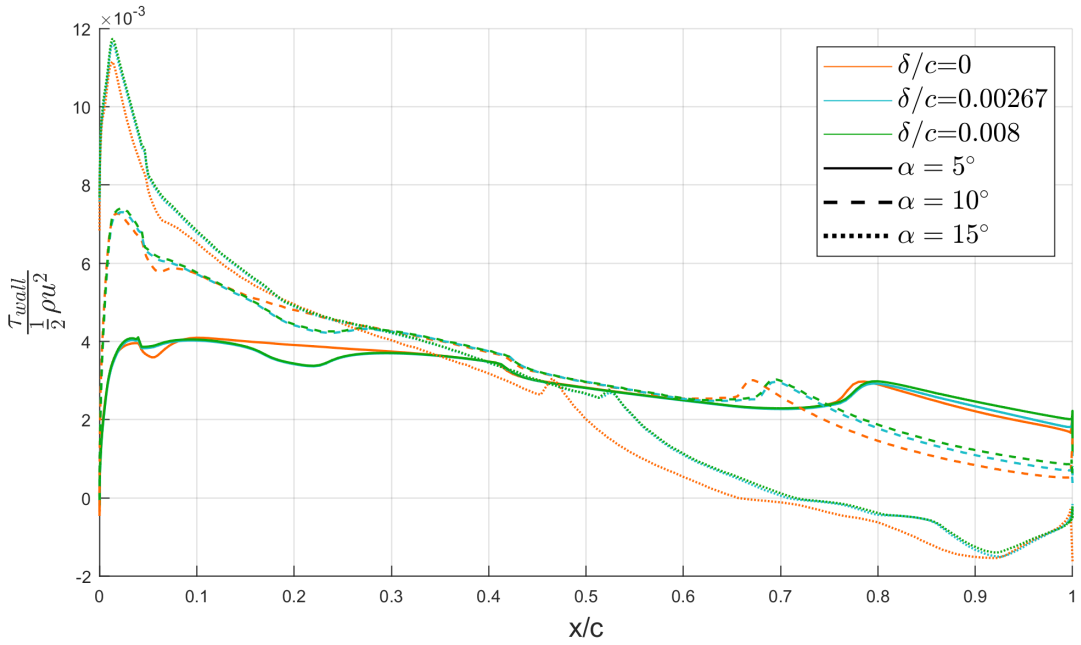

Figure 6.7: Wall shear stress on the suction surface with chord position for a NACA-63-415 profile with varied trailing edge thicknesses at $Re = 3.2 \times 10^6$, $\alpha = [0, 10, 15]°$ and a turbulence intensity of 0.98%

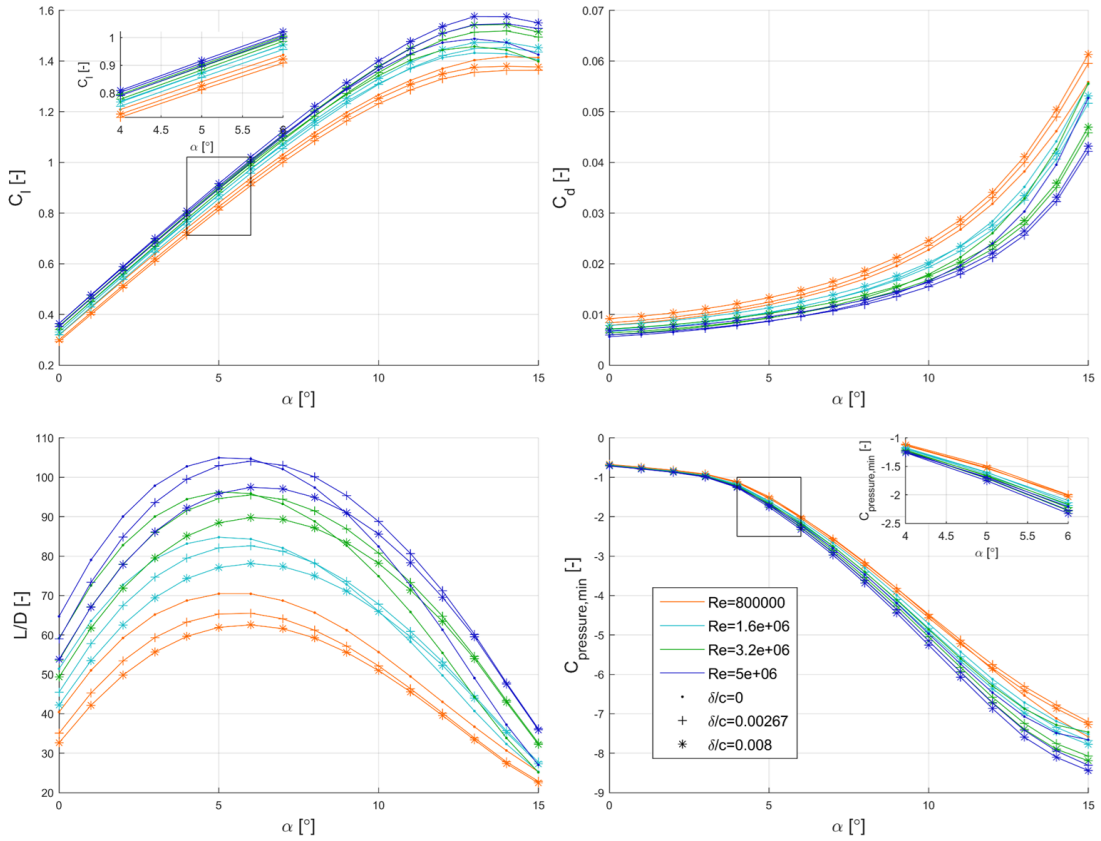

Figure 6.8: Aerofoil c_l (top left), c_d (top right), lift to drag ratio (bottom left) and $C_{pressure,min}$ (bottom right) variation with α for different trailing edge thicknesses and Reynolds numbers at a turbulence intensity of 1.92%.

6.3.2 Model domain

A cylindrical domain of diameter 72.47 m ($9.06D$) was used for the initial rotor design to match the global blockage of 1.2% at the Strangford Lough location. Figure 6.9 plots this domain and highlights the velocity inlet, pressure outlet and symmetry boundary conditions applied in the model. The velocity inlet is 10 D upstream of the turbine with a specified inflow of 2.5 m/s with a turbulence intensity of 8%, which decays to 6% at the rotor plane. A pressure outlet boundary condition was applied 20D downstream of the rotor plane.

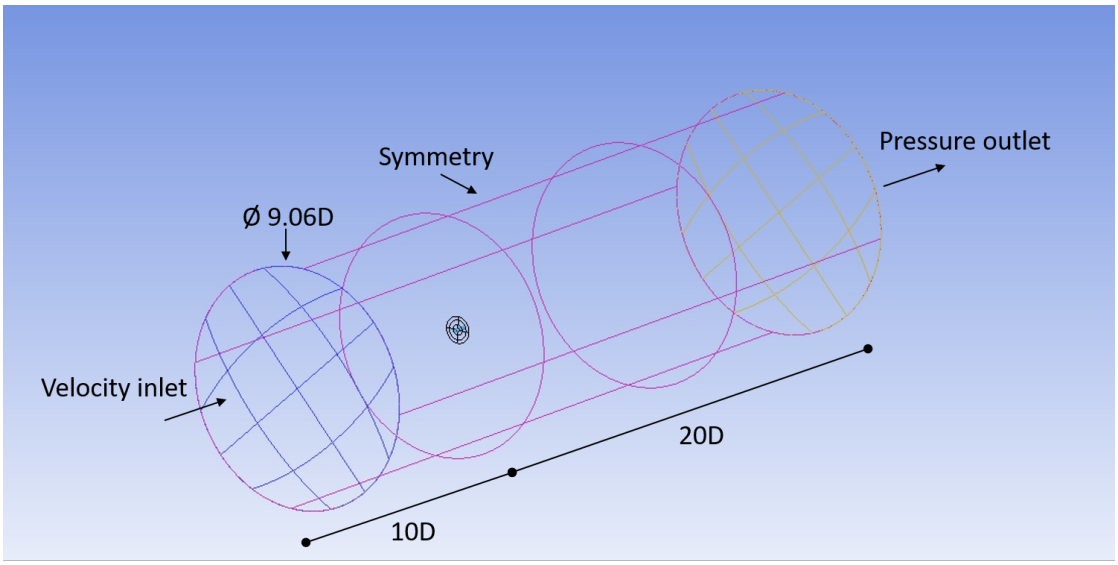

Figure 6.9: Model domain for RANS-BE turbine design.

6.3.3 Mesh convergence study

A mesh convergence study analysed three meshes of varied minimum cell sizing at the rotor's root and tip. A constant mesh growth rate of 1.05 was used in the area immediately surrounding the rotor and nacelle; this was relaxed towards the inlet

Table 6.3: Turbine design tool performance across mesh resolutions.

Mesh name	Minimum element size ($L_{element}/D$)	Number of elements (Millions)	C_p	C_t
Coarse	0.00500	2.7	0.574	0.908
Medium	0.00250	7.3	0.576	0.911
Fine	0.00125	20.0	0.582	0.917

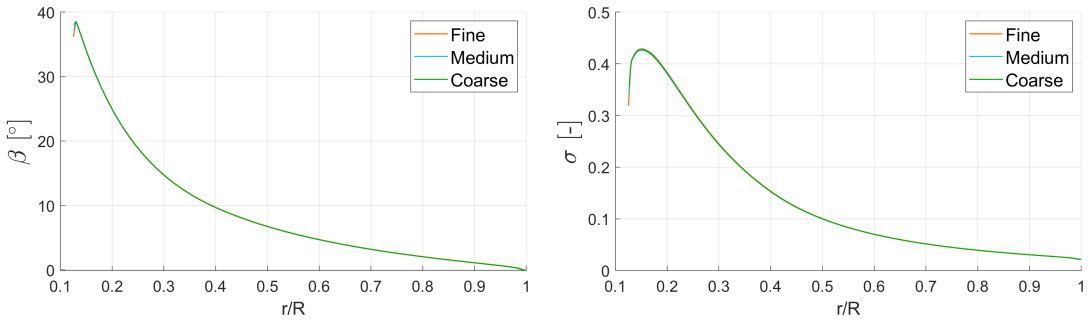

Figure 6.10: Blade twist (left) and solidity (right) distribution from the RANS-BE design tool for varied mesh refinement.

and outlet, where a value of 1.1 was applied. Mesh convergence was assessed based on turbine C_p and C_t. The results are summarised in Table 6.3. The difference in C_p and C_t between the coarse and fine mesh was 1.5% and 1% respectively. The primary cause for this discrepancy is the mesh's resolution in the root region, where the influence of the nacelle and decreased angular velocity causes a rapid change in the required blade twist and solidity. This effect is highlighted in Figure 6.10 with the steep gradient in the near root region; as this location provides little of the overall power output, the medium resolution mesh was adopted.

6.3.4 Tip speed ratio selection

Determining the appropriate λ for design requires balancing rotational speed for optimal performance against the onset of rotor blade cavitation and turbine thrust

as it provides more resistance to the flow. As observed in the 2D aerofoil plots in Figure 6.8, lower turbulence intensity and higher Reynolds number result in an improved lift to drag ratio for the section. From a design perspective, this would suggest that a higher λ should be targeted (if flow diversion effects are ignored due to the higher thrust) as the higher velocity increases the Re and lowers turbulence intensity. However, constraining this problem is the onset of blade cavitation, which can degrade blade surfaces and reduce performance. It is recommended that cavitation be avoided for tidal turbines (DNV GL, 2015).

To satisfy the no cavitation inception criteria when defining λ, an approach modified from Wimshurst et al. (2018) was applied to determine the maximum permissible tip speed ratio (λ_{max}) at a specified depth. The no cavitation requirement constrains the cavitation number (C_a) always to be greater than 0. C_a is defined as

$$C_a = \frac{p - p_v}{\frac{1}{2}\rho W^2} \tag{6.2}$$

where p_v is the vapour pressure, taken to be 2.4 kPa for seawater, W is the relative speed of the flow to turbine blade and p is the static pressure, inclusive of static pressure over the 2D section ($p_{section}$), atmospheric pressure (p_{atm}) and hydrostatic pressure (p_z) at depth z such that $p = p_{section} + p_{atm} + p_z$.

Using the $C_{pressure,min}$ coefficient for the 2D section, an approximate minimum static pressure over the section ($p_{section}$) can be estimated following

$$p_{section} = C_{pressure,min}\frac{1}{2}\rho W^2. \tag{6.3}$$

The critical location for cavitation is at the minimum p along the blade; this was

taken to be the blade's tip when positioned at top-dead-centre (a depth of $Z_{hub} - D/2$) as the hydrostatic pressure is at a minimum. Blade resolved simulations of Wimshurst et al. (2018) demonstrated that this is a conservative assumption as minimum p occurs slightly closer to the nacelle (94% span) due to tip loss effects reducing the suction peak. This effect was ignored for the initial estimates of λ_{max} and a conservative assumption for p_z was used,

$$p_z = \rho g(Z_{hub} - D/2). \tag{6.4}$$

Finally, an approximation of the velocity magnitude was made by assuming that the axial and tangential flow induction factors at the tip were 0 and 1, respectively, allowing

$$W \approx \sqrt{u_\infty^2 + (\Omega R)^2}. \tag{6.5}$$

This assumption is reasonable given the rotational component of velocity is much greater than the axial component and is also conservative as the higher velocity results in a more significant suction peak. λ_{max} can now be expressed as a function of Z_{hub} for a given α following

$$\lambda_{max} = \frac{\sqrt{\frac{2(p_v - p_{atm} - \rho g(Z_{hub} - D/2))}{\rho C_{pressure,min}} - u_\infty^2}}{u_\infty}. \tag{6.6}$$

Figure 6.11 plots λ_{max} for flow conditions expected at the blade tip for varying depths. It can be observed from this figure that α plays an essential role in defining λ_{max} and that reducing the blade twist at the tip may permit a higher λ_{max}. Secondary to this, increasing trailing edge thickness decreases the λ_{max} of the rotor; this is due to the higher suction peaks on the thickened aerofoils.

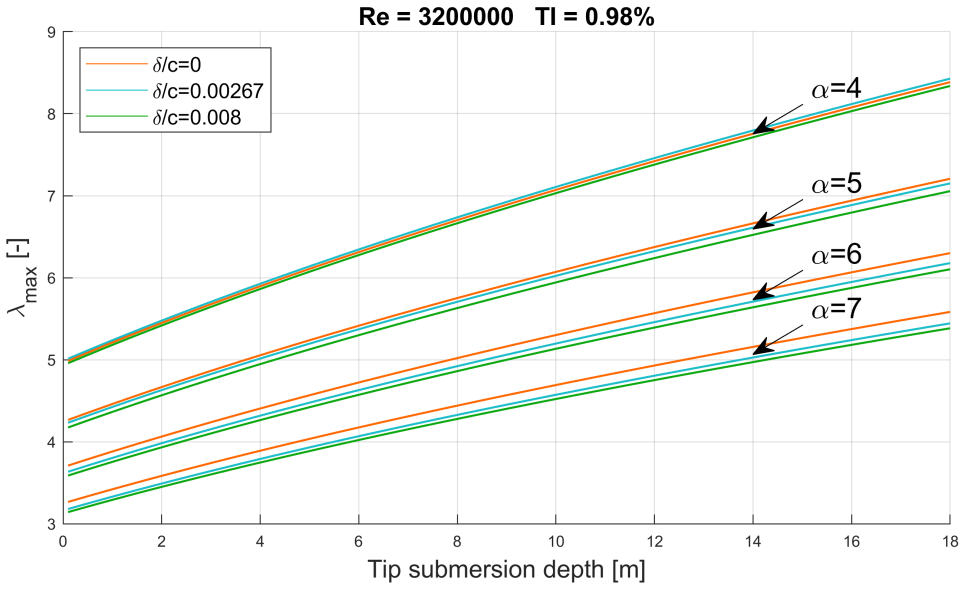

Figure 6.11: Variation in λ_{max} with tip submersion depth for Re =3.2×10^6 and turbulence intensity 0.98% which are typical conditions expected for the D=8 m rotor design. Depending on the trailing edge thickness, α^* is either 5° ($\delta/c = 0$) or 6° ($\delta/c > 0$).

To maximise the available energy passing the turbine, it is advantageous to select a rotor depth as close as practical to the water surface due to the flow's shear profile, this height has to be balanced against the impact of waves on the rotor. A smaller submersion depth is also beneficial for a floating turbine as the smaller lever reduces the moment on the platform. A rotor hub submersion depth of 1/3rd the water depth (10 m) was determined based on a comparison to Orbital Marine's O2 device (Orbital Marine Power, 2019). This provides a tip submersion depth of 6 m which corresponds to a $\lambda_{max} \approx 4.5$ for $\alpha^* = 6$.

The analysis suggests several ways to increase the λ_{max} if desired. These include modifying the section towards the tip to have a lower suction peak or increasing the blade twist angle to target a lower angle of attack. The latter strategy is indirectly employed in this study as a Glauert tip correction factor is not used in the blade

design process. The tip correction accounts for the effect of the span-wise flow and tip vortex by reducing the free-stream flow component; not including the factor will, therefore, reduce the attack angle at the rotor's tip for the design.

6.3.5 Blade trailing edge

Three rotors were designed using the modified RANS-BE design tool with the edge treatments described in Section 6.3.1.1 for $\lambda = 4.5$, $c_x = 2$ and $\alpha^* = 6$. Turbine C_p and C_t of each design case are presented in Table 6.4. Despite the sharp trailing edge section being the best performing for the lift to drag ratio, maintaining $\delta = 0.002$ m over the blade results in a slightly higher C_p. This is primarily due to the higher lift of the thickened sections at low turbulence intensity and the slight difference in drag between the sections (discussed further in Section 6.3.1.2). Given this result, it may be surprising that the performance of the $\delta/c = 0.008$ design case is slightly worse than the $\delta = 0$ m case. Figure 6.12 illustrates that c_l reduces towards the inboard section with increasing TI. However, the $\delta = 0$ m is slightly less sensitive to this change allowing the section to have a higher performance in the hub region than the $\delta/c = 0.008$ case. The tangential thrust coefficient (c_θ) and the section torque coefficient (c_q) are plotted in Figure 6.13 to highlight each radial station's contribution to the rotor performance. These coefficients are defined as

$$c_\theta = c_l \sin(\phi) - c_d \cos(\phi) \tag{6.7}$$

$$c_q = c_\theta \frac{r}{R}. \tag{6.8}$$

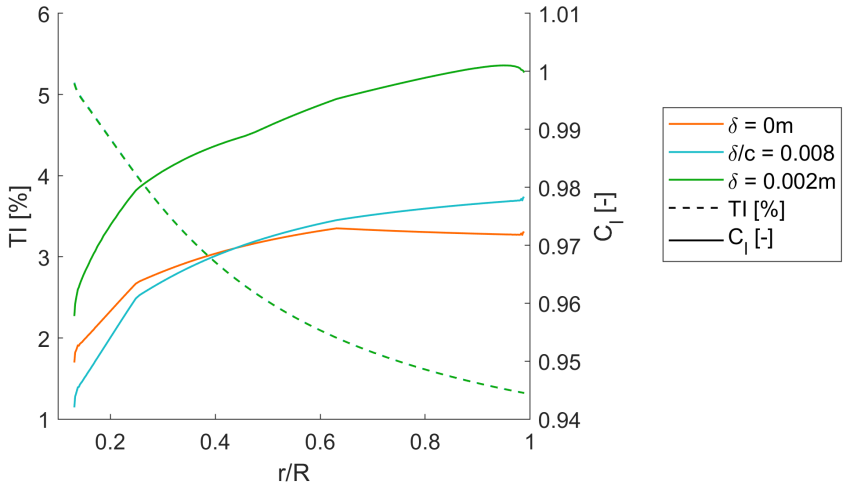

Figure 6.12: c_l and TI variation with radial position for rotors designed with various trailing edge treatments.

Figure 6.13 shows that the hub region is the reason the $\delta = 0$ m design has superior performance to the $\delta/c = 0.008$ design. It is worth noting that both designs have a similar c_q towards the tip due to the slightly higher c_d for the $\delta/c = 0.008$ design negating the improvement in c_l. The $\delta = 0.002$ m case is able to maintain a higher c_l towards the root due to the increased chord length reducing δ/c closer to $\delta/c = 0.002$ which has a higher c_l than the $\delta = 0$ m dataset for the TI (Section 6.3.1.2).

Table 6.4: Rotor performance for turbines designed with different trailing edge treatment at $\lambda^* = 4.5$, $c_x = 2$ and $\alpha^* = 6°$.

Trailing edge treatment	$\mathbf{C_p}$	$\mathbf{C_t}$
Sharp ($\delta = 0$ m)	0.575	0.927
Varied δ ($\delta/c = 0.008$)	0.573	0.927
Constant δ ($\delta = 0.002$ m)	0.580	0.928

Overall, the slight differences in performance between the rotors and the similar

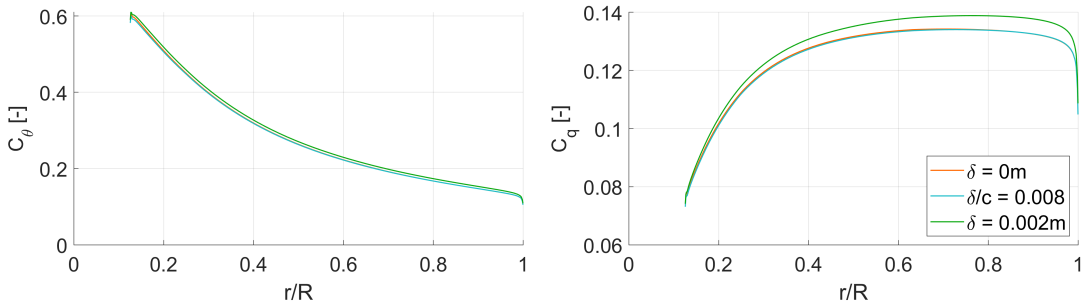

Figure 6.13: c_θ (left) and c_q (right) variation with radial position for rotors designed with varied trailing edge treatments.

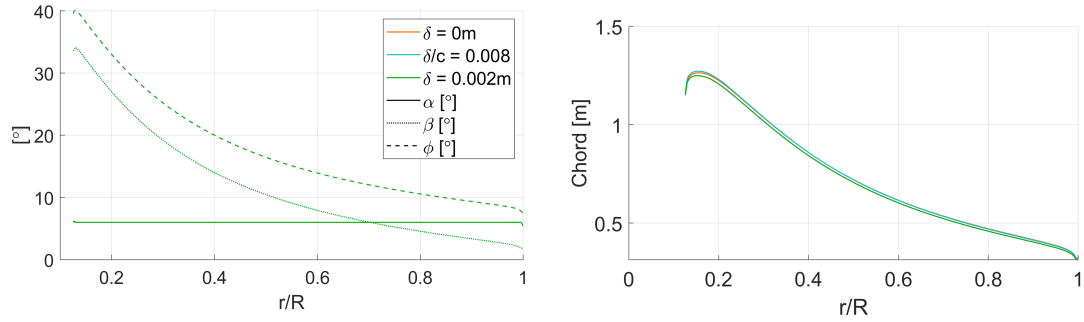

Figure 6.14: Span-wise distribution of blade twist angle (β), angle of attack (α) and their sum (ϕ) (left) and design chord length (right)

blade twist and solidity distributions, as observed in Figure 6.14, imply the choice of blade trailing edge is of little consequence to the overall design. Therefore, practical design and safety (not having a sharp edge) are likely to be the limiting factor in trailing edge choice. For this reason, the $\delta = 0.002$ m case was selected for the final design.

6.3.6 c_x adjustments

Optimising the target c_x is an important step in the design process as it impacts overall rotor thrust and performance. Physically, increasing c_x largely corresponds to increasing chord length. To develop higher values of c_x rotor solidity and thrust

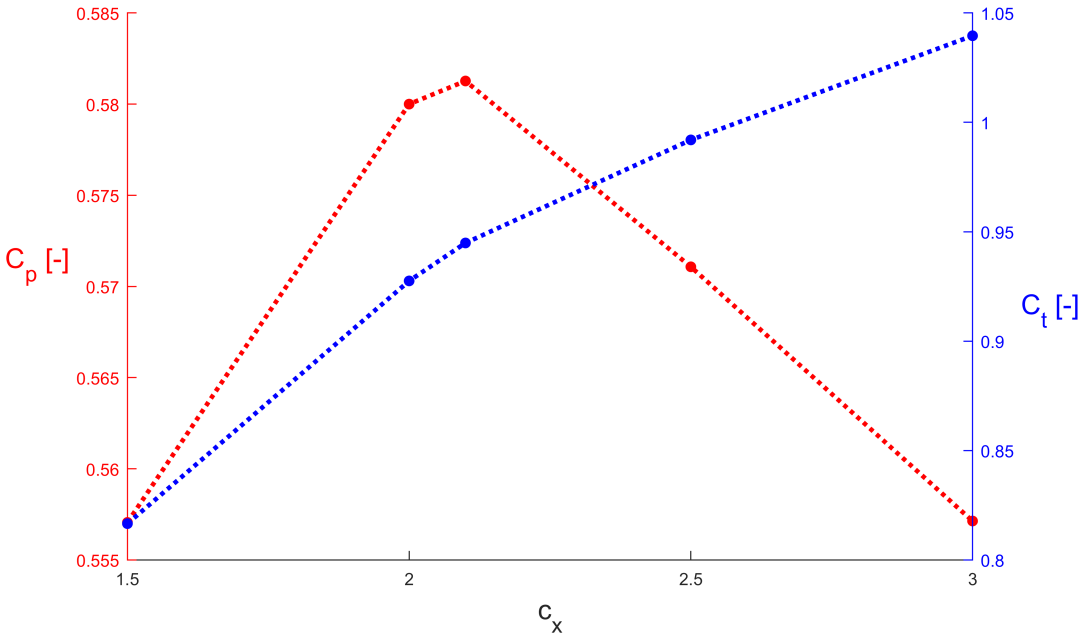

Figure 6.15: C_p and C_t variation with design c_x at λ=4.5. c_x is uniform along the blade span.

are higher, causing a reduction in the stream-wise velocity and requiring the blade twist to be adjusted to achieve the target angle of attack. Consequentially c_θ (and c_q) is augmented following Equation 6.7 and 6.8; these values should be maximised over the blade through the optimisation of c_x.

The optimal c_x, where c_x is kept uniform along the blade, for $\delta = 0.002$ m and λ=4.5 was determined through a two-stage iteration process. This process first determined C_p for three c_x before interpolating a quadratic between the data and selecting the optima for the next iteration. The process converged rapidly, avoiding unnecessary simulations. Results are plotted in Figure 6.15, which shows a maximum C_p of 0.584 when $c_x = 2.1$ was used.

While optimising a uniform c_x along the blade's length is essential for improving power production, physical limits exist for the chord length. Specifically, high

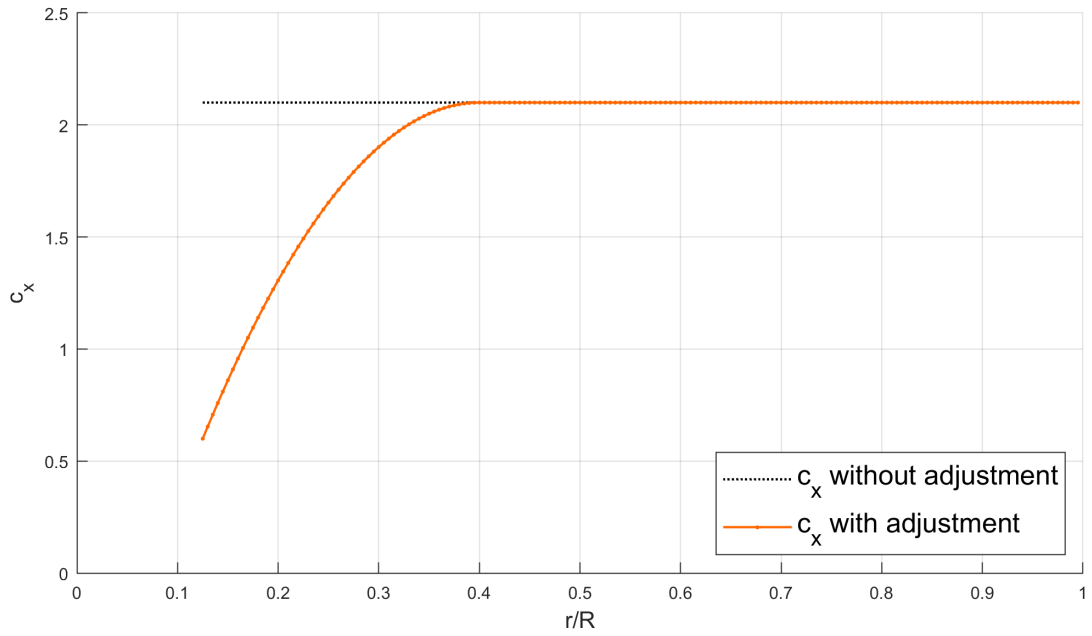

Figure 6.16: Variation in design c_x along the rotor blade.

target c_x can cause intersecting blade geometries, especially in the root region. This was observed for all c_x examined in this study. Consequentially, c_x was curtailed in the root region using a smoothing function to increase c_x from 0.5 at the nacelle (r/R=0.125) to 2.1 at r/R=0.4; this blending function is plotted in Figure 6.16. A limit for blade solidity is non-trivial to include in the design code due as it requires a consideration for the twist angle and the profile thickness as blades can overlap if the twist allows. The curtailment of c_x resulted in a marginally higher C_p (C_p=0.584) than the c_x=2.1 case (C_p=0.581). This is due to the optimisation of c_x uniformly along the blade and not at every radial station. When this parameter is allowed to vary a slightly higher C_p is possible.

6.3.7 Final geometry

The geometry was adjusted at the blade tip and root to limit rapid changes in blade shape. At the root section, a limit on the rate of reduction in σ was applied due to the influence of the boundary layer from the nacelle on the RANS-BE design tool. As this region is close to the nacelle, it has a relatively small influence on the turbine's power production. The adjustment made at the tip is a minor correction to limit the reduction in σ and β in this region. The need for this adjustment at the tip is due to the RANS-BE design tool not including a tip correction model, resulting in artificially high thrusts in this region, reducing blade σ and β. Applying this tip correction causes a reduction in power of 8.8%, this is the product of two factors. Firstly, not including a tip correction in the design leads to sub-optimal design parameters over this region. Secondly, artificially high thrusts exist at the tip when the correction is not applied as no load reduction is accounted for, resulting in an overestimate of power.

The geometry corrections were made by extrapolating β and σ using the gradient of the profile at r/R=0.175 and r/R=0.95 for the root and the tip respectively (producing a smooth geometry to the first derivative). The resulting geometry profiles are presented in Figure 6.17, and the impact of this adjustment on the power and thrust can be observed in Table 6.5. The table shows a change in C_t of 0.1% when the geometry adjustment is applied to the design.

6.4 Blade resolved MRF simulation

MRF (Multiple Reference Frames) simulations were run to improve the estimates for power and thrust, investigate blade tip treatment and develop the meshing

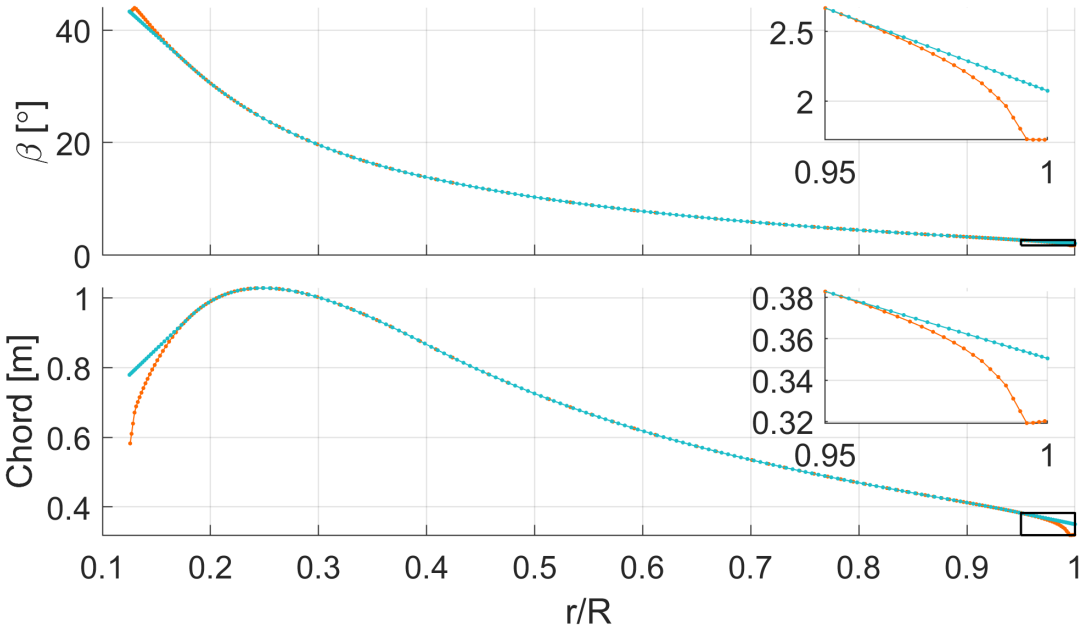

Figure 6.17: Original (orange) and extrapolated (blue) turbine geometry; extrapolation has used the gradient at the outer 5% of the blade to define the geometry beyond these extents.

Table 6.5: Impacts of design modifications on performance.

Turbine design condition	C_p	C_t
$c_x = 2.1$	0.581	0.945
Curtailed c_x	0.584	0.935
Curtailed c_x + tip correction	0.530	0.888
Curtailed c_x + tip correction + geometry adjustment	0.530	0.889

strategy for sliding mesh simulations. The MRF method modifies the Navier-Stokes equations within a sub-domain surrounding the blade and solves them in a moving reference frame. This approach permits steady solution methods, provided that the inflow conditions are steady, allowing for a computationally efficient simulation that resolves the blade geometry without needing a sliding mesh. Further details on the MRF method can be found in Chapter 2.

6.4.1 Model domain

The model domain was identical in size to the RANS-BE simulations except for the flow cross-section, which was reduced to a 120° sector by exploiting the rotor's azimuthal periodicity. The additional faces introduced to the model from splitting the domain were replaced with periodic boundaries to replicate the complete cylindrical domain. The model was divided into two sub-domains, the first being the outer domain and the second being an inner domain. The inner domain used a rotating reference frame to simulate the rotation of the turbine. Figure 6.18 highlights the two domains and the boundary conditions used in this model.

6.4.2 Mesh convergence

Mesh convergence was assessed using structured and semi-structured meshing approaches. Structured meshes offer control to users, requiring them to specify node distribution on the edges within the domain, as a consequence this method requires a significant amount of user input, especially for complex geometries. In contrast semi-structured methods take input parameters (such as a global mesh growth rate and maximum element size) to generate a mesh from the geometry.

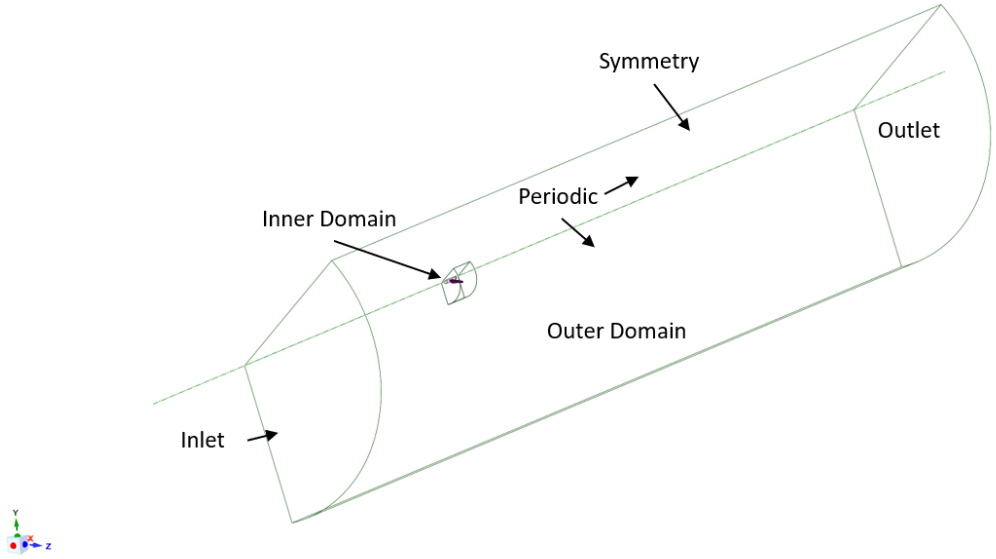

Figure 6.18: MRF Domain highlighting the inner and outer domains and boundary conditions.

Consequentially, semi-structured meshes are faster to create but may lack the resolution around the area of interest which can be achieved using structured methods. To address this short coming, improvements to semi-structured meshing software have allowed user specification of node distribution and mesh growth rates normal to surfaces using inflation layers. This leads to a mesh very similar to a structured mesh close to surfaces and a conventional unstructured mesh in the remaining domain; this approach is used for the semi-structured mesh presented in this section.

6.4.2.1 Structured mesh convergence

A block-structured hexahedral mesh was developed using ANSYS ICEM (ANSYS Inc., 2012). The mesh parameterisation was similar to that of Cao et al. (2018); however, the near wall resolution was modified due to the higher turbulence conditions permitting the use of the $k - \omega$ SST turbulence model. This turbulence

model used an enhanced wall treatment which models the boundary layer and requires either resolution in the viscous sublayer ($y^+ < 5$) or in the outer log-law region ($y^+ > 30$). Model resolution $5 < y^+ < 30$ places cells in the buffer region where this model has been shown to be less accurate (ANSYS Inc., 2013).

Table 6.6 summarises the results from a mesh convergence study for the blade area-weighted-average y^+ ($\overline{y^+}$) and near-wall growth rate ($GR_{NearWall}$). A $GR_{NearWall} = 1$ indicates a buffer layer with elements of uniform thicknesses normal to the surface. Overall the C_p and C_t for the rotor was most sensitive to the $\overline{y^+}$ range tested with a $\overline{y^+} < 66$ having <1% error; all $GR_{NearWall}$ tested also resulted in <1% error in C_p and C_t.

Table 6.6: Structured mesh convergence checks

Variable	$\overline{y^+}$	$GR_{NearWall}$	$\frac{C_t^c - C_t}{C_t^c}$	$\frac{C_p^c - C_p}{C_p^c}$
$\overline{y^+}$	**217.6**	1	-2.46%	-3.10%
	107.8	1	-1.02%	-1.36%
	65.9	1	-0.45%	-0.66%
	32.7	1	0.00%	0.00%
$GR_{NearWall}$	32.6	**1.2**	0.42%	-0.08%
	32.7	**1.1**	0.33%	-0.11%
	32.4	**1.05**	-0.22%	-0.32%
	32.7	**1**	0.00%	0.00%

The superscript c in C_t^c and C_p^c indicates that results are taken from the highest resolution for the given test variable.

Despite similar performance for integrated quantities for the range of $GR_{NearWall}$ tested, there is a significant difference in the pressure distribution around the blade in the range of $0.2 < r/R < 0.5$. The stability of the solution in this region is insufficient for the two most coarse meshes ($GR_{NearWall} = [1.10, 1.20]$) but appears to be stable for the lower growth rates. This is demonstrated in Figure 6.19.

The mesh selected for this design adopted a $GR_{NearWall}$ of 1.05 and had a $\overline{y^+}$

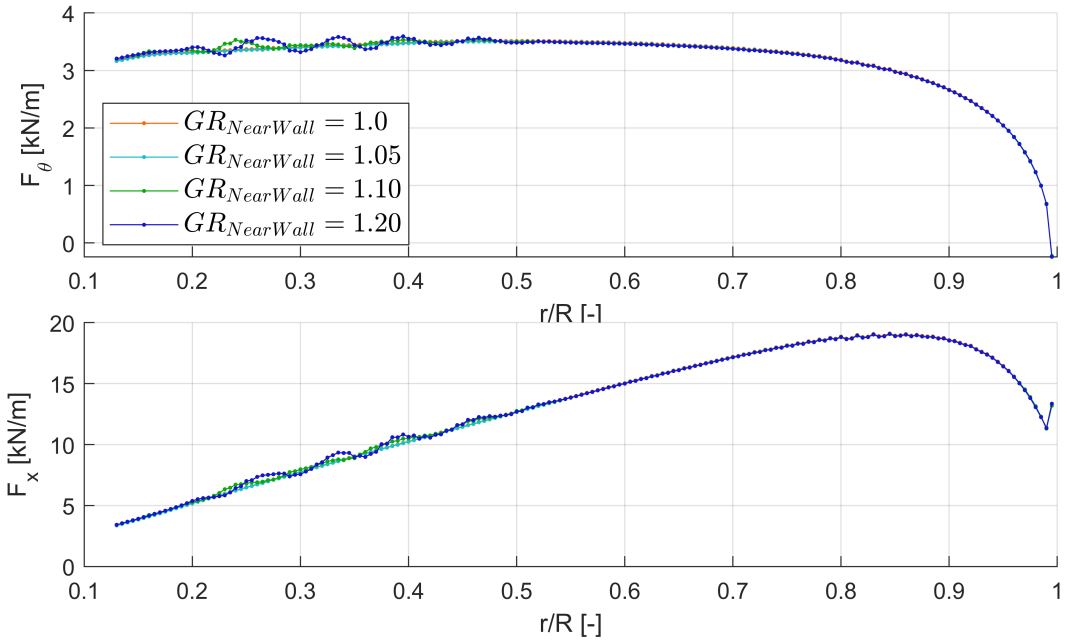

Figure 6.19: Tangential (top) and stream-wise (bottom) force distribution per unit span along the length of the rotor blade for varied $GR_{NearWall}$.

of 66.

6.4.2.2 Semi-structured mesh convergence

A semi-structured meshing approach was used in this study to develop a quick-to-build mesh with the capacity to have controlled refinement in the areas of interest. Primarily this method relied on developing a gridded face meshing on the blade surface (similar to structured approaches) and utilised inflation layers over the surface to generate a mesh capable of resolving a close-to-uniform y^+. Outside of the near-wall region, unstructured tetrahedral elements were used to fill the remaining model domain, reducing the user input time requirements. An example mesh demonstrating this parameterisation is presented in Figure 6.20. As can be observed in this figure the level of control over the near blade mesh resolution is

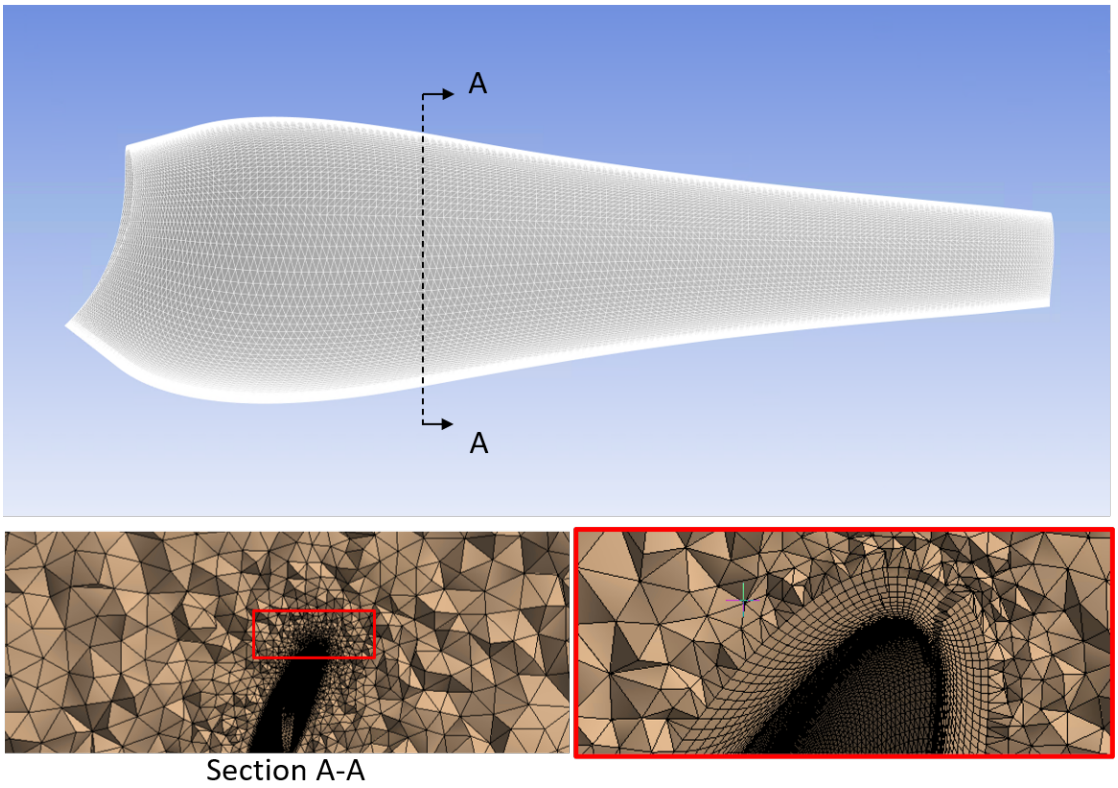

Figure 6.20: Mesh on blade surface (top). Cross section of mesh through blade geometry demonstrating the semi-structured mesh (bottom left). Zoomed view of blade tip showing inflation layers and the transition to unstructured mesh (bottom right).

nearly identical to that of structured methods.

A mesh convergence check, similar to that presented in the previous section, was undertaken. This study included additional variables to further examine the solution accuracy. These variables included:

- N_{chord} - Number of elements in the 2D cross-section
- GR_{chord} - Growth rate in the chord-wise direction
- N_{radial} - Number of elements in the radial direction (along the blades length)

- N_{blunt} - Number of element on the trailing edge

Table 6.7: Semi-structured mesh convergence checks

Variable	$\overline{y^+}$	N_{chord}	GR_{chord}	GR_{outer}	N_{radial}	N_{blunt}	$\frac{C_t^c - C_t}{C_t^c}$	$\frac{C_p^c - C_p}{C_p^c}$
$\overline{y^+}$	**120.7**	160	1.1	1.2	175	4	-0.95%	-1.08%
	60.8	160	1.1	1.2	175	4	-0.40%	-0.24%
	30.3	160	1.1	1.2	175	4	0.00%	0.00%
N_{chord}	29.5	**80**	**1.2**	1.2	175	4	0.42%	-0.10%
	30.3	**160**	**1.1**	1.2	175	4	0.43%	0.46%
	30.2	**320**	**1.05**	1.2	175	4	0.00%	0.00%
GR_{outer}	30.3	160	1.1	**1.2**	175	4	0.06%	-0.17%
	30.3	160	1.1	**1.1**	175	4	0.00%	0.00%
	N/A*	160	1.1	**1.05**	175	4	N/A*	N/A*
N_{radial}	30.3	160	1.1	1.2	**175**	4	-0.07%	0.04%
	30.3	160	1.1	1.2	**525**	4	0.00%	0.00%
N_{blunt}	30.3	160	1.1	1.2	175	**4**	0.13%	0.16%
	30.2	160	1.1	1.2	175	**8**	0.00%	0.00%
	N/A*	160	1.1	1.2	175	**16**	N/A*	N/A*

* Note that these simulations were unstable and results are not available.
The superscript c in C_t^c and C_p^c indicates that results are taken from the converged mesh, assumed to be the highest resolution for the given test variable.

Like the structured mesh, the range of parameters tested resulted in small changes in C_p and C_t; these results are presented in Table 6.7. Additionally, pressure distributions at radial stations and force distributions along the blade's length were examined for mesh convergence. Figure 6.21 and Figure 6.22 show the pressure and resultant force distribution along the blade's length for a varied N_{chord}. These plots demonstrate that force and pressure distributions are similar at the rotor's mid-span; however, there are some discrepancies between simulations towards the hub and the tip. Most noticeably, the force distribution in the stream-wise direction at $r/R = 0.80$ in the lower resolution mesh predicted a higher force than the others.

Additionally, the suction side's pressure distribution at $r/R = 0.99$ showed

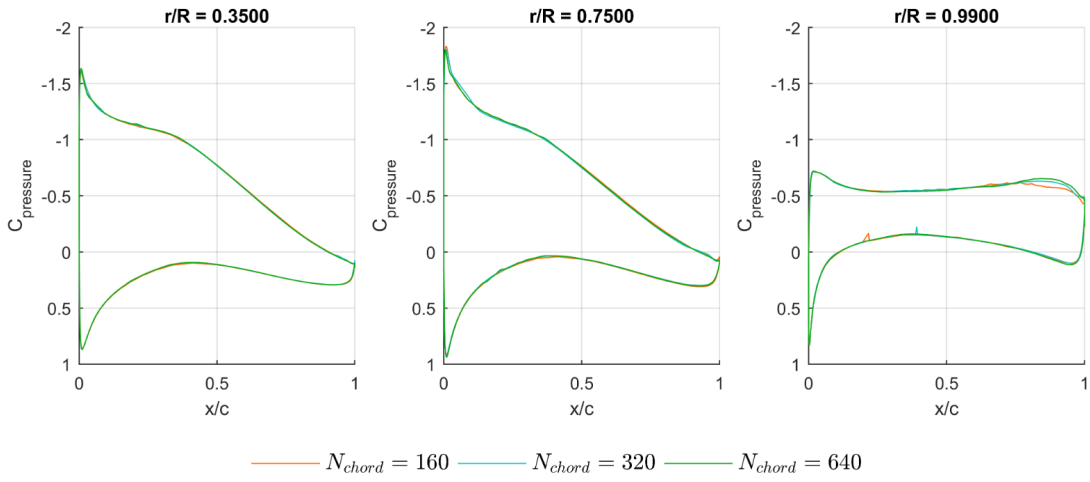

Figure 6.21: Pressure distribution around at $r/R = 0.35$ (left), $r/R = 0.75$ (middle) and $r/R = 0.99$ (right) for varied chord resolution using a semi-structured mesh.

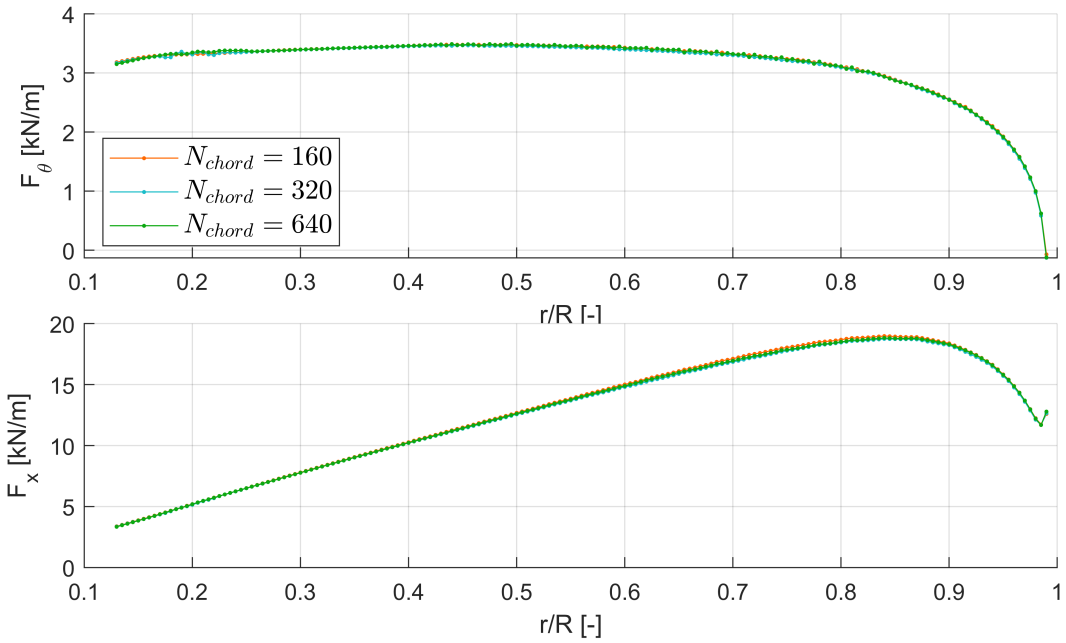

Figure 6.22: Tangential (top) and stream-wise (bottom) force distribution along the length of the rotor blade for varied N_{chord}.

two suction peaks in the higher resolution meshes. The secondary peak in suction pressure is not a result of improved aerofoil performance; instead, it is due to pressure equalisation between the suction and pressure surfaces towards the middle chord due to the tip vortex.

The converged mesh used a $\overline{y^+} = 30.3$, $N_{chord} = 160$, $GR_{chord} = 1.1$, $GR_{outer} = 1.2$, $N_{radial} = 175$ and $N_{blunt} = 4$, for all these parameters there was $< 0.5\%$ difference in C_p when using a higher resolution model.

6.4.2.3 Comparison between mesh approaches

Results for C_p and C_t between the two mesh types were similar with the structured mesh having a $C_p = 0.494$ and $C_t = 0.871$ and the semi-structured mesh producing a $C_p = 0.492$ and $C_t = 0.871$ at the design $\lambda = 4.5$. Examining the force and pressure distributions along the blade's radius (Figure 6.23 and Figure 6.24), it is apparent that differences in the meshing approaches are subtle, with only a small difference in the force distribution at $0.85R$. Given the similarity in the pressure distribution on the rotors, secondary factors were considered when selecting the appropriate mesh. Ultimately the semi-structured mesh was selected due to the simulations being 25% faster than the structured despite the semi-structured mesh containing more elements (3.1×10^6 for the structured and 3.5×10^6 for the semi-structured). This result is specific to the geometry tested and is unlikely to be true for all other applications.

6.4.2.4 Turbine tip

The effect of turbine tip shape was investigated by comparing the flat tip used in the mesh convergence study with a rounded tip. The rounding treatment used a

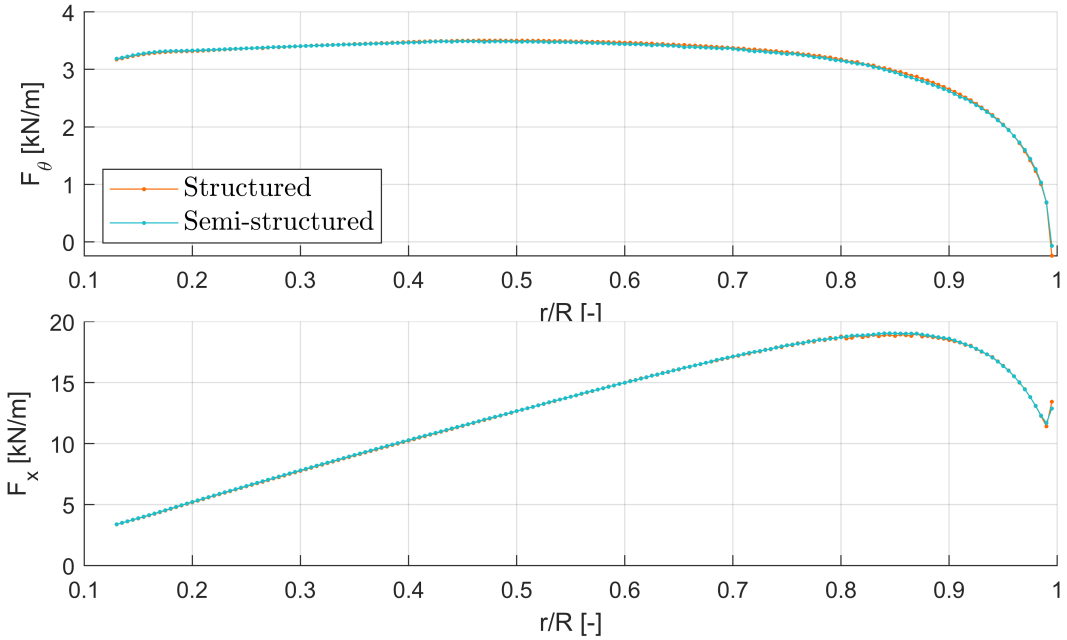

Figure 6.23: Tangential (top) and stream-wise (bottom) force distribution along the length of the rotor blade for structured (orange) and semi-structured (blue) meshes.

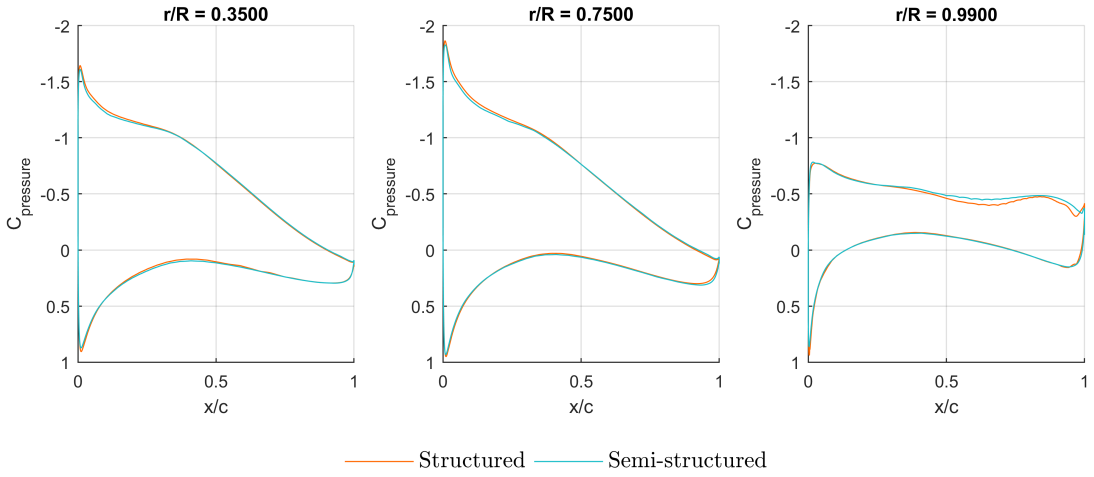

Figure 6.24: Pressure distribution around at $r/R = 0.35$ (left), $r/R = 0.75$ (middle) and $r/R = 0.99$ (right) for structured (orange) and semi-structured (blue) meshes.

semi-circle centred on the chord line to connect the suction and pressure surfaces; this resulted in a slight increase in blade radius from 4 m to 4.026 m. Results from the MRF simulations had no observable difference between the two tip treatments outside the tip region. Consequently, the change in C_p and C_t for the curved tip was small, with a 0.37% reduction in power and a 0.63% reduction in thrust compared to the flat tip.

Figure 6.25 and Figure 6.26 show the static pressure distribution on the blade tip and the radial velocity near the blade. The pressure plot demonstrates that rounding the tip reduces the pressure on the pressure surface and increases pressure on the suction surface as radial flow along the blades permits pressure equalisation. This is confirmed in Figure 6.26 which shows a slightly more significant impediment to the flow as it passes from the pressure to the blade's suction surface.

Ultimately, due to the flat blade tip's higher power generating capacity, this design was selected despite the marginally higher stream-wise thrust.

6.5 Sliding mesh

A sliding mesh was constructed by tessellating the 120-degree MRF mesh about the rotor hub to generate a complete turbine's geometry in a cylindrical channel. The domain was identical to that used in the RANS-BE model (Section 6.3) except that the mesh defines the whole rotor geometry. A rotational mesh motion was defined for the inner domain to simulate the turbine operating at $\lambda = 4.5$ and a sliding interface was prescribed between the inner and outer domains. This removed the need for azimuthal periodicity imposed from the MRF approach. The model was run using a second-order unsteady implicit solver ANSYS Fluent 19.2 (ANSYS

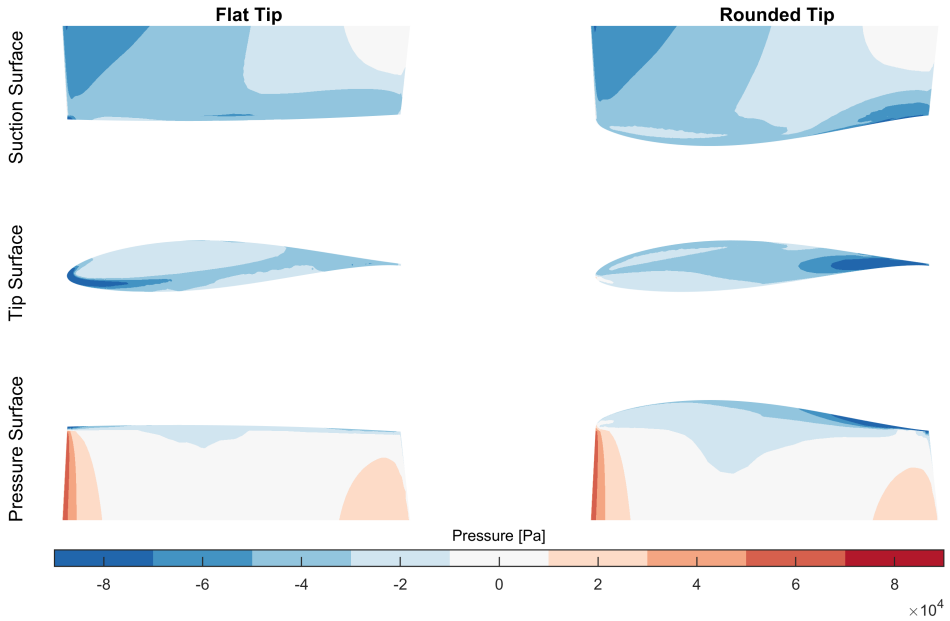

Figure 6.25: Static pressure on the blade tip for flat (left) and curved (right) geometries.

Inc., 2018).

6.5.1 Time-step convergence

An analysis of time-step convergence was performed by running a series of simulations with varied time-step size and the number of iterations carried out per time-step. The results of this study are shown in Figure 6.27. This figure presents the magnitude of the continuity residual and the real-time taken to complete one rotation of the turbine on a 16 core compute node from the Oxford ARCUS cluster with the marker's colour and size, respectively. This figure highlights how important the choice of time-step is to produce accurate results within an acceptable time frame. Further to this there is a limitation on the time-step size to prevent the sliding domain from jumping past cells any cells on the interface between the

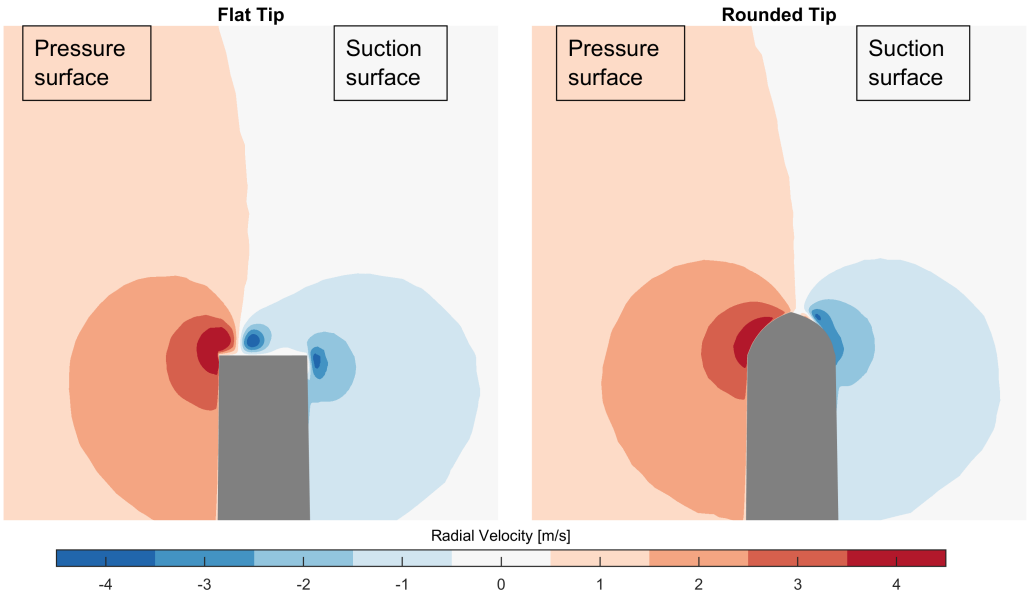

Figure 6.26: Radial velocity on a plane intersecting the 33% chord and aligned with the free-stream flow near the blade tip (blade twist at the tip is 2.1°) for flat (left) and curved (right) geometries. Free-stream flow direction is left to right.

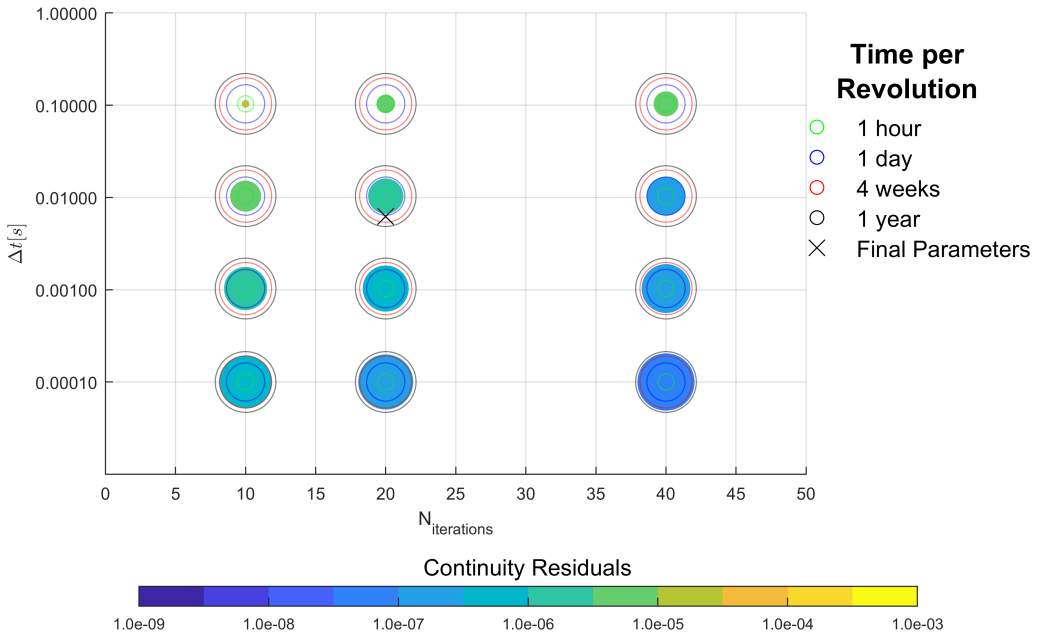

Figure 6.27: Magnitude of the continuity residual for varied time-step and number of iterations per time-step. Size of the marker reflects the real time taken to simulate a complete rotation of the turbine on a 16 core node on the Oxford ARCUS cluster.

static and sliding domains.

Ultimately a time-step size of 0.00621 seconds with 20 iterations per time-step was selected (0.5° rotation per time-step) due to it balancing the performance with the simulations time, taking approximately 1 day to simulate a rotation. Results from this parameterisation appeared to converge within the first 10 rotations; an additional 5 rotations (15 total) were used to confirm this. The average CFL over the domain was 0.498; using the implicit scheme avoided restrictive conditions imposed by the CFL within the explicit solver.

6.5.2 Single turbine performance

The sliding mesh results were similar to those generated from the MRF simulations, confirming that the MRF model's assumptions are valid for this model domain. Results for C_p and C_t were constant over the rotation, just marginally higher ($\sim$0.5%) than those produced in the steady MRF simulations. Some difference is expected between the results as the solution switches from a steady to an unsteady solver. Given the close agreement between the models, the mesh and time-stepping method was deemed fit for purpose and suitable for further fence scale simulations.

6.6 Comparison of turbine models

Three numerical methods of simulating tidal turbines have been used in this chapter to design an 8 m diameter turbine. As the numerical methods increased in complexity with each iteration (RANS-BE $\rightarrow$ MRF $\rightarrow$ Sliding mesh), the capacity to alter the design was reduced. Ultimately, this resulted in a close to optimal design (and practical) but not the best design for performance. This is due to the lower order models' underlying limitations, carrying design errors through to the higher-order models. Figure 6.28 plots the C_p and C_t predicted from each of the three model types used in this study. The plot shows that the MRF and sliding meshes have close agreement at the design λ and highlights how the accuracy of the RANS-BE model changes (relative to the MRF model) over the range of λ. C_t appears to be captured reasonably well by the RANS-BE model ($\pm$3%) at $\lambda > 3$. Below $\lambda = 3$ the RANS-BE model accuracy is reduced, most likely due to the increased angle of attack on the blade inducing stall; stall is not accurately captured by the 2D dataset or within a steady simulation. RANS-BE C_p has a

more significant error than C_t, which is expected given that C_p is proportional to u^3 whereas C_t is proportional to u^2, compounding any errors in the velocity in this parameter. C_p is also sensitive to the angle of attack and reliant on the torque distribution along the blade, increasing errors further towards the blade's tip due to the higher lever arm.

Figure 6.29 plots the tangential and stream-wise force distribution along the blade's length for each of the model types used in this study. The MRF and the Sliding mesh models produce close to equivalent results; however, significant errors are observed in the RANS-BE model, most noticeable at the hub and the tip regions. The limitation of the RANS-BE model in capturing vortex shedding (both at the tip and the hub of a rotor) has been well studied with correction models being developed to try and account for these effects (Hansen and Johansen, 2004; Moriarty and Hansen, 2005). While these models are not perfect, they bring more physics into the model and improve the solution when used correctly. In this case, the Glauert tip correction appears to underestimate the losses from the rotor blade, leading to higher overall C_p and C_t for the RANS-BE case.

The RANS-BE results are only marginally higher across the mid-span of the rotor blade than the other methods. Given that the mid-span of the blade has the weakest span-wise flow components and, therefore, most closely resembles the 2D cases which drive the RANS-BE tool, this result is expected.

The RANS-BE model performs poorly around the hub. While this may be of low consequence for power generation (as torque production is low over this region), it further highlights the differences between the models. The RANS-BE model used in this study did not include a hub correction model meaning the drop in force observed at the hub is not a result of a vortex shedding. Instead,

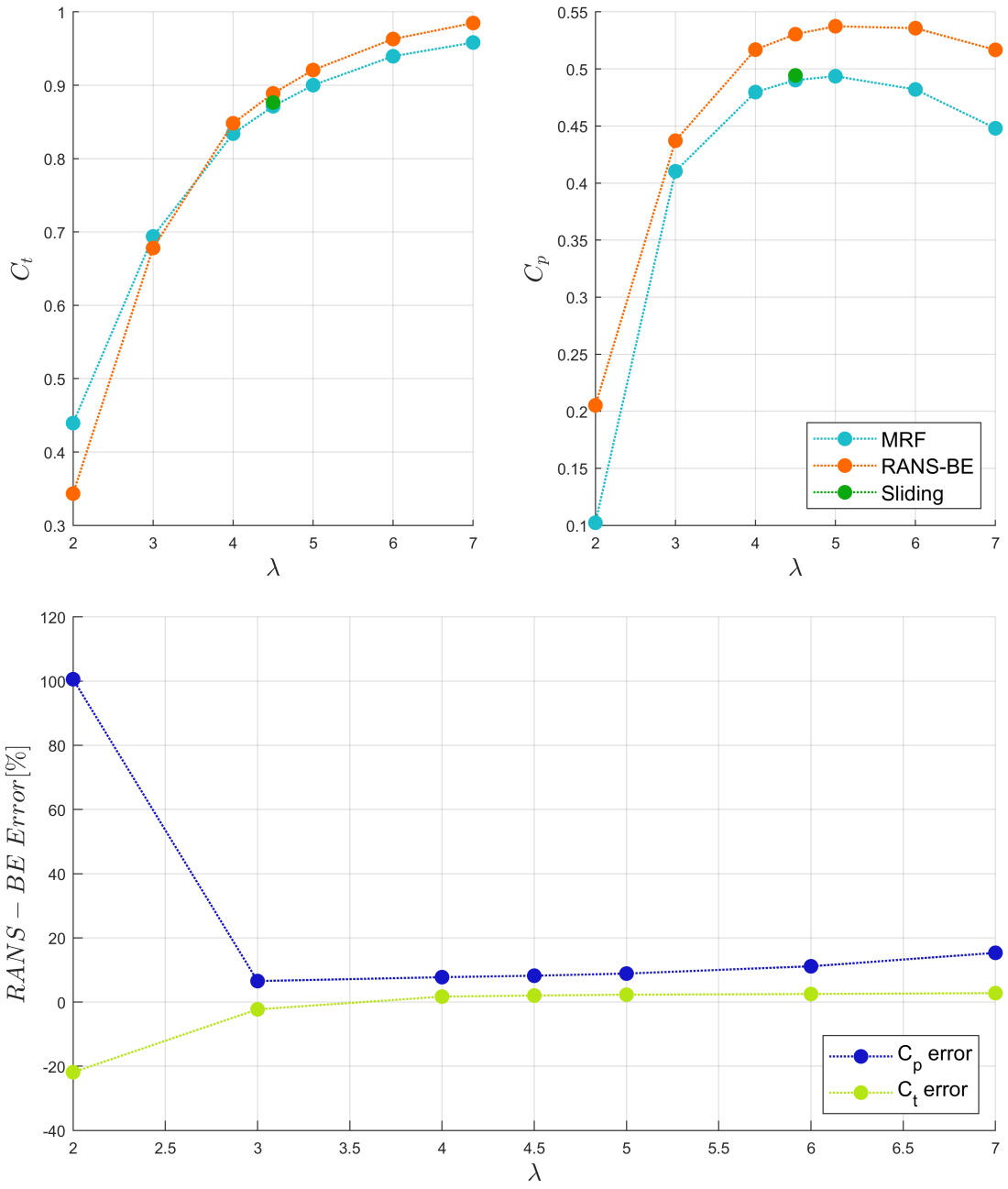

Figure 6.28: C_t (top left) and C_p (top right) variation with λ for the three model types used in this study. The bottom plot shows the error in the RANS-BE results relative to the MRF results.

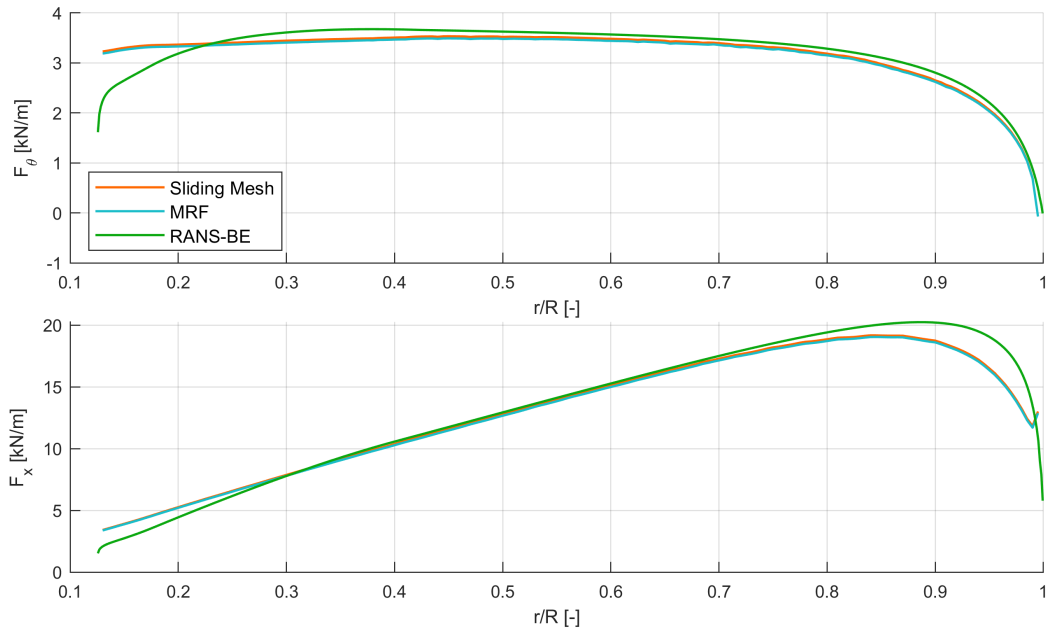

Figure 6.29: Force distribution along the blade length from RANS-BE (green), MRF (blue) and Sliding mesh (orange) simulations.

this observation may be credited to the velocity definition used in the RANS-BE model and the change in pressure distribution over the blade due to span-wise flows. Figure 6.30 shows a comparison of the stream-wise flow component (u_x) for the RANS-BE model and the Sliding mesh model at 30°, 60°, 90° and 120°. Note that the Sliding mesh model is periodic, so the selected values represent points at every 30° in a complete rotation, and the blade passes through the plane at 120°.

Figure 6.30 shows that the RANS-BE model does an excellent job of capturing the average stream-wise velocity; this is expected given the BE formulation performs azimuthal averaging. What is shown in this plot by the Sliding mesh results is that after the blade passes (30°) to just before the subsequent blade passing (90°), the stream-wise velocity recovers from the previous blade passing. This exposes the incoming blade to a higher stream-wise velocity than the average (used

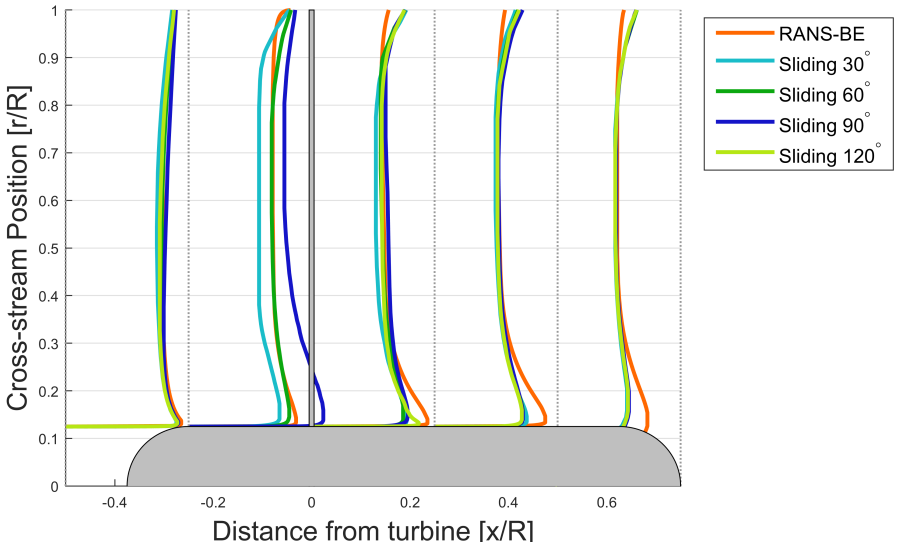

Figure 6.30: Stream-wise velocity profiles from RANS-BE and Sliding mesh simulations around the turbine. The blade positions in the Sliding mesh results are at 0°, 120° and 240°, due to the radial symmetry in the problem data is plotted at 30° increments between 0-120° which is equivalent to 30° increments around the entire rotor.

in the RANS-BE). As the velocity at the blade is determined from stream-wise and rotational contributions following

$$W = \left[(\Omega r + u_\theta)^2 + u_x^2\right]^{1/2} \tag{6.9}$$

this effect is more prominent towards the hub as the angular velocity component dominates outside this region. As a result of the underestimated stream-wise velocity, the angle of attack is lower in the RANS-BE model than the MRF and sliding meshes.

Furthermore, due to the span-wise flow, the pressure distribution around the 2D aerofoil is changed; this is clear when examining the $C_{pressure}$ variation at different radial stations from the sliding mesh model (Figure 6.31). Towards the

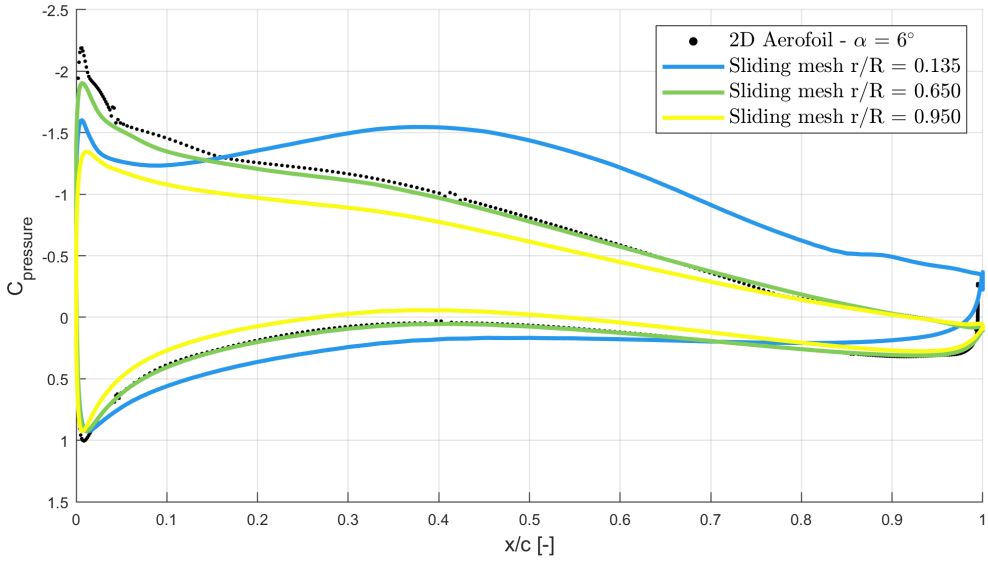

Figure 6.31: $C_{pressure}$ variation towards the hub ($r/R = 0.135$), mid-blade ($r/R = 0.65$) and tip ($r/R = 0.95$) from the Sliding mesh simulations plotted alongside the $C_{pressure}$ from the 2D simulations at the turbine design target α.

tip and the turbine's hub, it is clear that the pressure distribution does not match that for the 2D section at the design angle of attack ($\alpha = 6°$). At the tip, α decreases to 4° and at the hub, the shape of the pressure distribution is completely changed. Presumably, this is due to the span-wise flow component being significant when compared to the relative velocity of the blade (W), modifying the pressure distribution.

6.7 Conclusions

A design for an 8 m diameter rotor has been developed to operate in a global blockage of 1.2%. The design approach adopted gradually increasing model complexity with each design iteration considering more practical constraints to manufacture

and aiming to fix design parameters in place before using the more complex models to refine the design.

2D airfoil data was generated for a NACA-63-415 aerofoil for varied trailing edge treatments operating in a range of turbulence intensities and Reynolds numbers. This data was input to a modified RANS-BE design tool that interpolated for the inflow conditions and between aerofoil profiles to maintain a constant trailing edge thickness of 2 mm. Analysis of the pressure distribution on the aerofoils determined that cavitation initiation may be a limiting factor in the turbine's design operating speed, and an upper limit for λ was defined through a simplification of Wimshurst et al. (2018) which took conservative estimates for flow speed relative to the turbine blades and the critical location for the inception of cavitation.

The RANS-BE design was used and further refined in MRF simulations, where both structured and semi-structured meshes were compared. The difference in blade loading between the structured and semi-structured meshes was negligible when the appropriate inflation layers parameterisation was used. This result validates the use of the semi-structured meshing with near-wall inflation layers for the application to tidal turbine rotors.

Sliding mesh simulations were completed to validate the MRF model and determine the appropriate time-stepping for the transient model. A time-step of 0.00621 s (0.5° rotation) with 20 iterations per time-step was sufficient for this application matching the MRF simulation results closely.

Comparing the three models used in this study highlighted the RANS-BE model's limitations in capturing the physics of the flow near the blade root and tip within a tidal turbine rotor. Specifically, the RANS-BE model's failure to simulate span-wise flows (which violate the underlying assumptions of BE theory), the

unsteady fluid mechanics and skewed inflows relative to the turbine plane were all contributors to the error in the RANS-BE model.

The rotor operates at a design λ of 4.5 and achieves a C_p of 0.494 and C_t of 0.871 when in a cylindrical channel with a global blockage of 1.2%. This design meets the requirement of fully turbulent conditions over the blades and is practical for further blade resolved analysis at the fence scale using the $k-\omega$ SST turbulence closure scheme. The design is derived from a first pass through the design procedure. Further optimisation of the rotor is possible, especially at the root and the tip; however, this would come at a high computational cost as lower-order RANS-BE methods do not adequately capture the physical processes in these regions and a more computationally expensive method, such as the MRF technique, would be required.

Chapter 7

Yaw control of turbine fences

This chapter analyses the performance of a four turbine long fence by making adjustments to the yaw of the outermost turbines to constrain the flow and improve flow alignment. Building on the methods used in Chapter 4, where a turbine fence endwall was used to constrain the flow, this chapter examines a correction for the cross-stream flow component at the ends of a fence which cause a loss in end turbine performance. The correction is made by yawing the outer turbines within the fence to align them with the primary flow direction. Alternative yaw angles are also considered to investigate lateral confinement from the outer turbine on the fence. Yaw control is a practical method of providing lateral confinement for larger turbines (such as that designed in Chapter 6) as no additional structures are required were they to rotate about their existing tower connection. For this study, to avoid confusing the impact of yaw with changing local blockage (pivoting about the tower changes the inter-turbine spacing), a constant tip-to-tip spacing is maintained by yawing the outer turbine around the inner-most point of the turbine swept area.

7.1 Yaw of turbines

7.1.1 Single turbines

Misalignment of flow with the rotor plane is common in both wind and tidal turbines due to the continually varying flow direction. In the horizontal direction misalignment from normal to the turbine plane is referred to as yaw (Ψ). Yawed inflow to turbines is typically considered undesirable for a single turbine due to reduced volume flux through the rotor and inefficiencies from blade advancing and retreating effects; this effects is well understood for wind (Galloway et al., 2014; Bastankhah and Porté-Agel, 2016; Micallef and Sant, 2016; Dou et al., 2019) and tidal (Musa et al., 2020) turbines. Over one half of a rotation, a yawed turbine blade advances into the flow, increasing the relative velocity between the fluid and the blade and decreasing the blade angle of attack. Over the other half of the rotation, the blade and fluid are moving in the same direction, decreasing their relative speed and increasing the angle of attack. This is of concern for a tidal turbine as the variation in the angle of attack and relative flow speed results in increased unsteady loading, which can be detrimental to turbine life span.

Bahaj et al. (2007) quantified some of the effects of yawing a turbine in their experimental study of a single turbine at various yaw angles within a cavitation tunnel. This work provided a comprehensive data set of power and thrust measurements for a range of yaw angles (Ψ), tow speeds and tip-speed-ratios (λ). This data set is commonly used when evaluating numerical model accuracy for tidal turbines in yawed flow, see e.g. (Park et al., 2016; Baratchi et al., 2017). Shahsavarifard and Bibeau (2020) also performed experiments on a yawed rotor, noting that the power loss was negligible for yaw angles smaller than 10° due to

the strong relationship between the power output and the cosine of the yaw angle. Beyond this angle, there was a rapid decrease in performance. While this result highlighted the importance of correctly aligning rotors with the oncoming flow direction, it also suggests that there is scope for small yaw adjustments of turbines.

Numerically, several methods have been used to model yawed turbines. Galloway et al. (2014) accounted for the effects of yaw with a geometric correction to the inflow in an unsteady Blade Element Momentum (BEM) model. While the results captured the variability in blade loading, it was inaccurate when combined with additional flow phenomena, such as waves, under-predicting the peaks in blade root bending moment. Baratchi et al. (2017) compared both an actuator disk and actuator line model of a yawed turbine to the results of Bahaj et al. (2007). The work showed that superior performance could be achieved from an actuator line than a disk model due to its ability to capture wake unsteadiness and the root and tip vortices; however, both models tended to over-predict power and thrust. Superior model accuracy was observed in Park et al. (2016) using a blade resolved sliding mesh model which was also compared to the results of Bahaj et al. (2007). This model accurately captured the variation in power and thrust with yaw, however, this method is known to be computationally intensive as it resolved the blade geometry and motions explicitly.

7.1.2 Turbine fences

The previous section referenced studies which have been conducted for solitary turbines in yawed flow, however due to the high installation cost and capacity to share

infrastructure between turbines, it is likely that tidal turbines may operate in close proximity to each other as an array. As discussed in Section 2.2, closely-spaced turbines offer an additional benefit of producing higher power output through the local blockage effect.

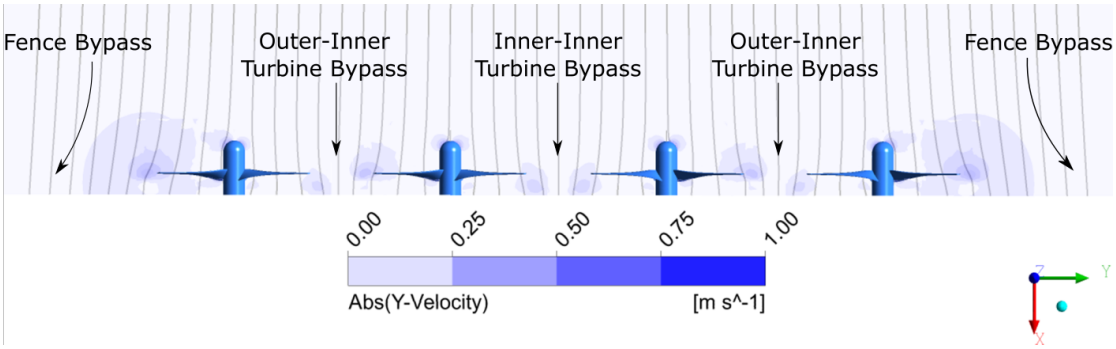

Figure 7.1: Streamlines of flow approaching a turbine fence, highlighting the greater flow diversion around the end turbines over the inner turbines. The contours are the absolute value of the cross-stream flow velocity.

While there is typically an improvement for all turbines within a fence when spacing is reduced, the performance of the outermost turbines lag behind as they do not experience the same onset flow as the inner turbines. End turbines do not have an adjacent turbine on both sides to constrain the flow, consequently, the approach flow towards the ends of the fence has a cross-stream flow component. This results in the outboard turbines encountering flow with a yaw component. Figure 7.1 demonstrates this effect for a fence of four turbines. A greater cross-stream flow component is present over a larger area at either end of the fence than towards the middle. This so-called "end effect" has been investigated experimentally by Cooke et al. (2015) who used porous discs to examine the effects of inter-turbine spacing in a flume. Cooke et al. (2015) observed a reduction in performance of the outboard turbines, this result was supported numerically by Vogel and Willden

(2017) and Vogel and Willden (2019) who observed a similar reduction in end turbine performance along a four turbine long fence using a RANS-BE model. More recently model turbines have been used by McNaughton et al. (2021) to perform towing tank tests of two turbines, specifically designed for high blockage conditions, adjacent the tank side-wall (which emulated a symmetry plane) and a full scale floating fence installation in Nova Scotia was analysed by Jeffcoate et al. (2021) (turbines were not design for blocked flow conditions). Both of these experiments showed a slight performance improvement for the outer turbines within the fence. The results of McNaughton et al. (2021) and Jeffcoate et al. (2021) are still the subject of further investigation to understand why the outer turbine have higher power. Nevertheless, consistent across all this work is the observation of a performance variation along the fence.

To compensate for the diversion of the approach flow at the ends of a turbine fence, this chapter investigates outer turbine yaw to align the rotor normal to the local flow direction. Misalignment of the approach flow contributes to azimuthal variations in blade loading as the incident flow vector varies with the blade passing inboard and outboard of the fence. This is of relevance to turbine fence operators as the fluctuating blade loading may contribute to turbine fatigue. A secondary objective of yawing the outermost turbines within the fence is to also reduce this load variation. This is analysed using a blade resolved sliding mesh model of the fence, purpose-built to simulate a tidal fence of 4 turbines.

7.2 Methodology

7.2.1 Simulated turbine

A four turbine fence of 8 m diameter (D), three-bladed turbines spaced at s/D=0.25 was used in this study. The turbine was designed using the Reynolds-Averaged Navier-Stokes (RANS) embedded Blade Element (BE) method outlined in Chapter 6, this method accounts for the effects of local blockage through implementing McIntosh et al. (2011). Some alterations to the design were made towards the tip and root of the rotor to avoid rapid transitions in blade twist and intersecting blade geometries. A NACA-63-415 aerofoil profile was used along the length of the blade; the 2D aerofoil data input to the RANS-BE model was generated using ANSYS Fluent 19.2 ANSYS Inc. (2013). The turbine was designed to operate at a tip-speed-ratio (λ) of 4.5 in order to limit cavitation at its operational depth (10 m) based on an approximation following Wimshurst et al. (2018). The tip-speed-ratio was defined as $\lambda = \omega R/u_\infty$ for this study, where ω is the rotational speed of the turbine, and R is the turbine radius. Within this study, λ has been scaled by the free-stream flow speed (u_∞) and not the free-stream flow normal to the rotor ($u_{x'}$).

7.2.2 Computational model

Analogous to the turbine fence modelled in Chapter 4, a fence of four turbines (two outer and two inner rotors) was analysed in a planar fence configuration with an inter-turbine spacing of $s = 0.25D$. The turbine fence was modelled in ANSYS Fluent 19.2 (ANSYS Inc., 2013) using a transient sliding mesh method.

This method solves the unsteady RANS equations over multiple domains; an inner domain which contains the turbine geometry and outer domain which prescribes the channel boundaries, an interface surface connects the domains. The turbine movement is directly simulated though a rotational transformation of the inner domain. The four turbine long fence, was positioned at the centre of a 550 m wide and 30 m deep channel ($B_g = 1.2\%$) matching the channel dimensions of Strangford Lough in Northern Ireland. The fence was submerged at a nacelle depth of 10 m. To exploit the system's symmetry and reduce the computational cost, the rotors were designed to be counter-rotating about the fence's centre and positioned around the channel's centerline. This halved the computational load as only two turbines needed to be modelled by exploiting model symmetry. Figure 7.2 shows the computational domain highlighting the boundary conditions applied to the model. A uniform inflow velocity of 2.5 m/s was applied at the inlet.

This simulation's computational mesh took the unstructured rotor mesh from Section 6.5 and filled the surrounding domain with unstructured tetrahedral elements. In total, the mesh contained 23 million elements for the two rotor domain. This element count was kept relatively small due to the high Re of the simulation permitting the use of the $k-\omega$ SST turbulence model. The unsteady Reynolds-Averaged Navier-Stokes equations were solved over a total of 12 complete turbine rotations.

7.2.3 Yawed turbine simulations

Seven yaw angles ($\Psi = [-10°, -5°, -2.5°, 0°, +2.5°, +5°, +10°]$) were investigated as part of this study. The yaw angle was defined by a rotation of the outer turbine

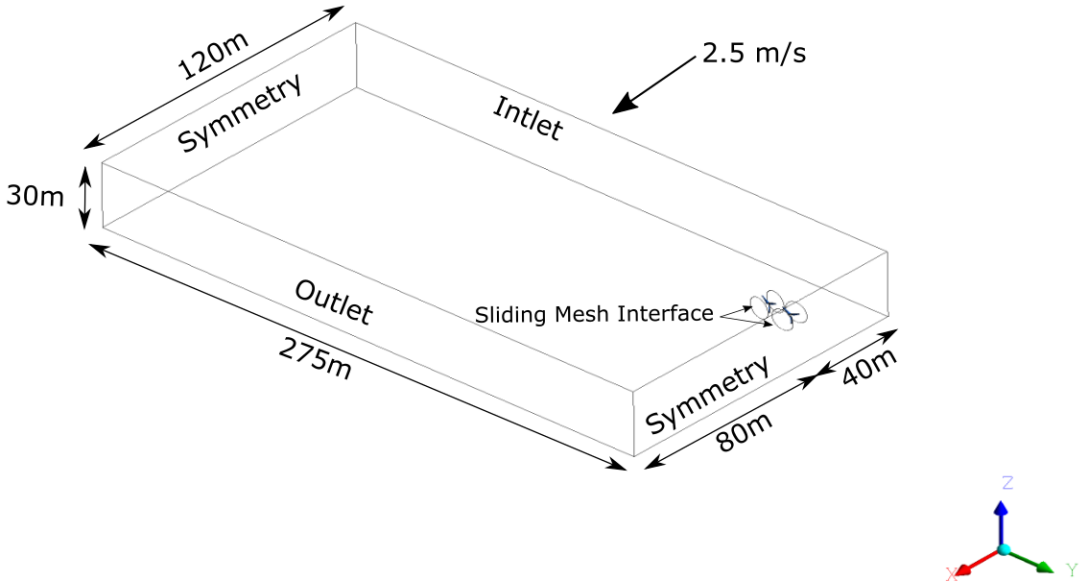

Figure 7.2: Computational domain for yawed turbine simulations with representative channel geometry based on Strangford Lough.

about the innermost position of the blade tip as shown in Figure 7.3. Two other reasonable alternative yaw definitions are also presented in Figure 7.3, yawing about a support tower and yawing about the centre of the rotor plane. While these alternative definitions are more practical for the physical implementation, the chosen method preserves the inter-turbine spacing between the inner and outer turbines, maintaining the local blockage of the inner turbine. Yawing the turbine about the tower would alter both the inter-turbine spacing and the stream-wise offset whereas yawing about the centre of the rotor plane would decrease the inter-turbine spacing with non-zero yaw. Both these methods make it difficult to isolate the effect of yaw in isolation. All turbines within the fence were operated at the same angular speed ($\omega = 2.81$ rad/s). This speed corresponded to the design $\lambda = 4.5$ for a single turbine with a u_∞ of 2.5 m/s in the same global blockage

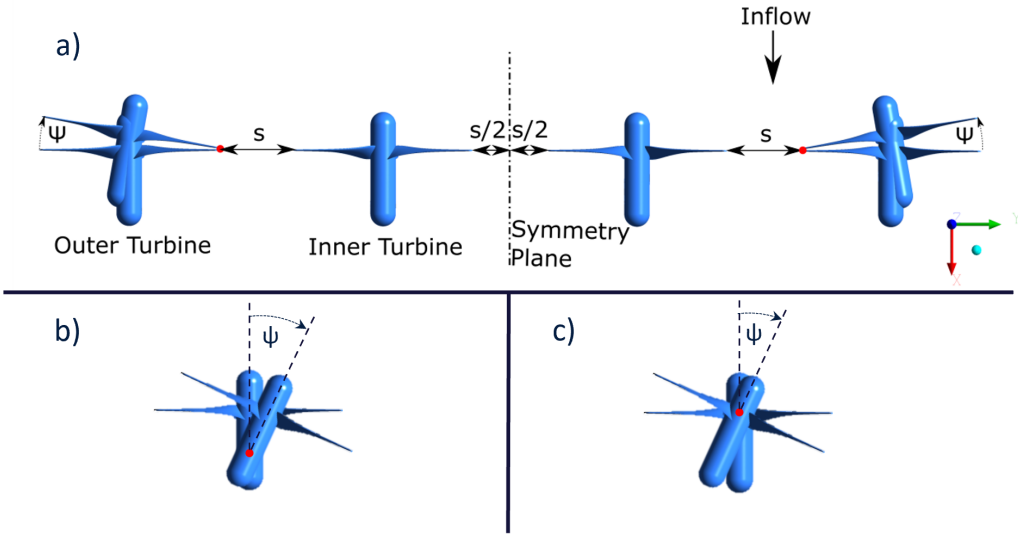

Figure 7.3: Plan view of yaw applied to the outer turbine with the inner turbines remaining unchanged. (a) is yawed about the innermost region of swept area, (b) is yawed about a support tower and (c) is yawed about the center of the rotor. Yaw angles pointing towards the centre of the fence are positive in this study.

conditions.

7.2.4 Stream-wise adjustment

Stream-wise displacement of the outer turbine was also investigated for two yaw angles, $\Psi = 0°$ and $\Psi = +2.5°$. Stream-wise offsets between -0.25D (-2 m) and 0.25D (2 m) were examined in this study to test the observations of Draper and Nishino (2014) and Hunter et al. (2015) around optimal stream-wise offsets. The study of Draper and Nishino (2014) examined two row's of turbines with the rows either staggered or aligned. Draper and Nishino (2014) suggested that the optimal layout for a fixed number of turbines is in a single plane, however, owing to the limitation of the LMADT model used in this study, only staggered turbines outside

the near-wake region were considered. Hunter et al. (2015) was able to examine staggered fences in the near-wake region using a RANS actuator disk model and showed that a small performance improvement is possible when the disk's were differentially tuned. This aspect of the study aims to provide further support for Hunter et al. (2015) results by explicitly resolving turbine geometry in the model.

7.2.5 Differential operation

The $\Psi = 0°$ and the $\Psi = 5°$ cases were further optimised by individually adjusting the rotational speeds of the turbines. To determine this operating point, the fence was first optimised for synchronised λ, then the outer and inner turbine λ were adjusted individually until the total fence power was at a maximum. This process converged within a few iterations.

7.3 Results

Excluding the differential speed controls analysis, the results presented in this parameter study are for a fixed turbine rotational speed (ω) of 2.81 rad/s corresponding to a λ of 4.5. Adjusting λ had limited influence on the turbine power coefficients and the relative difference between the inner and outer turbines, as shown in Figure 7.4. Increasing the tip speed ratio to $\lambda = 5.4$ increased fence C_p by 1.8% to $C_p = 0.542$ and fence C_t by 2.4% to 0.971 due to a higher turbine resistance being achievable through the local blockage created by the fence. Qualitatively the relationship of power and thrust between the inner and outer turbines was the same when operating at the optimal λ=5.4 condition and the sub-optimal λ=4.5.

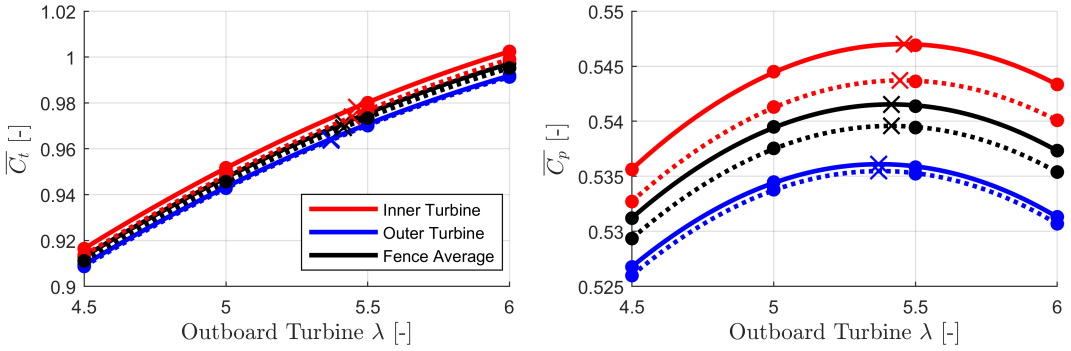

Figure 7.4: Inner (red), outer (blue) and fence-averaged (black) turbine thrust coefficient C_t (left) and power coefficient C_p (right) over a range of λ for 0° (solid) and +5° (dashed) outboard turbine yaw angles. The maximum turbine C_p is marked with crosses.

7.3.1 Non-yawed turbine flow

The performance of the four turbine fence was initially characterised for the no outer turbine yaw condition. Outer turbine $C_p = 0.529$ and $C_t = 0.909$ were both observed to be lower than the equivalent inner turbine parameters ($C_p = 0.536$, $C_t = 0.916$). The difference between them is described by the symmetry factor, Φ. Φ quantifies the balance between a parameter for the inner and outer turbines with a positive value indicating a bias towards the inner turbine. This is defined as

$$\Phi_X = \frac{X_{inner} - X_{outer}}{X_{inner}} \tag{7.1}$$

where X is a turbine metric (e.g., C_p or C_t). For the no yaw condition there was a 1.3% bias in power production towards the inner turbine ($\Phi\ C_p = 0.013$) and a 0.8% bias in thrust ($\Phi\ C_t = 0.008$).

While the differences in integrated quantities of C_p and C_t were relatively small between the inner and outer turbines, a greater disparity was observed in the blade loading. Blade root bending moments were used to quantify the loading as the

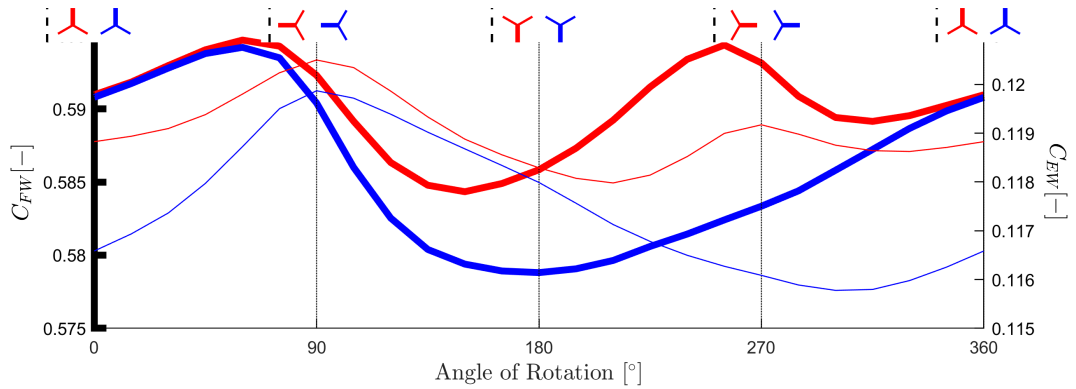

Figure 7.5: C_{FW} (bold) and C_{EW} (normal) azimuthal variation for inner (red) and outer (blue) turbines.

blade moved around the azimuth. This loading was split into two components, C_{FW} which is the root bending moment coefficient normal to the rotor plane (flapwise direction), and C_{EW}, which is the root bending moment coefficient in the plane of rotation of the turbine (edgewise direction). These coefficients were defined as

$$C_{FW} = \frac{M_{FW,i}}{\frac{1}{2}\rho u_\infty^2 A_t R} \quad C_{EW} = \frac{M_{EW,i}}{\frac{1}{2}\rho u_\infty^2 A_t R} \tag{7.2}$$

where $M_{FW,i}$ is the root bending moment of blade i in the flapwise direction and $M_{EW,i}$ is the root bending moment of blade i in the edgewise direction. Figure 7.5 plots the azimuthal variation in C_{FW} and C_{EW} for the outer and inner turbines. This plot clearly demonstrates that the amplitude of loading experienced by the outer turbine (amplitude C_{FW}=0.015) is 48.0% greater than the inner turbine (amplitude C_{FW}=0.010). The cause of this is explored in Figure 7.6 which shows that the flow angle at hub height through the turbine plane is significantly larger for the outboard side than the inboard side. This flow mis-alignment, in conjunction with the reduced mass flux through the rotor, results in a drop off in load as the

blade passes the end of the fence.

The load signal also demonstrates a once-per-revolution peak in load fluctuations for the outer turbine and a twice-per-revolution signal for the inner turbine, these peaks correspond to the blade passing an adjacent turbine. Due to the symmetry assumption, the peak for the inner turbine's root bending moment at 90° corresponds to the blade passing a counter rotating turbine, qualitatively, this is similar to the peak at 270° where the blade passes a co-rotating turbine. Given this observation, results presented here can be considered indicative of a fence of four turbines all spinning in the same direction.

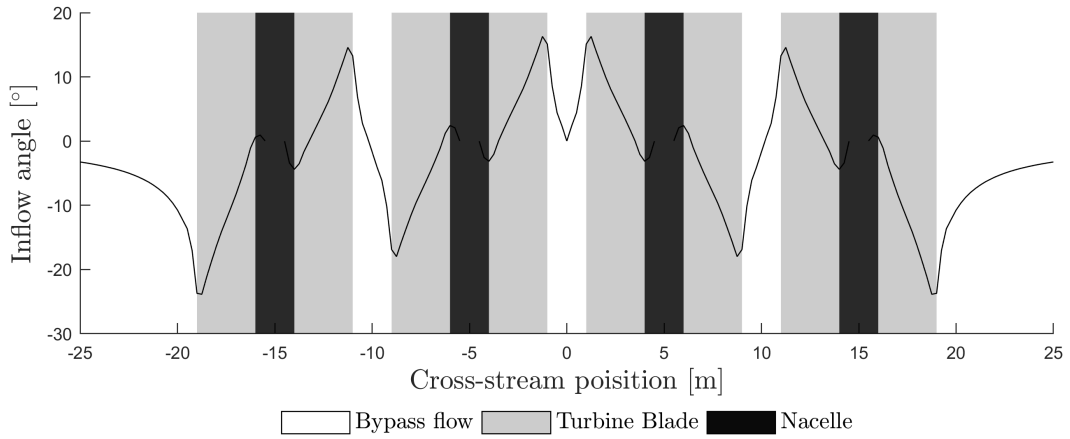

Figure 7.6: Flow approach angle relative to the turbine plane at hub height along the fence, 0° is normal to the turbine plane. The grey area marks the portion of the transect where the turbine blade sweeps through and the black area is the location of the nacelle.

7.3.2 Impact of outboard turbine yaw on performance

The C_p, C_t and volume flux (Q) (averaged over a complete rotation) are presented in Figure 7.7 for varied outer turbine yaw angles. The fence average for all three quantities are maximised when the outer turbine yaw angle is 0°. The outer turbine

produces maximum power when it is yawed inwards by +2.5°, but this coincides with a decrease in inner turbine performance, resulting in an overall reduction in fence power. An approximately linear decrease in the inner turbine performance was observed as the outer turbine yaw angle increased. This result highlights an interaction between the turbine performance and the constraint on the bypass flow between inner and outer turbines. Figure 7.8 plots the velocity contours and streamlines at the hub height over half the turbine fence and Figure 7.9 plots the inflow angle and velocity normal to the turbines at hub height. At negative outer turbine yaw angles a subtle increase in velocity across the entire inner rotor is observed, leading to a increase in power. The increased velocity is sustained by the outer turbine imposing greater confinement on near wake expansion at negative yaw angles.

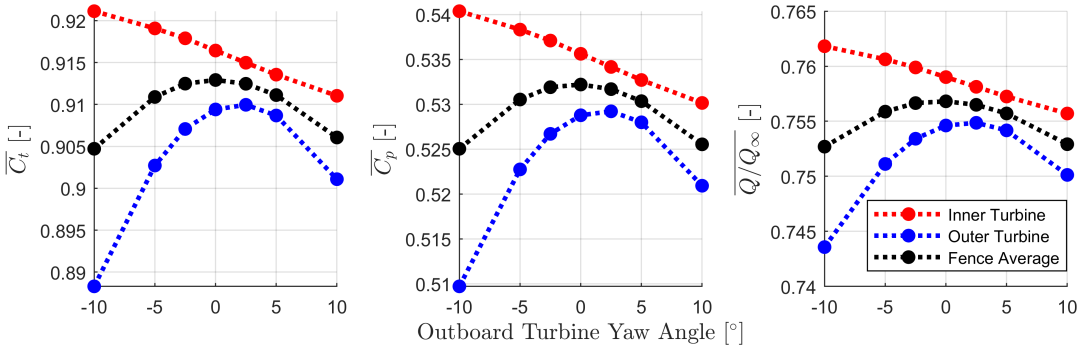

Figure 7.7: Turbine thrust coefficient C_t (left), power coefficient C_p (middle) and normalised volume flux $\overline{Q/Q_\infty}$ (right), for inner (red) and outer (blue) turbines at varied yaw angles. The fence average is plotted in black.

For the outer turbine, the volume flux through the turbine appears to be proportional to the cosine of the yaw angle (as is the swept area normal to the free stream flow). A slight angular offset to this relation is observed with outboard turbine performance optimised at a yaw angle of +2.5°. The inflow alignment

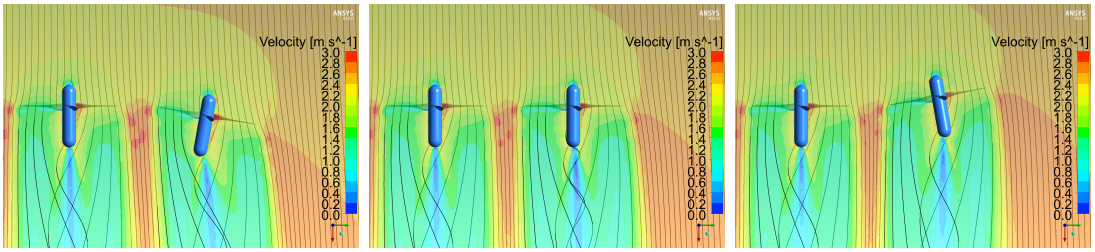

Figure 7.8: Velocity streamlines at hub-height for half of a four turbine fence. The inner turbine is on the left and the outer turbine is on the right. The outer turbine yaw alignment has been adjusted by -10° (left), 0° (middle) and +10° (right).

correction can be observed in Figure 7.8 on the outer turbine for the +10° yaw case. In this plot, the inflow angle passing the outer portion of the turbine is close to orthogonal to the blade; correcting for the misalignment observed in the 0° yaw case. Despite the correction over the outer portion of the rotation, the inner region is made worse at higher yaw angles, so too is the velocity normal to the rotor. Figure 7.9 plots the approach angle (averaged at hub height over a rotation) alongside the normal component of velocity to the turbine. A decrease in inflow angle magnitude is observed as the yaw is increased, with the largest yaw angle (+10°) producing between 5° to -10° misalignment over the outer portion of the blade relative to the no yaw case which had between 2° and -22°.

The integrated quantities presented in Figure 7.7 arise due to the combined effect of all the blades through a rotation, however due to the asymmetric flow an individual blade's contribution varies with azimuthal position. Figure 7.10 plots this variation with different outboard turbine yaw angles. Also important to the blade loading of yawed turbines is the direction of rotation. Changing the spin direction causes a 180° phase shift of the loading from the blade advancing and retreating effect. To decouple this effect Figure 7.10 includes the azimuthal variation of individual blade C_p for co-rotating, counter-rotating (outer turbine spin

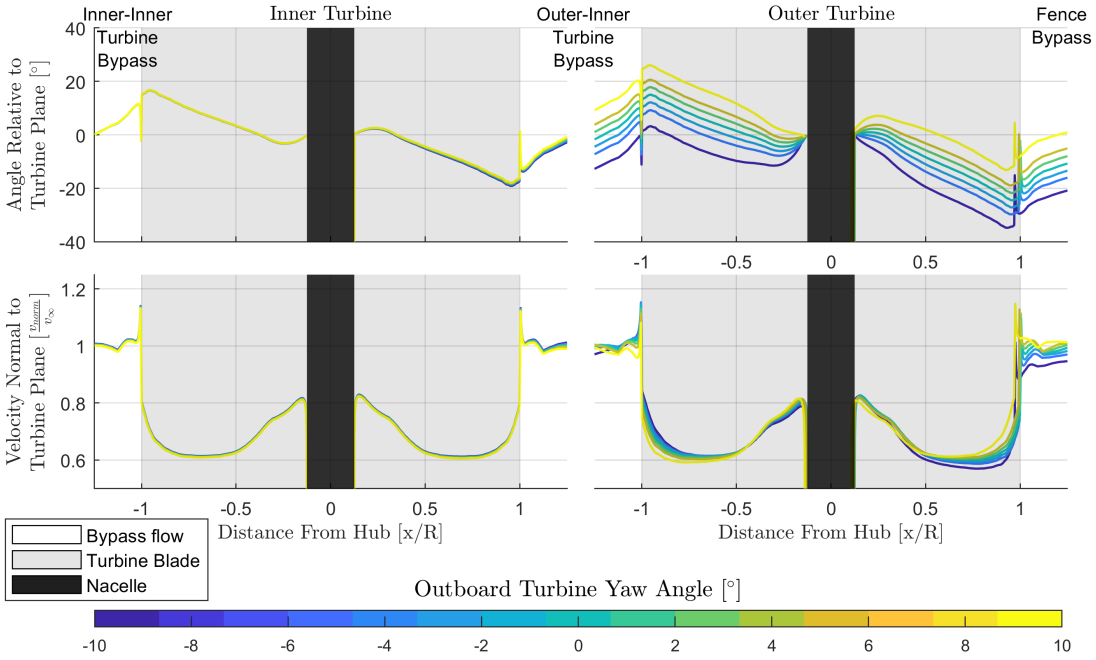

Figure 7.9: Transect of turbine inflow angle (top) and inflow velocity (bottom) at rotor hub height for the inner (left) and outer (right) turbines. Inflow angle and velocity are determine relative to the turbine plane as it yaws. Data has been averaged over a complete turbine rotation.

direction reversed), and the average over both directions. This plot demonstrates that much of the azimuthal variation in blade performance results from the turbine blade advancing and retreating. As the rotation is reversed the blade advancing and retreating load is offset by 180°; the super position of this loading with the confinement loads (passing the adjacent turbine's blades) results in a 90° shift in the peak load when the turbine spin direction is reversed. Averaging over the co-rotating and counter-rotating outer turbine results demonstrates two regions where flow properties are, on average, enhanced. The first is with a yaw angle of -5° as the outer turbine blade passes the inner turbine (θ=90°). At this azimuthal position, the constructive interference between the turbines is at a maximum due to the distance between adjacent blades being a minimum and the negative yaw

angle imposes an additional lateral constraint on the inner turbine. The secondary peak observed in the plot occurs at the +10° yaw angle over the outermost portion of the fence (θ=270°). This localised improvement is primarily associated with flow realignment around the fence, as mentioned above and observed in Figure 7.8.

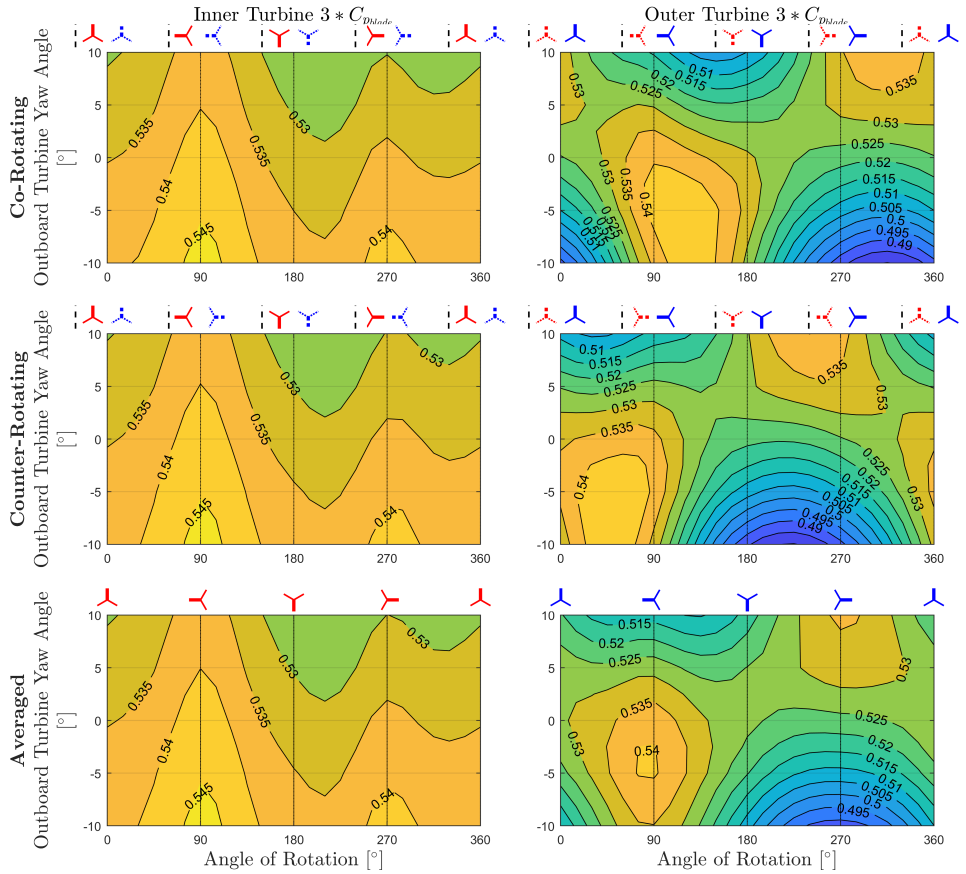

Figure 7.10: Inner (left column) and outer (right column) turbine C_p variation with angular position for varied turbine yaw angles. The top row corresponds to co-rotating inner and outer turbines, the middle to counter-rotating inner and outer turbines, and the bottom is the average of the rotation directions. The inner turbine always rotates in the anticlockwise direction.

The two regions of improvement highlight the balance between optimising the flow alignment relative to the outer turbine and increasing flow confinement, these

effects are optimised at different yaw angles and azimuthal positions for the individual blade. Given that multiple blades experience this loading (albeit with a phase offset), the maximum rotor power is achieved at an outer turbine yaw angle somewhere between the positions which optimise the two regions of enhanced performance (Ψ=+2.5°). This optimum yaw angle also corresponds to minimising the variation in the power production over a rotation.

The differences between co-rotating and counter-rotating turbines had little influence on the integrated performance of the fence. Furthermore no significant impact on the inner turbine blade loading was observed when the direction of rotation of the outer turbine was changed. This supports the assertion presented in Section 7.3.1 that results from modelling two turbines with a symmetry plane are indicative of a fence of four turbines all spinning in the same direction.

7.3.3 Impact of outboard turbine yaw on loading

Figure 7.11 shows the flapwise (C_{FW}) and edgewise (C_{EW}) root bending moments coefficients. The C_{EW} plot supports the observation made in Section 7.3.2 that the variation in power production throughout a rotation is minimised at $\Psi = +2.5°$ (given $P \propto \sum_{i=1}^{3} M_{EW,i} * \omega$). A similar trend is also observed in the flapwise direction for the same yaw position. The outboard turbine loading in both flapwise and edgewise directions is smaller in amplitude than the inboard turbine for $\Psi = +2.5°$, in addition, at this yaw angle the outer turbine bending moment amplitude is smaller than both inner and outer turbines for the $\Psi = 0°$ case. This is of practical relevance to turbine manufacturers as it influences blade fatigue estimates. At the $\Psi = +2.5°$ position, the outer turbine loading amplitude in the

flapwise direction is 0.008 (47.4% reduction from $\Psi = 0°$), this is similar to the inner turbine (0.010) and corresponds to the point that minimises the variance due to the combined effects of blade advancing and retreating and flow alignment.

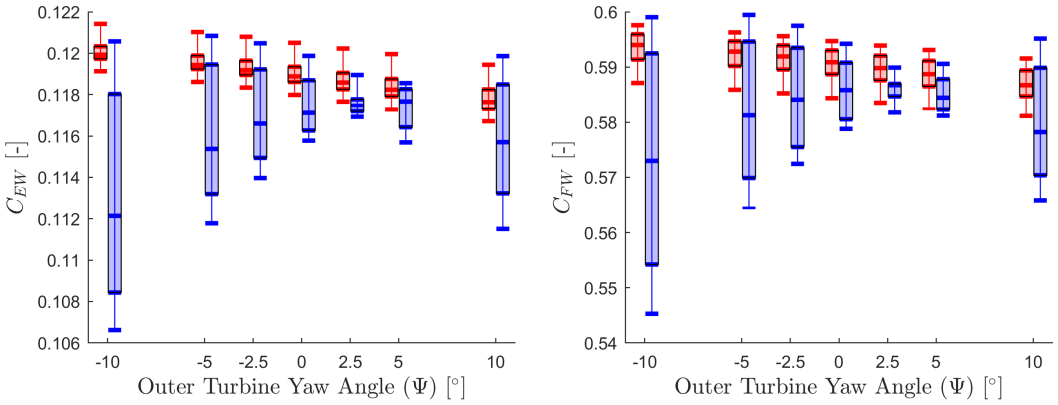

Figure 7.11: Box and whisker plots of C_{EW} (left) and C_{FW} (right) for inner (red) and outer (blue) turbines for varied outboard turbine yaw angles.

The azimuthal variation in C_{EW} and C_{FW} is plotted in Figure 7.12. Concentric profiles of both C_{EW} and C_{FW} for the inner turbine indicate a uniform increase in loading around the azimuth, consistent with increasing the mass flux over the entire turbine. The outer turbine experiences more significant changes in loading from being yawed due to blade advancing and retreating effects. This is demonstrated by the ~180° phase shift in C_{EW} and C_{FW} peaks between the co-rotating and counter-rotating turbines as the higher relative blade speed shift peaks from inboard to outboard of the fence.

Figure 7.13 plots the axial and tangential force distribution per unit span along a blade from the outer turbine as it passes the inner-outer turbine bypass (θ=90°) and the fence bypass (θ=270°). This plot shows an impact on both the axial and tangential force distribution (F_x and F_θ), with the highest impact of yaw being localised around the final quarter of the blade. The pressure distribution at the

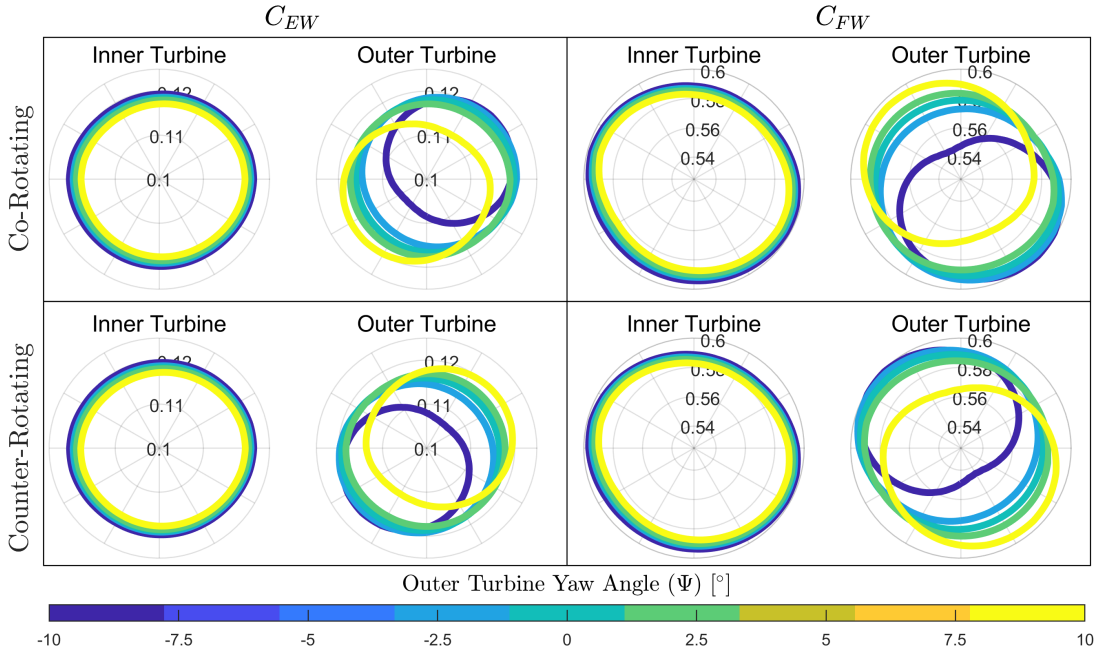

Figure 7.12: Azimuthal variation in C_{EW} (left) and C_{FW} (right) for co-rotating (top), counter-rotating (bottom). Inner and outer turbines are plotted as if viewing from front on.

85% radius position ($r = 0.85R$), also presented in Figure 7.13, shows that the change in blade force is associated with an uplift in static pressure around the entire section. Most notably, there is an increase in suction on the suction surface towards the peak (near the leading edge) however, there is also a small pressure rise over the pressure surface.

Figure 7.14 plots the suction surface towards the tip of a blade on the outboard turbine. This plot demonstrates that the greatest improvement in suction peak is achieved for the outboard passage (θ=270°) for $\Psi = +10°$, whereas there is a decrease in the suction peak when $\Psi = -10°$ over the same region. This is intuitive when comparing to the inflow and alignment plot (Figure 7.9) as there is a higher flow speed and improved alignment over the outboard region when the

turbine is yawed by $\Psi = +10°$. The azimuthal position of the higher suction also correspond to the regions of greater torque observed in Figure 7.12. At locations around θ=90° and θ=270° the blade advancing and retreating effect is small due to the relative motion of the blade transitioning from advancing to retreating. This leads to a change in pressure over the blade surface as a result of the change in velocity, the magnitude of this effect is reversed between positive and negative yaw cases.

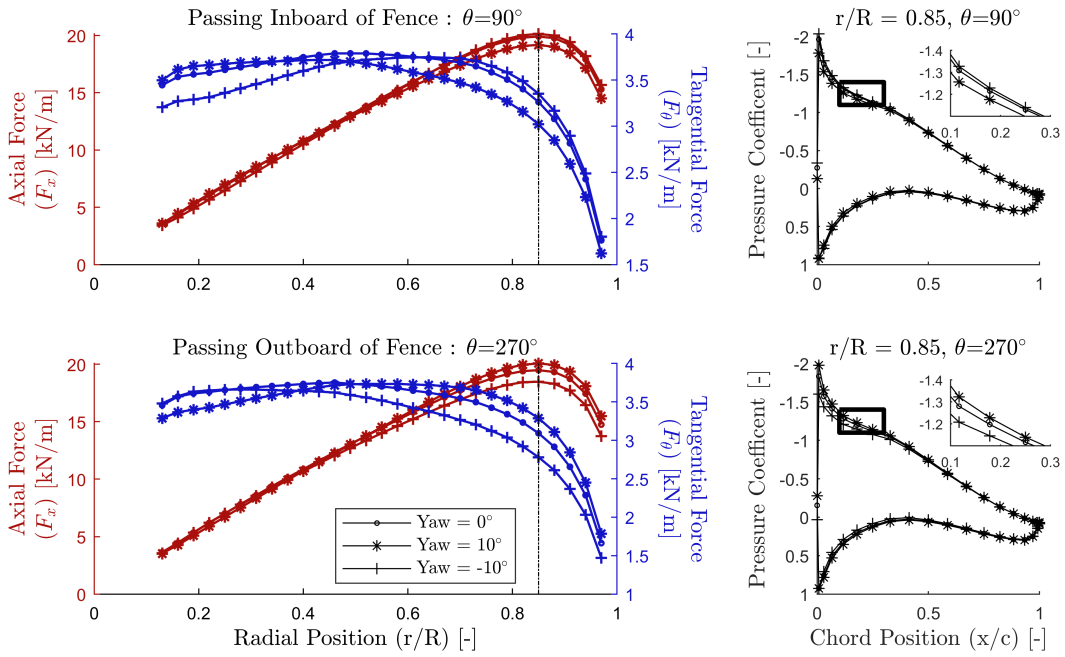

Figure 7.13: Turbine normal, F_x, (red) and turbine plane ,F_θ, (left) force distribution and blade pressure distributions at r/R=0.85 (right) for a blade on the outer turbine passing inboard (top) and outboard (bottom) of the fence. Results are presented for the co-rotating turbines.

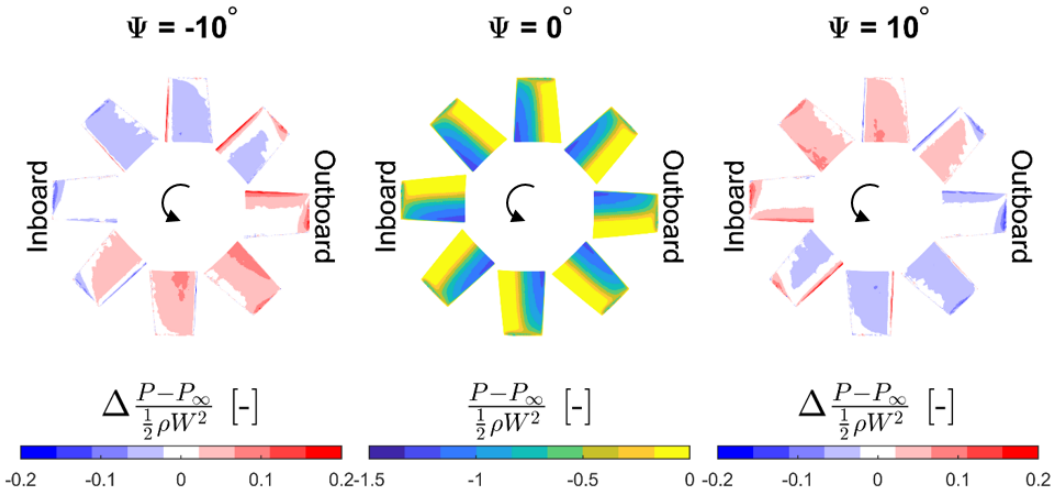

Figure 7.14: Static pressure coefficient on the blade suction surface over the tip region (0.85R-1R) every 45° indicated by the blade plot angle for $\Psi = -10°$ (left), $\Psi = 0°$ (middle) and $\Psi = +10°$ (right). The $\Psi = -10°$ and $\Psi = +10°$ are plotted as the difference from the $\Psi = 0°$ case.

7.3.4 Differential operation of yawed turbines

Allowing variable speed operation of the turbines permits additional power extraction from the fence as each turbine can be optimised for the specific flow conditions and constructive turbine-turbine interaction effects. Figure 7.15 shows that individually, the outer turbine achieves more power when the rotational speed is reduced from $\lambda = 5.41$ (which is the optimal λ for synchronised controls) to $\lambda = 5.25$ due to the lower inflow velocity resulting from the fence end-losses. However, the speed reduction of the outer turbine required to maximise overall fence power is less due to the lateral flow confinement it provides to the inner turbine. The optimal fence power is achieved when the outer turbine operates at $\lambda = 5.36$. This result is within 0.2% for both the yaw cases tested ($\Psi = 0°$ and $\Psi = +5°$). The figure also shows that spinning the outer turbine faster enhances the inner turbine C_p as a linear function of the outer turbine λ and reduces the outer turbine C_p

proportional to λ^2 over the range tested.

Comparing between the $\Psi = 0°$ and $\Psi = +5°$ simulations, the impact of yawing the outer turbine reduces performance, especially for the inner turbine. The physical intuition for this phenomenon is similar to that presented in the yaw adjustment section, where increased yaw removed the lateral constraint on the inner turbine. In this case, yaw angles are fixed, and a lateral constraint is imposed by increasing the outer turbine λ. This action is dampened when the turbine is in a yawed position leading to slightly less power in those cases.

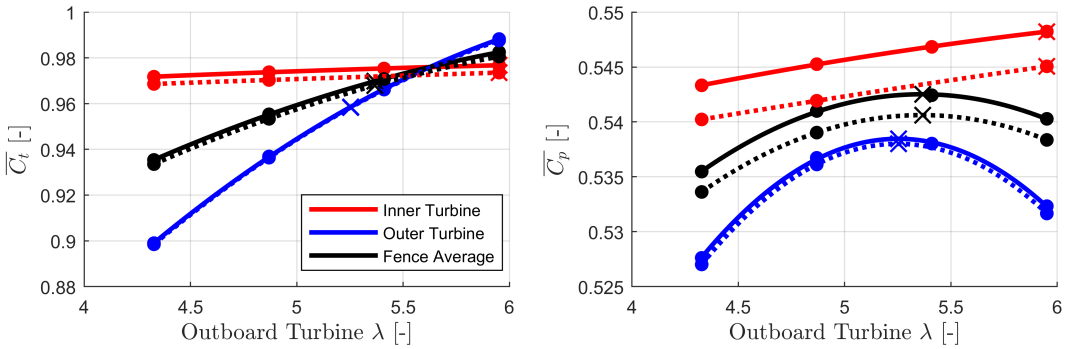

Figure 7.15: Inner (red), outer (blue) and fence averaged (black) turbine C_t (left) and C_p (right) over a range of outboard turbine λ with a fixed inboard turbine λ of 5.41 for Ψ=0° (solid) and Ψ=5° (dashed). The maximum turbine C_p is marked with crosses.

The surfaces in Figure 7.17 are the output of the differential speed operation optimisation process. Average fence C_p and C_t have been scaled to show the percentage improvement relative to the optimal synchronised operation case of the $\Psi = 0°$ fence, C_p^* and C_t^*.

Two differential speed control methods were investigated in this study. The first (strategy 1) was focused on optimising the total turbine power and was determined through a progressive iteration of inner and outer turbine λ. The second strategy

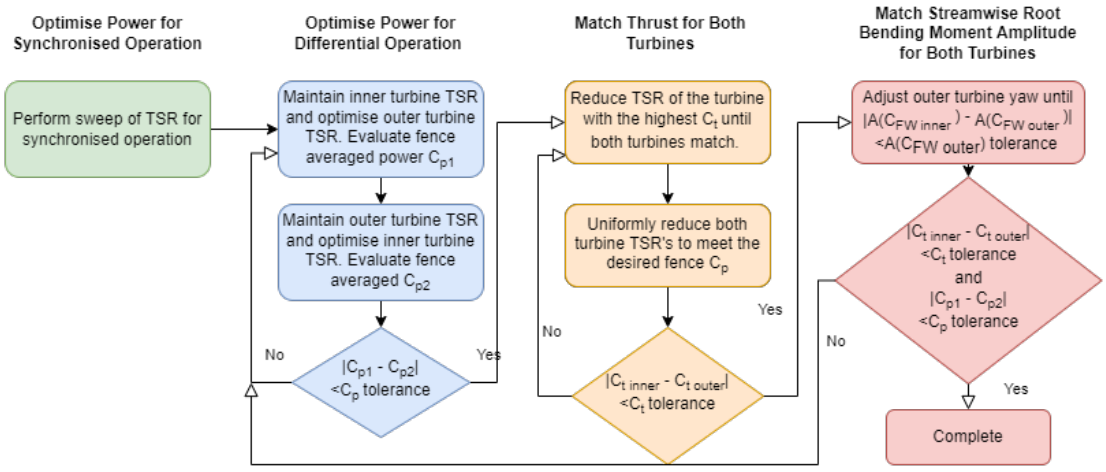

Figure 7.16: Strategy to match thrust and blade load amplitude on a 4 turbine fence.

(strategy 2) is presented in Figure 7.16, focusing on the trade off between total power generation and turbine loading. Through this process average turbine C_p and C_t were matched between the inner and outer turbines. An additional degree of freedom is introduced by allowing the outer turbine to yaw. This makes it possible to also balance the amplitude of the blade root bending moments between the inner and outer rotors, ensuring that turbines experienced closely matched loading conditions.

The black cross (strategy 1) in Figure 7.17 shows that there is a combination of turbine λ for which fence performance is marginally improved (<0.25%) above the synchronised control case. The green star (strategy 2) shows a combination of inner and outer turbine λ which reduces the overall azimuthally-averaged thrust on the system and balances the azimuthally-averaged loading between the inner and outer turbine.

By operating the outer turbine at $\lambda = 5.21$ and the inner turbine at $\lambda = 5.07$, the two rotors have the same azimuthally-averaged thrust coefficient and the added

benefit of a reduction in the total thrust on the system of 1.5%. There is still a 1.5% bias in power production towards the inner turbine. From a blade loading perspective this is of less concern as the edgewise bending moments are significantly smaller than the flapwise bending moments. The amplitude of the flapwise root bending moment for the outer turbine is close to unchanged under this operation strategy, being close to double that of the inboard turbine ($\Phi C_{FW}\,Amplitude = 0.5$).

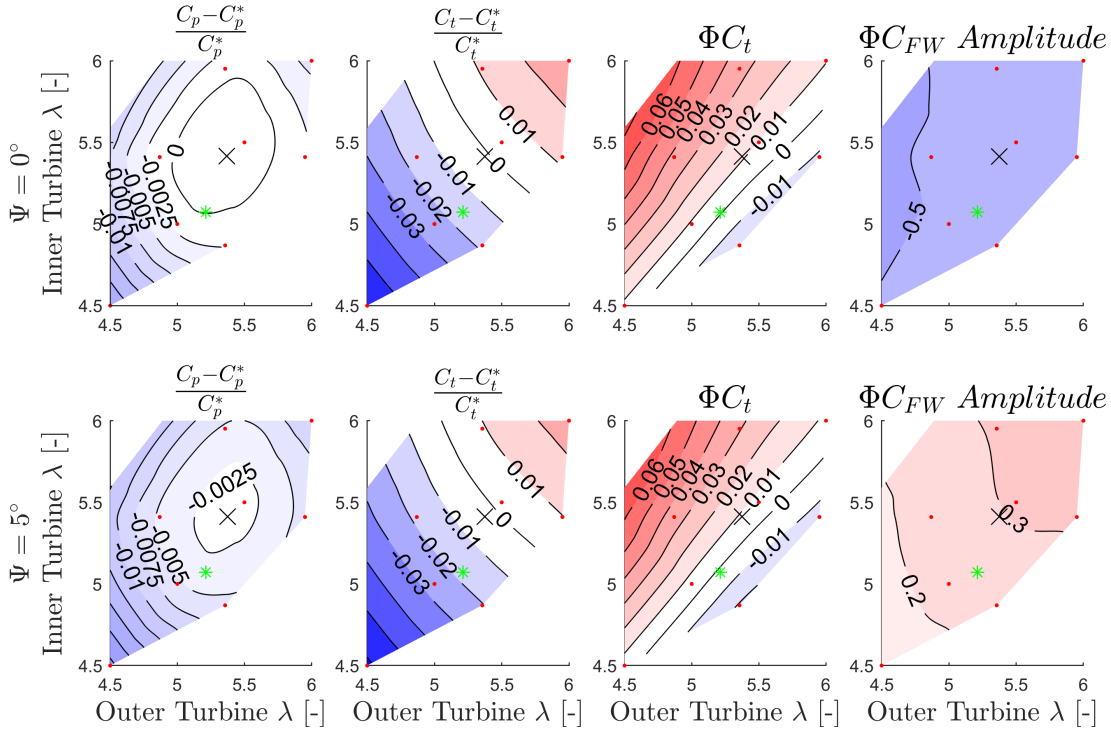

Figure 7.17: Averaged turbine fence C_p (left), C_t (centre-left), ΦC_p (centre-right) and ΦC_{FW} Amplitude (right) with differential operation for $\Psi = 0°$ (top) and $\Psi = +5°$ (bottom). C_p and C_t have been scaled by their respective values for the optimal operating condition with synchronised controls for $\Psi = 0°$ (C_p^* and C_t^*). Red circles indicate the data points the contours were interpolated from and the black cross is the operating condition which produces the maximum power. The green star is the operating point for the operating strategy presented in Figure 7.16

Table 7.1: Comparison between differential operation strategies with a 5% outer turbine yaw

	Inner Turbine			Outer Turbine		
	C_p	C_t	C_{FW} *Amplitude*	C_p	C_t	C_{FW} *Amplitude*
Strategy 1	0.543	0.972	2.251E-03	0.538	0.964	1.586E-03
Strategy 2	0.543	0.953	2.221E-03	0.537	0.953	1.637E-03
Difference (%)	-0.2%	-2.0%	-1.3%	-0.1%	-1.1%	3.2%

Using the same operating point but yawing the outboard turbine by 5° reduces the amplitude of C_{FW} for the outer turbine by 49%, less than inboard turbine (positive ΦC_{FW} amplitude) in Figure 7.17). This comes at the cost of a $< 0.4\%$ reduction in fence power but it is advantageous as both the load magnitude and amplitude are closer to uniform along the fence. Further optimisation of yaw over the range of $0° < \Psi < +5°$ is expected to equalise both the azimuthally averaged thrust and the flapwise blade root bending moment amplitude. This effectively ensures that the same loading conditions are experienced by both turbines.

A comparison between the two strategies operating with a 5% outer turbine yaw is made in Table 7.1. This table demonstrates how strategy 2 makes a small sacrifice in turbine power (reduction of less than 0.2%) to reduce the thrust experienced by the turbines (reduction of more than 1.1%). A slight increase is observed in the outer turbine C_{FW} *Amplitude* relative to strategy 1, however outer turbine C_{FW} *Amplitude* is less than inner turbine C_{FW} *Amplitude* for both strategies. Further iterations of strategy 2 would result in the yaw angle decreasing and outer turbine C_{FW} *Amplitude* increasing to match that of the inner turbine.

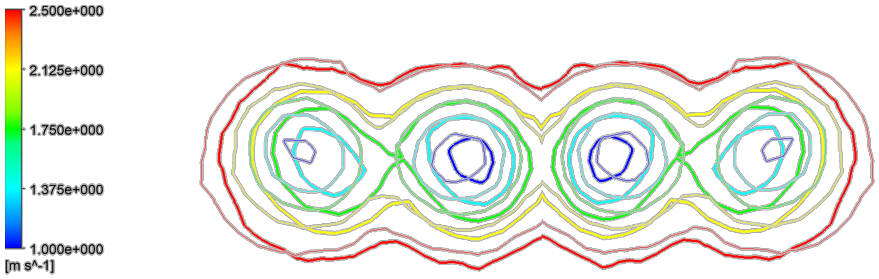

Figure 7.18: Velocity magnitude contours $4D$ downstream of the turbine fence for 0° outboard turbine yaw (thin lines) and +10° outboard turbine yaw (thick lines).

7.3.5 Wake deflection

Deflection of the outer turbines wake as a result of turbine yaw was observed in this study. As the turbine is yawed towards the centre of the fence, so too was the wake. Figure 7.18 shows the difference in the wake shape between the Ψ=0° and Ψ=+10° cases $4D$ downstream of the turbine plane. This figure highlights a smaller wake width as flow progresses away from the rotor plane.

Wake deflection may be a useful tool in larger scale tidal turbines farms to optimise total farm energy output. Wake steering has been shown to improve energy production in wind farms by diverting wakes away from downstream turbines (Archer and Vasel-Be-Hagh, 2019). Similar methods using these controls may also provide benefit to tidal farms. The tidal application of these controls is slightly different from wind, which employs dynamic yaw controls to steer wakes from downstream turbines. The process needs to be dynamic in wind to adjust for the varying flow directions. For the tidal application, the predominate flow direction is known due to the periodic nature of the tides. In this case, yaw controls to reduced the wake width behind short turbine fences as shown in Figure 7.18 may allow a higher packing density of tidal turbines.

7.3.6 Stream-wise offset

C_p, C_t and Q averaged over a complete rotation are plotted in Figure 7.19. This plot demonstrates that for a positive stream-wise offset (outer turbine advances into the flow), there is a decrease in outer turbine performance. This corresponded with an approximately equal (over the range of offsets tested) increase in inner turbine performance, having an overall neutral impact on fence power production. Examining the outer-inner turbine bypass region in Figure 7.20 provides an insight to the physical process responsible for this observation. As the outer turbine advances into the flow, the lateral constraint on the inboard side is reduced. This leads to a reduction in mass flux through the turbine (Figure 7.19) and an increased bypass flow which is diverted towards the adjacent turbine. Because of this, mass flux through the system is close to constant. This phenomenon is an artefact of the turbine stagger being smaller than the length required for pressure recovery. Were the stream-wise offset much larger, performance of the outer turbine is expected to decay to that of a single turbine the inner turbines to that of a two turbine fence. This result expands on those of Draper and Nishino (2014) and Hunter et al. (2015), suggesting that some small stagger is acceptable within a turbine farm when targeting optimal power.

Figure 7.21 plots the C_p contribution of a blade around the azimuth of a turbine with varied outer turbine stream-wise offsets. This plot shows how the change in flow, observed in Figure 7.20, translates to a change in power. The outboard region of the inner turbine (θ=270°) and the inner region of the outer turbine (θ=90°) experience opposite trends with changing stream-wise offsets; the outer turbine increasing as the inner turbine decreases. This results in approximately

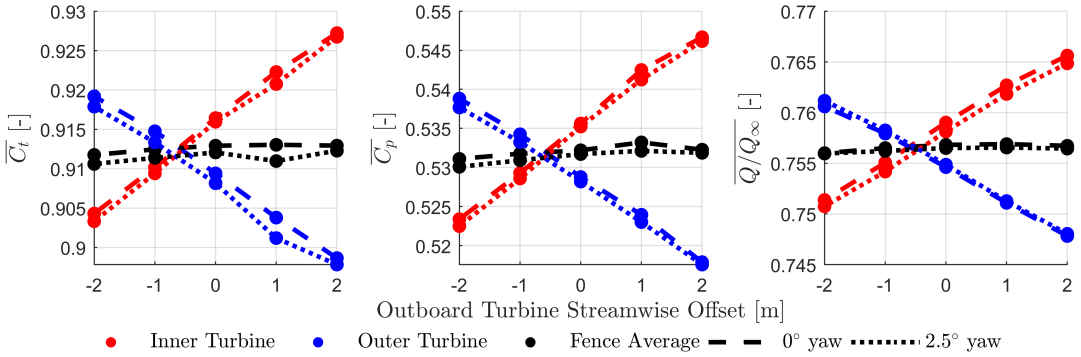

Figure 7.19: Turbine thrust coefficient C_t (left), power coefficient C_p (middle) and normalised volume flux $\overline{Q/Q_\infty}$ (right), for inner (red) and outer (blue) turbines at varied outer turbine stream-wise offsets. The fence average is plotted in black, the no turbine yaw case is plotted with dashed lines and 2.5° yaw case is with a dotted line.

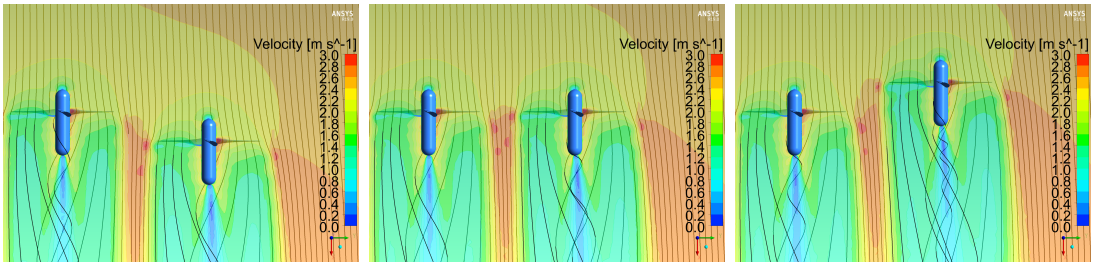

Figure 7.20: Velocity streamlines at hub-height for half of a four turbine fence. The inner turbine is on the left and the outer turbine is on the right. The outer turbine yaw offset has been adjusted by -2 m (left), 0 m (middle) and +2 m (right).

constant total fence power. Given this result, it may appear that a slight negative offset is beneficial to match the C_t or C_p of the outer and inner turbines without a sacrifice on turbine power. However this adjustment impacts flow conditions primarily around the inner-outer turbine bypass (as shown by the outer turbine power production in Figure 7.21) and increases the unsteady loading on the system.

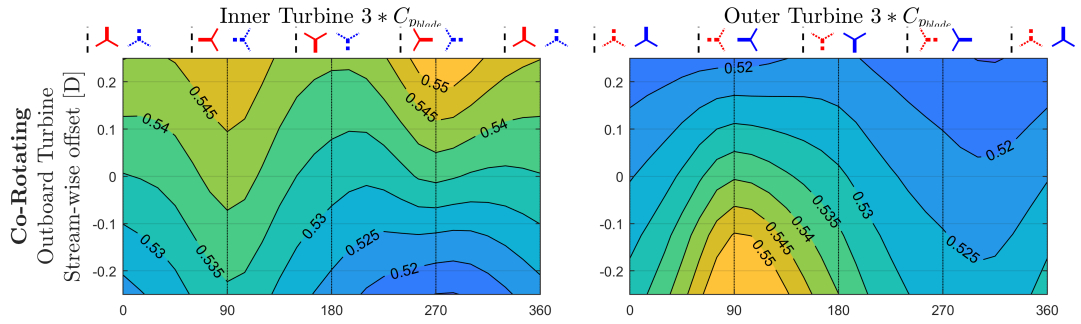

Figure 7.21: Inner (left) and outer (right) turbine C_p variation with angular position for varied outer turbine stream-wise offsets.

7.4 Model limitations

This study employed an unsteady RANS model with a sliding mesh to resolve the rotation of a turbine within a fixed domain. The model has been useful to characterise the flow physics associated with the yawing of an outboard turbine within a fence; however, some key physics have been removed to facilitate a quick simulation. Notably, flow conditions have been simplified to allow the impact of outer turbine yaw to be isolated. Surface deformation, flow profiles and waves all impact the turbine loading and power production which may be influenced by yaw. Non-uniform flow in each axis will impact the individual turbine loading characteristics and the variation of the flow conditions along the length of the fence with interfere with how the turbines interact. Furthermore, the turbine towers have not been included in this study; the tower has been observed in experiments to reduce blade loading as it passes the tower Bahaj et al. (2007). This effect is typically small; however, the physics of the problem changes when the turbine is yawed, and the downstream projection of the turbine on the tower is reduced.

The choice to analyse the outer turbine yawing about the inner-most point of

the turbine swept area was an effective means to isolate the impact of yaw on the turbine fence separate to local blockage and stream-wise displacement. However, the practical implementation would likely require the turbine to rotate around the tower, located at an offset downstream of the turbine plane. A preliminary set of simulations with the turbine yawing around a tower has produced qualitatively similar results. Further simulation is required to determine the combined effect of varying the inter-turbine spacing and outer turbine yaw angle when the outer turbine is yawed about a fixed tower.

Due to computational constraints, only a single yaw angle was investigated for differential operation; defining the optima requires significant iterations and model runs, making it impractical to consider a range of outer turbine yaw angles. For the $\Psi = 5°$ case, which was optimised for differential controls, the resulting operating condition was similar to that of the $\Psi = 0°$ suggesting only a small variation in yaw angle is required to tune the differential controls; further simulation is required to verify this hypothesis. This physical reason is that small yaw angles do not significantly impact the inflow (inflow is proportional to the cosine of the yaw), and the leading order effect from the yaw is blade advancing and retreating which quickly increases when outside of the optimal alignment conditions.

7.5 Conclusions

This study has analysed the impact of yaw controls on the outermost turbines of a four turbine fence operating in blockage conditions representative of Strangford Lough. It has been demonstrated that a small adjustment in the outboard turbine yaw angle towards the fence centre results in a performance improvement for that

turbine. However, this comes at the cost of reduced flow confinement around, and hence performance of, the inboard turbines.

Both co-rotating and counter-rotating turbines operating with synchronised controls were analysed in this study. While the direction of rotation was not observed to influence power output, it did significantly influence the azimuthal variation in outer turbine blade loading due to the advancing and retreating blade effect. Averaging over co-rotating and counter-rotating simulations allowed the blade advancing and retreating effect to be controlled for and highlighted the two factors influencing performance within the fence with the outer turbine yawed. These were confinement of the bypass flow between the inner and outer turbines and improved alignment of the incident flow for the outer turbine. The former was optimised for the inner turbine at $\Psi > -10°$ and the latter was optimised for the outer turbine at $\Psi = +2.5°$. Given the balance of the two effects, the optimal arrangement for power generation when the rotors are performing with synchronised controls was $\Psi = 0°$. Despite this result, yaw was effective in reducing the amplitude of loading of the outer turbine, with a yaw angle of $+2.5°$ reducing the C_{FW} amplitude by 47.5% (from 48% greater than the inner turbines amplitude to 22% less). At this yaw angle, the influence of the blade advancing and retreating effect was minimised; this is advantageous for fatigue and maintenance planning as load cycles on the inner and outer turbines can be treated as equivalent.

Differential turbine speed operation was also investigated in this study. While it was found that no significant improvements in power were realised by operating the turbines at different speeds, an operating point was identified for the $\Psi = 0°$ case which produced the same power as the optimal synchronised turbine operation case, reduced fence C_t by 1.5% and balanced the thrust between the inboard and

outboard turbines. A similar operating condition was found for the $\Psi = +5^{\circ}$ case; however, this configuration produced 0.4% less power than the $\Psi = 0^{\circ}$ layout. Despite this, the configuration may be preferable as the variation in outboard turbine loading was halved.

Chapter 8

Conclusions and future work

Section 8.1 summarises the conclusions made in this thesis, primarily from the analysis in Chapters 4, 5, 6 and 7. Suggestions for future work are made in Section 8.2 and a summary of the contribution of this work in the tidal stream energy research space is made in 8.3.

8.1 Conclusions

Methods to improve turbine performance by reducing turbine fence end-losses have been investigated in this thesis. End-losses are a reduction in power and an increase in unsteady blade loading for the outer turbines within a fence due to anisotropic blockage conditions (flow expansion constraint from adjacent turbine on the inboard side, no constraint on the outboard side). This loss, and potential mitigation methods have been examined in this thesis for short turbine fences.

The work presented in this thesis has discussed the impact of lateral confinement on short tidal turbine fences through both a physical barrier (end-wall) and

turbine fence controls (yaw). Both of these methodologies act to reduce the flow component in the cross-stream direction.

End-losses were investigated using a RANS-BE model with gradually decreasing inter-turbine spacing. As expected greater end-losses were observed under higher local blockage conditions. Greater power can theoretically be produced by closely-spaced tidal turbines, and it is more likely to be preferred by manufacturers as a closer packed fence has the potential to reduce device costs. For this reason, the minimum practical spacing of $s = 0.25D$ was used in this study for the investigation of end-loss mitigation strategies.

8.1.1 End-wall

Both numerical and experimental investigations of a turbine fence end-wall were conducted. The end-wall geometry was designed using a parametric design process which added camber and thickness to an elliptical cross-section. RANS-BE modelling suggested that the best performing geometry gave a 3.95% improvement in turbine fence C_p and a modest reduction in C_t (0.67%) due to the reduced λ^* the turbine operated at when accompanied by the end-wall. The introduction of additional infrastructure reduced the overall efficiency with which power was extracted (basin efficiency) due to parasitic drag from the end-wall (0.9% reduction). Given the improvement in C_p further analysis was carried out with physical experimentation in a towing tank facility.

Towing tank test were conducted at SSPA in Gothenburg, Sweden using two 1.2 m diameter turbines close to the side of the tank which acted as a symmetry plane to emulate a fence of four rotors. The turbine fence end-wall, shaped out

of marine grade plywood using a CNC router to match the geometry from the numerical study, was placed at half the inter-turbine spacing (0.125D) away from the end of the fence. The results from the experiment did not show as strong support for the use of an end-wall as the numerical model with a 1.5% improvement in outboard turbine C_p (5.6% in numerical study) and a 0.8% decrease in inboard turbine performance (2.4% increase in the numerical study). The cause for this discrepancy was due to the limitations of both the experiment and RANS-BE models. The noisy data in the experiment made it difficult to determine the optimal turbine operating point and the use of the tank sidewall was not a perfect symmetry plane. This is due to a speed differential between the sidewall and water which occurs as a result of the thrust from the turbines and leads to the formation of a boundary layer. Nevertheless the end-wall was shown to improve the overall fence power and reduce the amplitude of root bending moment loads on turbine blades. It was also suggested that the use of an end-wall may have an additional purpose as a buoyancy aid for floating devices.

8.1.2 Turbine design

Comparing experimental and RANS-BE results of the four turbine fence demonstrated some limitations in model accuracy when analysing closely-spaced turbine fences. Predictions of turbine power and thrust were up to 21.3% and 6.1% off respectively, when compared to experimental data. The cause of this is, in part, due to the cross-stream forces which help to squeeze and accelerate bypass flow between closely spaced turbines. The RANS-BE formulation assumes azimuthal flow symmetry over the rotor swept area and no radial flow components; assump-

tions which are not met within a closely spaced turbine fence. Consequentially a higher order model is required with less restrictive assumptions to further analyse closely spaced turbines and end-losses. A blade-resolved sliding-mesh RANS model was adopted for further study of these systems. While resolving the turbine geometry is possible with the mesh, it is not practical to resolve the near-wall region, and an appropriate turbulence model is needed ($k-\omega$ SST). The existing turbine design used in the end-wall study was not suited to this model due to transitional flow which was present over the blade. To model this, a more complex four equation turbulence model with higher near-wall resolution is required; this model was prohibitively computationally expensive to use for this study. Instead, lateral constraint was further analysed using a newly designed turbine of 8 m diameter ($\lambda^* = 4.5$). This design ensured fully turbulent flow over the blades.

The design for an 8 m diameter turbine was carried out for operating conditions informed by Strangford Lough (a potential site for tidal stream energy extraction) using the RANS-BE method of McIntosh et al. (2011) . A modification to this method was made to facilitate the interpolation across 2D aerofoil data with respect to turbulence intensity, Reynolds number and trailing edge thickness. This method allowed rapid prototyping of designs without the need to continually generate 2D aerofoil data for the flow conditions. For this design study, operation close to the surface posed a cavitation risk. This was mitigated through the implementation of a conservative operating condition based on an adjustment to Wimshurst et al. (2018). This specified the highest λ where cavitation is likely to be avoided ($\lambda = 4.5$) and was used as the design speed of the turbine.

Blade resolved simulations compared both structured and semi-structured meshes in 120° wedge MRF and sliding mesh simulations. It was found that both mesh

schemes produced roughly equivalent results with the semi-structured having a smaller run-time and requiring less user input in the meshing process. As a result, the semi-structured mesh was used for further analysis. This analysis included an investigation into the tip shape of the turbine, comparing between a rounded and flat tip. It was found that a flat tip offered better performance than a rounded tip as the rounded tip encouraged equalisation of pressure between the pressure and suction surfaces through greater tip loss. This design and mesh was used in the yawed turbine simulations.

8.1.3 Yaw controls

The use of yaw adjustment on the outermost turbine within a four turbine long fence was investigated using an unsteady sliding-mesh RANS simulation. The action of yawing the outboard turbine slightly improved its power generation up to an angle of 2.5° however this came at a cost of inboard turbine power as the adjustment of turbine position reduced the lateral confinement on the inboard turbines. Similarly, yawing the outer turbine away from the centerline of the fence improved the inboard turbine's performance and reduced the outboard turbine's performance; this result was consistent whether the turbines were co-rotating or counter-rotating. The results highlight the balance between flow alignment and flow confinement which needs to be struck to efficiently operate a turbine fence.

Despite the optimal power being generated when the rotors were all aligned normal to the free-stream flow, unsteady loading on the outer turbine was shown to be a reason a turbine operator may wish to adjust the yaw angle. Due to the end-loss effect, a cross-stream flow component is present on the turbine which

induces a blade advancing and retreating effect. It was shown that by adjusting the outboard turbine yaw angle to 2.5°, the flow was better aligned and the unsteady loading component was reduced to less than inner turbine's fluctuations (reduction of 47.5%).

Yaw adjustments in conjunction with differential speed controls were combined into a operation strategy to balance loading and reduce load amplitude along the fence. It was demonstrated that a fence with its outboard turbines yawed at 5° would experience a reduction in fence power of 0.3% (relative to optimal operation of the fence using synchronised control) alongside a 1.5% reduction in thrust. This condition coincided with even thrust on the turbines and reduced the loading amplitude of root bending moment on the outer turbine from 50% higher than the inboard turbine to 25% lower.

8.2 Future work

The work undertaken in this thesis has shown that closely spaced turbines can have both positive and negative impacts on performance and loading. While this work has presented two different methods which improve the power output or the reduce the amplitude of unsteady loading cycles experienced by the rotor, additional exploration of flow confinement may further improve turbine fence design. Specifically, investigations of the vertical position of the turbine in the water column and the effect that it has on loading would provide additional insights for improved power generation. Similar to the end turbine within a fence, asymmetric flow confinement conditions are present above and below a turbine (close to the water surface or sea floor). The way in which this positioning affects power and

loading may suggest additional operational adjustments such as a pitch control.

The work in this study has focused on idealised uniform flow conditions. An important next step in transferring this work into real world designs is evaluating it under more realistic flow conditions; this would include a shear profile and waves. Given the improvement on the uniform-steady flow cases, some improvement is expected as the turbine will be better aligned to the mean flow condition. This suggests that on average a perturbation, such as a wave, will have a smaller impact as the flow misalignment on the blade. Yawing a turbine with respect to a wave may also reduce peak loading as the wave does not propagate through the rotor at once.

Incorporating the findings on outer turbine yaw from this thesis into a practical design would require scale testing prior to implementation. This could take the form of a towing tank test (similar to the sidewall analysis). An ensemble of tests at different yaw angles could be compared to the blade resolved CFD results to validate the observations from the model. Further to this, realistic design conditions (such as waves) should also be tested.

8.3 Contribution of work

8.3.1 RANS-BE modelling of turbine fences

A comparison between RANS-BE and experimental results showed that the RANS-BE method is not sufficient for accurately resolving the key physics at play for closely spaced turbines due to a violation of both the no span-wise flow assumption and azimuthal asymmetry. This is due to an interplay between adjacent turbines

which impose lateral forces on the flow as it diverts around the rotor. Consequentially, this type of model is not expected to accurately simulate the improvement in performance due to local blockage. This study also highlighted the complexities of towing tank testing, in particular using the tank sidewall as a symmetry plane. In reality the sidewall is not a true symmetry plane as the thrust from the turbine induces a small boundary layer in the vicinity around the turbine, reducing the turbine performance when positioned close to the wall.

8.3.2 Development of new turbine geometry for fence scale simulation

A new rotor design and computational mesh has been purpose built and calibrated for turbine fence simulations. This design was created to ensure fully turbulent flow over the blades (permitting the use of the $k-\omega$ SST turbulence model) and targeted a reduced cell count in regions where detail is not required using an semi-structured mesh. This design is a computationally efficient and detailed model which can be used to explore the operational parameter space within a turbine fence and may be useful in future detailed operational studies.

8.3.3 Turbine fence end-loss load correction

This study has furthered the understanding of turbine fence end-losses through the use of blade resolved simulations. These simulations have demonstrated that an effect, similar to the blade advancing and retreating effect for yawed flows, is present on the outer turbines within closely spaced turbine fences. Through the implementation of a yaw correction or a turbine fence end-wall this effect can be

controlled for, leading to reduced load disparity between turbines and amplitude of the blade root bending moments.

8.3.4 Papers and planned publications

Work from the initial turbine fence end-wall experimentation has already been published in Ettema et al. (2020), with contributions of this work earning a co-authorship in McNaughton et al. (2020) and paper currently under review as second author (McNaughton et al., 2021). Two additional first author papers are currently being interally reviewed with the intension to publish soon. These are *Investigations into short tidal turbine fence performance with the inclusion of an end-wall* and *Hydrodynamic yaw control within a tidal turbine fence.*

Bibliography

Ahmadian, R., Falconer, R. A., and Lin, B. (2010). Hydro-environmental modeling of proposed Severn barrage, UK. *Proceedings of the Institution of Civil Engineers - Energy*, 163(3):107–117.

Andritz Hydro (2016). Tidal Turbines – Hammerfest.

Annika Clements and Service, M. (2015). Bathymetric and Habitat Map for Strangford Lough. Technical report, AFBI.

ANSYS Inc. (2012). ANSYS ICEM CFD 14.5 User Manual.

ANSYS Inc. (2013). ANSYS Fluent User' s Guide Release 15.0.

ANSYS Inc. (2018). ANSYS Fluent 19.2.

ARC (2022). ARCUS.

Archer, C. L. and Vasel-Be-Hagh, A. (2019). Wake steering via yaw control in multi-turbine wind farms: Recommendations based on large-eddy simulation. *Sustainable Energy Technologies and Assessments*, 33:34–43.

Arshad, M. and O'Kelly, B. C. (2013). Offshore wind-turbine structures: a review. *Proceedings of the Institution of Civil Engineers - Energy*, 166(4):139–152.

Atlantis Strom (2004). Atlantis Strom.

Bahaj, A. S., Molland, A. F., Chaplin, J. R., and Batten, W. M. (2007). Power and thrust measurements of marine current turbines under various hydrodynamic flow conditions in a cavitation tunnel and a towing tank. *Renewable Energy*, 32(3):407–426.

Bak, C., Fuglsang, P., Johansen, J., and Antoniou, I. (2000). Wind tunnel tests of the NACA 63-415 and a modified NACA 63-415 airfoil. Technical report, Risø National Laboratory.

Baker, C. (1991). Tidal power. *Energy Policy*, pages 792–797.

Baratchi, F., Jeans, T. L., and Gerber, A. G. (2017). Actuator line simulation of a tidal turbine in straight and yawed flows. *International Journal of Marine Energy*, 19:235–255.

Bastankhah, M. and Porté-Agel, F. (2016). Experimental and theoretical study of wind turbine wakes in yawed conditions. *Journal of Fluid Mechanics*, 806:506–541.

Belloni, C. S. K. (2013). *Hydrodynamics of Ducted and Open-Centre Tidal Turbines*. PhD thesis, University of Oxford.

Belloni, C. S. K., Willden, R. H. J., and Houlsby, G. T. (2013). A Numerical Analysis of Bidirectional Ducted Tidal Turbines in Yawed Flow. *Marine Technology Society Journal*, 47(4):23–35.

Belloni, C. S. K., Willden, R. H. J., and Houlsby, G. T. (2017). An investiga-

tion of ducted and open-centre tidal turbines employing CFD-embedded BEM. *Renewable Energy*, 108:622–634.

Bertagnolio, F., Sørensen, N. N., Johansen, J., and Fuglsang, P. (2001). Wind turbine airfoil catalogue. Technical report, Risø National Laboratory.

Blue Energy (2010). Blue Energy.

Bonar, P. A. J., Adcock, T. A. A., Venugopal, V., and Borthwick, A. G. L. (2018). Performance of non-uniform tidal turbine arrays in uniform flow. *Journal of Ocean Engineering and Marine Energy*, 4(3):231–241.

Brown, J., Gow, G., and Garrad, A. (2001). SCOTLAND ' S RENEWABLE RESOURCE 2001 – VOLUME II. *Analysis*, II(7).

Burrows, R., Walkington, I. A., Yates, N. C., Hedges, T. S., Wolf, J., and Holt, J. (2009). The tidal range energy potential of the West Coast of the United Kingdom. *Applied Ocean Research*, 31(4):229–238.

Cao, B., McNaughton, J., Vogel, C. R., and Willden, R. H. J. (2019). Hydrodynamic Design of Multi-Rotor Tidal Arrays. *EWTEC 2019*.

Cao, B., Willden, R. H. J., and Vogel, C. R. (2018). Effects of blockage and freestream turbulence intensity on tidal rotor design and performance. *RENEW 2018*, pages 127–135.

Cooke, S. (2016). *Enhanced Array Design for Tidal Power Generation*. PhD thesis, University of Oxford.

Cooke, S. C., Willden, R. H. J., Byrne, B. W., Stallard, T., and Olczak, A. (2015). Experimental Investigation of Thrust and Power on a Partial Fence

Array of Tidal Turbines. *Proceedings of the 11th European Wave and Tidal Energy Conference*.

DNV GL (2015). DNVGL-ST-0164 Tidal Turbines. Technical report, DNV GL.

Dou, B., Guala, M., Lei, L., and Zeng, P. (2019). Wake model for horizontal-axis wind and hydrokinetic turbines in yawed conditions. *Applied Energy*, 242:1383–1395.

Draper, S. and Nishino, T. (2014). Centred and staggered arrangements of tidal turbines. *Journal of Fluid Mechanics*, 739:72–93.

Ettema, S., McNaughton, J., Vogel, C., and Willden, R. (2020). Experimental investigation of the performance of a sidewall-constrained tidal turbine fence. *RENEW 2020*, pages 527–533.

European Marine Energy Centre (2018). Open Hydro.

Fleming, C. F. and Willden, R. H. J. (2016). Analysis of bi-directional ducted tidal turbine performance. *International Journal of Marine Energy*, 16:162–173.

Frid, C., Andonegi, E., Depestele, J., Judd, A., Rihan, D., Rogers, S. I., and Kenchington, E. (2012). The environmental interactions of tidal and wave energy generation devices. *Environmental Impact Assessment Review*, 32(1):133–139.

Galloway, P. W., Myers, L. E., and Bahaj, A. B. S. (2014). Quantifying wave and yaw effects on a scale tidal stream turbine. *Renewable Energy*, 63:297–307.

Galloway, P. W., Myers, L. E., and Bahaj, A. S. (2011). Experimental and Numerical Results of Rotor Power and Thrust of a Tidal Turbine Operating at

Yaw and in Waves. In *Proceedings of the World Renewable Energy Congress – Sweden, 8–13 May, 2011, Linköping, Sweden*, volume 57, pages 2246–2253. Linköping University Electronic Press.

Garrett, C. and Cummins, P. (2007). The efficiency of a turbine in a tidal channel. *Journal of Fluid Mechanics*, 588:243–251.

Glauert, H. (1935). Airplane propellers. In *Aerodynamic Theory*, volume Vol. IV, pages 169–269. Aerodynamic Theory.

Halo Energy (2019). Halo Energy.

Hansen, M. O. and Johansen, J. (2004). Tip studies using CFD and comparison with tip loss models. In *Wind Energy*, volume 7, pages 343–356. John Wiley & Sons, Ltd.

Houlsby, G. T. and Draper, S. (2008). Application of Linear Momentum Actuator Disc Theory to Open Channel Flow. Technical report, University of Oxford.

Hunter, W., Nishino, T., and Willden, R. H. J. (2015). Investigation of tidal turbine array tuning using 3D Reynolds-Averaged Navier-Stokes Simulations. *International Journal of Marine Energy*, 10:39–51.

Igra, O. (1981). Research and development for shrouded wind turbines. *Energy Conversion and Management*, 21:13–48.

Jeffcoate, P., Burden, C., Cresswell, N., Lee, J., Kaufmann, N., Starzmann, R., and Pieroway, R. (2021). Comparisons between flood and ebb performance of PLAT-I in nova scotia. *Proceedings of the European Wave and Tidal Energy Conference*, pages 1934–1.

Khamlaj, T. A. and Rumpfkeil, M. P. (2018). Analysis and optimization of ducted wind turbines. *Energy*, 162:1234–1252.

Khan, M. J., Bhuyan, G., Iqbal, M. T., and Quaicoe, J. E. (2009). Hydrokinetic energy conversion systems and assessment of horizontal and vertical axis turbines for river and tidal applications: A technology status review. *Applied Energy*, 86(10):1823–1835.

King, J. and Tryfonas, T. (2009). Tidal stream power technology - State of the art. In *OCEANS '09 IEEE Bremen: Balancing Technology with Future Needs*.

Koh, W. X. and Ng, E. Y. (2016). Effects of Reynolds number and different tip loss models on the accuracy of BEM applied to tidal turbines as compared to experiments. *Ocean Engineering*, 111:104–115.

Kok, J. C. (2000). Resolving the dependence on freestream values for the k-ω turbulence model. Technical Report 7, National Aerospace Laboratory.

Kolekar, N. and Banerjee, A. (2015). Performance characterization and placement of a marine hydrokinetic turbine in a tidal channel under boundary proximity and blockage effects. *Applied Energy*, 148:121–133.

Kregting, L. and Elsäßer, B. (2014). A hydrodynamic modelling framework for strangford lough part 1: Tidal model. *Journal of Marine Science and Engineering*, 2(1):46–65.

Laurens, J. M., Ait-Mohammed, M., and Tarfaoui, M. (2016). Design of bare and ducted axial marine current turbines. *Renewable Energy*, 89:181–187.

Liu, C. and Hu, C. (2015). Numerical Prediction of the Hydrodynamic Performance of a Horizontal Tidal Turbines. *OMAE*, 34.

Liu, J., Lin, H., and Purimitla, S. R. (2016). Wake field studies of tidal current turbines with different numerical methods. *Ocean Engineering*, 117:383–397.

Lu, X. and McElroy, M. B. (2017). Global Potential for Wind-Generated Electricity. In *Wind Energy Engineering: A Handbook for Onshore and Offshore Wind Turbines*, pages 51–73. PNAS.

MacEnri, J., Reed, M., and Thiringer, T. (2011). Power quality performance of the tidal energy converter, SeaGen. In *Proceedings of the International Conference on Offshore Mechanics and Arctic Engineering - OMAE*, volume 5, pages 529–536. American Society of Mechanical Engineers Digital Collection.

MacEnri, J., Reed, M., and Thiringer, T. (2013). Influence of tidal parameters on SeaGen flicker performance. *Philosophical Transactions of the Royal Society A: Mathematical, Physical and Engineering Sciences*, 371(1985):20120247.

Malki, R., Williams, A. J., Croft, T. N., Togneri, M., and Masters, I. (2013). A coupled blade element momentum - Computational fluid dynamics model for evaluating tidal stream turbine performance. *Applied Mathematical Modelling*, 37(5).

Mansour, N. N., Kim, J., and Moin, P. (1988). Near-Wall k-e Turbulence Modeling. *AIAA Journal*, 27(8).

Masters, I., Chapman, J. C., Willis, M. R., and Orme, J. A. C. (2011). A robust blade element momentum theory model for tidal stream turbines including

tip and hub loss corrections. *Journal of Marine Engineering and Technology*, 10(1):25–35.

McIntosh, S. C., Fleming, C. F., and Willden, R. H. J. (2011). Embedded RANS-BEM Tidal Turbine Design. *EWTEC 2011*.

McNaughton, J., Cao, B., Ettema, S., Zilic de Arcos, F., Vogel, C., and Willden, R. (2020). Experimental testing of the performance and interference effects of a cross-stream array of tidal turbines. *RENEW 2020*, pages 563–570.

McNaughton, J., Cao, B., Vogel, C. R., and Willden, R. H. J. (2019). Model scale testing of multi-rotor arrays designed to exploit constructive interference effects. *Proceedings of the 13th European Wave and Tidal Energy Conference*.

McNaughton, J., Ettema, S., Zilic De Arcos, F., Vogel, C. R., and Willden, R. H. J. (2021). Tow tank investigation into the influence of lateral spacing and differential control on the performance of a multi-rotor tidal stream turbine fence. *Journal of Marine Science and Engineering*, pages 1–18.

Menter, F. R. (1994). Two-equation eddy-viscosity turbulence models for engineering applications. *AIAA Journal*, 32(8):1598–1605.

Menter, F. R., Kuntz, M., and Langtry, R. (2003). Ten Years of Industrial Experience with the SST Turbulence Model Turbulence heat and mass transfer. *Heat and Mass Transfer*, 4:625–632.

Menter, F. R., Langtry, R. B., Likki, S. R., Suzen, Y. B., Huang, P. G., and Völker, S. (2006). A correlation-based transition model using local variables - Part I: Model formulation. *Journal of Turbomachinery*, 128(3):413–422.

Micallef, D. and Sant, T. (2016). A Review of Wind Turbine Yaw Aerodynamics. In *Wind Turbines - Design, Control and Applications*. InTech.

Moriarty, P. J. and Hansen, A. C. (2005). AeroDyn Theory Manual. *Renewable Energy*, 15(January):500–36313.

Musa, M., Ravanelli, G., Bertoldi, W., and Guala, M. (2020). Hydrokinetic Turbines in Yawed Conditions: Toward Synergistic Fluvial Installations. *Journal of Hydraulic Engineering*, 146(4):04020019.

Neill, S. P., Angeloudis, A., Robins, P. E., Walkington, I., Ward, S. L., Masters, I., Lewis, M. J., Piano, M., Avdis, A., Piggott, M. D., Aggidis, G., Evans, P., Adcock, T. A., Židonis, A., Ahmadian, R., and Falconer, R. (2018). Tidal range energy resource and optimization – Past perspectives and future challenges. *Renewable Energy*, 127:763–778.

NES Fircroft (2021). The Biggest Wind Turbines in the World.

Nishino, T. and Willden, R. H. J. (2012). The efficiency of an array of tidal turbines partially blocking a wide channel. *Journal of Fluid Mechanics*, 708:596–606.

Nishino, T. and Willden, R. H. J. (2013). Two-scale dynamics of flow past a partial cross-stream array of tidal turbines. *Journal of Fluid Mechanics*, 730:220–244.

Olczak, A., Stallard, T., Feng, T., and Stansby, P. K. (2016). Comparison of a RANS blade element model for tidal turbine arrays with laboratory scale measurements of wake velocity and rotor thrust. *Journal of Fluids and Structures*, 64:87–106.

Orbital Marine Power (2019). Orbital Marine Power.

ORPC (2019). ORPC.

Park, S., Park, S., and Rhee, S. H. (2016). Influence of blade deformation and yawed inflow on performance of a horizontal axis tidal stream turbine. *Renewable Energy*, 92:321–332.

Payne, G. S., Stallard, T., Martinez, R., and Bruce, T. (2018). Variation of loads on a three-bladed horizontal axis tidal turbine with frequency and blade position. *Journal of Fluids and Structures*, 83:156–170.

Ross, H. and Polagye, B. (2020). An experimental assessment of analytical blockage corrections for turbines. *Renewable Energy*, 152:1328–1341.

Rourke, F. O., Boyle, F., and Reynolds, A. (2010a). Marine current energy devices: Current status and possible future applications in Ireland. *Renewable and Sustainable Energy Reviews*, 14(3):1026–1036.

Rourke, F. O., Boyle, F., and Reynolds, A. (2010b). Tidal energy update 2009. *Applied Energy*, 87(2):398–409.

Sathiamoorthy, M. and Probert, S. D. (1994). The integrated Severn barrage complex: Harnessing tidal, wave and wind power. *Applied Energy*, 49(1):17–46.

Schlichting, H. and Gersten, K. (2000). *Boundary-Layer Theory 8th Edition*. Springer.

Schluntz, J. . (2014). *Tidal turbine array modelling*. PhD thesis, University of Oxford.

Schluntz, J. . and Willden, R. H. J. (2015). The effect of blockage on tidal turbine rotor design and performance. *Renewable Energy*, 81:432–441.

Schmitz, S. and Jha, P. K. (2013). Modeling the wakes of wind turbines and rotorcraft using the actuator-line method in an OpenFOAM - LES solver. In *Annual Forum Proceedings - AHS International*, volume 3, pages 2228–2235.

Shahsavarifard, M. and Bibeau, E. L. (2020). Performance characteristics of shrouded horizontal axis hydrokinetic turbines in yawed conditions. *Ocean Engineering*, 197:106916.

Shiu, H., Van Dam, C. P., Johnson, E., Barone, M., Phillips, R., Straka, W., Fontaine, A., and Jonson, M. (2012). A design of a hydrofoil family for current-driven marine-hydrokinetic turbines. In *International Conference on Nuclear Engineering, Proceedings, ICONE*, volume 4, pages 839–847. American Society of Mechanical Engineers (ASME).

Siddiqui, M. S., Rasheed, A., Tabib, M., and Kvamsdal, T. (2016). Numerical Analysis of NREL 5MW Wind Turbine: A Study Towards a Better Understanding of Wake Characteristic and Torque Generation Mechanism. In *Journal of Physics: Conference Series*, volume 753, page 32059. Institute of Physics Publishing.

Siemens (2015). World-leading tidal energy system achieves 5GWh milestone.

Simec Atlantas (2016). AR1500 TIDAL TURBINE. Technical report, Simec Atlantas.

SIMEC Atlantis Energy (2019). Simec Atlantis Energy.

SME (2019). Tidal Energy.

Snel, H. (2003). Review of aerodynamics for wind turbines. *Wind Energy*, 6(3):203–211.

Veers, P. S., Ashwill, T. D., Sutherland, H. J., Laird, D. L., Lobitz, D. W., Griffin, D. A., Mandell, J. F., Músial, W. D., Jackson, K., Zuteck, M., Miravete, A., Tsai, S. W., and Richmond, J. L. (2003). Trends in the design, manufacture and evaluation of wind turbine blades. *Wind Energy*, 6(3):245–259.

Vermeer, L. J., Sørensen, J. N., and Crespo, A. (2003). Wind turbine wake aerodynamics.

Vogel, C. R., Houlsby, G. T., and Willden, R. H. (2016). Effect of free surface deformation on the extractable power of a finite width turbine array. *Renewable Energy*, 88:317–324.

Vogel, C. R. and Willden, R. H. J. (2017). Multi-rotor tidal stream turbine fence performance and operation. *International Journal of Marine Energy*, 19:198–206.

Vogel, C. R. and Willden, R. H. J. (2019). Improving Tidal Turbine Performance Through Multi-Rotor Fence Configurations. *Journal of Marine Science and Application*, 18(1):17–25.

Vogel, C. R., Willden, R. H. J., and Houlsby, G. T. (2018). Blade element momentum theory for a tidal turbine. *Ocean Engineering*, 169:215–226.

Waters, S. and Aggidis, G. (2016). A world first: Swansea Bay tidal lagoon in review. *Renewable and Sustainable Energy Reviews*, 56:916–921.

Wimshurst, A., Vogel, C. R., and Willden, R. H. J. (2018). Cavitation limits on tidal turbine performance. *Ocean Engineering*, 152:223–233.

Wind-works (2019). FloDesign-Ogin DAWT.

Xia, J., Falconer, R. A., and Lin, B. (2010). Impact of different operating modes for a Severn Barrage on the tidal power and flood inundation in the Severn Estuary, UK. *Applied Energy*, 87(7):2374–2391.

Xu, H., Shen, W., Zhu, W., Yang, H., and Liu, C. (2014). Aerodynamic analysis of trailing edge enlarged wind turbine airfoils. In *Journal of Physics: Conference Series*, volume 524.